



Swansea University
Prifysgol Abertawe

MODELLING, CHARACTERISATION AND INTERPRETATION OF
RHEOLOGICAL EXPERIMENTS PERFORMED ON AQUEOUS
SOLUTIONS OF WORM LIKE MICELLES

Adeniyi Ogunkeye
MEng

Swansea University

Submitted to Swansea University in fulfillment of the requirements for the Degree of
Ph.D.

May 2023

Copyright: The Author, Adeniyi Ogunkeye, 2023.

Abstract

This thesis reports a series of theoretical, experimental and computational investigations concerning advanced rheometry and the dynamics of worm like micellular systems (WLMs) in superposition rheometry. A robust experimental data set is first obtained under both parallel and orthogonal superposition rheometry conditions before the ability of the Corotational Maxwell, Giesekus and, for the first time, Gordon-Schowolter constitutive models to capture the behaviour of WLMs under superposition flows is evaluated. The initiation of stress controlled oscillatory rheometry is then investigated both theoretically and experimentally (using the same WLM system) to determine the impact of instrument inertia on the establishment of steady state oscillatory flows. This study reveals that the time scale for the establishment of steady state oscillations can be dramatically impacted by the presence of instrument inertia. Finally, a Brownian Dynamics approach is used in an attempt to identify the polymer dynamics responsible for the appearance of negative values of the ‘parallel storage modulus’ under certain conditions, as is often noted in the literature.

Declarations and Statements

DECLARATION

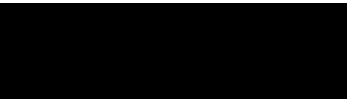
This work has not previously been accepted in substance for any degree and is not being concurrently submitted in candidature for any degree.

Signed: 

Date: 16/08/2023

STATEMENT

This thesis is the result of my own investigations, except where otherwise stated. Where correction services have been used, the extent and nature of the correction is clearly marked in a footnote(s).

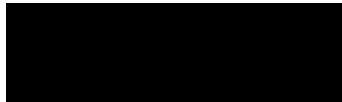
Other sources are acknowledged by footnotes giving explicit references. A bibliography is appended 

Signed: 

Date: 16/08/2023

I hereby give consent for my thesis, if accepted, to be available for electronic sharing after expiry of a bar on access approved by the Swansea University.

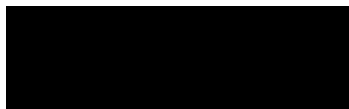
Signed:



Date: 16/08/2023

The University's ethical procedures have been followed and, where appropriate, that ethical

Signed:



Date: 16/08/2023

Acknowledgements

I wish to thank my supervisor Dr. Dj Curtis for his unrelenting efforts and guide throughout my research. I also appreciate all assistance provided by Dr.Rebecca Hudson especially for her support in handling the delicate instruments used throughout this research. In particular, I am full of gratitude to all members of my family for their endless financial support, inspirations and encouragement throughout my PhD program.

Contents

1	Introduction	19
2	Basic principles of Rheology/Rheometry	22
2.1	Introduction	22
2.1.1	Rheology	23
2.1.2	Viscoelasticity	27
2.1.3	Small Amplitude Oscillatory Shear	29
2.2	Rheometry	31
2.3	Geometries	33
2.3.1	Parallel plate	35
2.3.2	Cone and plate (CP) measuring system	36
2.3.3	Narrow gap double wall concentric cylinder	37
3	Worm Like Micelles	39
3.1	Introduction	39
3.2	Micelle Formation	39
3.3	Rheological Behaviour of Wormlike Micelles	41
3.4	Shear Banding Phenomena	45
4	Evaluation of Constitutive Models for WLMs	47
4.1	Superposition Rheometry	47
4.2	Experimental Methods	66
4.3	Data Processing	67

4.4	Results & Discussion	71
4.5	Conclusion	85
5	Influence of Inertia on Startup of Stress Controlled Oscillatory Shear	86
5.1	Introduction	86
5.2	Modelling	89
5.2.1	Frequency Dependency	94
5.2.2	Effect of Inertia on Conditioning Time	100
5.3	Experimental	100
5.3.1	Materials & Methods	100
5.3.2	Results & Discussion	102
5.4	Conclusion	105
6	Investigation of Negative Storage Modulus G'_{\parallel} in Parallel Superposition Rheometry via Brownian Dynamics	106
6.1	Introduction	106
6.1.1	Integration Scheme	112
6.2	Validation	114
6.2.1	Equilibrium properties	115
6.2.2	Steady Shear Simulations	119
6.2.3	Small Amplitude Oscillatory Shear (SAOS)	121
6.3	Optimization	126
6.4	Parallel Superposition Simulations	130
6.5	Conclusions	137
7	Conclusion & Recommendations	138
A	Chapter4:Appendix	142
B	Chapter5:Appendix	157
C	Chapter6:Appendix	159

D Publications	173
E Nomenclature	185

List of Figures

2.1	The result of the application of a shear stress, σ to a block of Hookean solid. On the application of the stress the material section ABCD is deformed and becomes ABC'D'.	24
2.2	Schematic representation of a tangential force on the face of the cube. . .	24
2.3	Laminar flow in the form of fluid layers	25
2.4	Flow curves for Newtonian (black), shear thinning (red), shear thickening (blue) and Bingham plastic (green) behaviour in fluids. The yield stress of the Bingham plastic is represented by σ_γ	26
2.5	The viscoelastic solid contains a spring and dashpot arranged in parallel.	27
2.6	The viscoelastic liquid contains a spring and dashpot arranged in series. .	28
2.7	A schematic diagram of a Separate Motor Transducer (SMT) rheometer. The motor and the torque sensing element are separate thereby eliminating instrument inertial artefacts from the system.	32
2.8	A schematic diagram of a Combined Motor Transducer (CMT) rheometer.	34
2.9	Schematic diagram of a parallel plate geometry system with radius (r) and gap (d).	36
2.10	A schematic diagram of a cone and plate geometry set up with radius (r) and angle (α). The truncation gap is highlighted in red.	37
2.11	Schematic representation of the cross-section of a narrow gap double wall concentric cylinder geometry.	38
3.1	Schematic illustration of a surfactant	40

3.2	Schematic representation of the three states in which surfactant molecules reside in water.	40
3.3	Schematic illustration of the relationship between the packing parameter (p) and the morphology of self-assembled surfactant aggregates. Reproduced from ref [18] with permission from the Royal Society of Chemistry.	41
3.4	Contrasting the structure and rheology of polymers (in solution) and wormlike micelles. Reproduced from ref [30] with permission from the Royal Society of Chemistry.	43
4.1	a) The orthogonal superposition equipment with a double wall Couette cell that has an opening in the inner wall of the cup connecting to the liquid reservoir in the center of the cup b) This flow is achieved by superposition of an oscillatory flow in the orthogonal direction ($\dot{\gamma}_{\perp}$) onto the steady shear flow ($\dot{\gamma}$).	50
4.2	Schematics of (a) the bob, (b) the double-wall cup (the outer cylinder is shown as translucent). Reproduced with permission from Ref [86].	51
4.3	The vertical cross section of the OSP double-wall concentric cylinder geometry, displayed for the 0.5mm gap cell. The center cylinder (bob) is shown in gray. The outer and inner cylinders (cup) are shown in black. The top openings on the bob and bottom openings on the cylinder are depicted by dashed lines.	52
4.4	Critical frequency against shear rate with different values of the non-affine parameter (a). a = 0.25 (blue), 0.5 (black), 0.75 (red), 0.99 (green) and $\lambda_1 = 1.4739$ s.	62
4.5	The linear viscoelastic moduli of the ST solution showing experimental values (symbols) and calculated values (solid lines) obtained from a two mode Maxwell model with a solvent viscosity. The storage modulus (G') is represented by blue shapes and lines. The loss modulus (G'') is represented by red shapes and lines. The black dashed line represents $\lambda_{br} = 1/G''_{min}$	69

4.6	The linear viscoelastic moduli of the SB solution showing experimental values (symbols) and calculated values (solid lines) obtained from a two mode Maxwell model with a solvent viscosity. The storage modulus (G') is represented by blue shapes and lines. The loss modulus (G'') is represented by red shapes and lines. The black dashed line represents $\lambda_{br} = 1/G''_{min}$.	70
4.7	Data analysis procedure A for the shear thinning (ST) formulation using the Giesekus (GIE) model. The blue and red circles are experimental G' and G'' , respectively. The solid lines are fits with the GIE model. The open shapes are absolute values of any negative experimental data. Parameters from the SAOS data given as $G = 51.8 Pa$, $\lambda = 0.6546 s$, $\alpha = 0.3$ & $\eta_s = 0.059 Pa.s$ is used to calculate model fits for PSR (Eqn 4.19 & Eqn 4.18(left)) and OSR (Eqn 4.17 & Eqn 4.16 (right)).	73
4.8	Data analysis procedure A for the shear thinning (ST) formulation using the Corotational Maxwell model (CRM). The blue and red circles are experimental G' and G'' , respectively and the solid lines are fits with the CRM model (PSR (Eqn 4.27 & Eqn 4.28), OSR (Eqn 4.29 & Eqn 4.30)). The open shapes are absolute values of any negative experimental data and $a = 0$.	74
4.9	Data analysis procedure A for the shear thinning (ST) formulation using the Gordon-Schowalter model (GS). The blue and red circles are experimental G' and G'' , respectively and the solid lines are fits with the GS model (PSR (Eqn 4.55 & Eqn 4.56), OSR (Eqn 4.64 & Eqn 4.65)). The open shapes are absolute values of any negative experimental data.	75
4.10	Data analysis procedure B for the shear thinning (ST) formulation using the Corotational Maxwell model (CRM). The blue and red circles are experimental G' and G'' , respectively and the solid lines are fits with the CRM model (PSR (Eqn 4.27 & Eqn 4.28), OSR (Eqn 4.29 & Eqn 4.30)). The open shapes are absolute values of any negative experimental data and $a = 0$.	76

4.11	Data analysis procedure B for the shear thinning (ST) formulation using the Gordon-Schowalter model (GS). The blue and red circles are experimental G' and G'' , respectively and the solid lines are fits with the GS model (PSR(Eqn 4.55 & Eqn 4.56) , OSR(Eqn 4.64 & Eqn 4.65)). The open shapes are absolute values of any negative experimental data. . . .	77
4.12	Data analysis procedure A for the shear banding (SB) formulation using the Giesekus (GIE) model. The blue and red circles are experimental G' and G'' , respectively. The solid lines are fits with the GIE model. The open shapes are absolute values of any negative experimental data. Parameters from the SAOS data given as $G = 115 Pa$, $\lambda = 1.0606 s$, $\alpha = 0.5$ & $\eta_s = 0.2793 Pa.s$ is used to calculate model fits for PSR(Eqn 4.19 & Eqn 4.18(left)) and OSR(Eqn 4.17 & Eqn 4.16 (right)).	79
4.13	Data analysis procedure A for the shear banding (SB) formulation using the Corotational Maxwell model (CRM). The blue and red circles are experimental G' and G'' , respectively and the solid lines are fits with the CRM model (PSR(Eqn 4.27 & Eqn 4.28), OSR(Eqn 4.29 & Eqn 4.30)). The open shapes are absolute values of any negative experimental data and $a = 0$	80
4.14	Data analysis procedure A for the shear banding (SB) formulation using the Gordon-Schowalter model (GS). The blue and red circles are experimental G' and G'' , respectively and the solid lines are fits with the GS model (PSR(Eqn 4.55 & Eqn 4.56), OSR(Eqn 4.64 & Eqn 4.65)). The open shapes are absolute values of any negative experimental data. . . .	81
4.15	Data analysis procedure B for the shear banding (SB) formulation using the Corotational Maxwell model (CRM). The blue and red circles are experimental G' and G'' , respectively and the solid lines are fits with the CRM model (Eqn 4.27, Eqn 4.28, Eqn 4.29 & Eqn 4.30). The open shapes are absolute values of any negative experimental data and $a = 0$	82

4.16	Data analysis procedure B for the shear banding (SB) formulation using the Gordon-Schowalter model (GS). The blue and red circles are experimental G' and G'' , respectively and the solid lines are fits with the GS model (PSR(Eqn 4.55 & Eqn 4.56) , OSR(Eqn 4.64 & Eqn 4.65)) . The open shapes are absolute values of any negative experimental data. . . .	83
5.1	Step torque test with hagfish gel in concentric cylinder geometry plotted as apparent compliance. The first 80 seconds of data are caused by a coupling of instrument inertia and elasticity leading to creep ringing effects which are identified by the damped oscillations. This data can be misinterpreted as real material data whereas it is a result of instrument artefacts. Reproduced from Ref [31] permission from Springer New York.	87
5.2	Low frequency ($\omega = 0.1 \text{ rad s}^{-1}$) response of a two mode Maxwell model ($\tau_1 = 0.01 \text{ s}$, $\tau_2 = 1.0 \text{ s}$, $\eta_1 = 1.0 \text{ Pa.s}$, $\eta_2 = 10.0 \text{ Pa.s}$, $I = 0.1 \text{ Pa.s}^2$) in the presence of instrument inertia (a) and in the inertia-less case (b). In both subfigures, the red line shows the complete solution, the dashed black line shows the offset (γ_{off}), the black line shows the steady state periodic response (γ_p) and the blue line shows the transient response (γ_t). At low frequencies, including inertia in the model has negligible effect as the transient response is insignificant in comparison to the periodic and offset terms.	96
5.3	Intermediate frequency ($1.0 \text{ rad/s} \leq \omega \leq 10 \text{ rad/s}$) response of a two mode Maxwell model ($\tau_1 = 0.01 \text{ s}$, $\tau_2 = 1.0 \text{ s}$, $\eta_1 = 1.0 \text{ Pa.s}$, $\eta_2 = 10.0 \text{ Pa.s}$, $I = 0.1 \text{ Pa.s}^2$) in the presence of instrument inertia (a-c) and in the inertialess case (d-f). In all subfigures, the red line shows the complete solution, the dashed black line shows the offset (γ_{off}), the black line shows the steady state periodic response (γ_p) and the blue line shows the transient response (γ_t). As frequency increases the effect of the transient terms becomes more important in the initial response. At these frequencies the inclusion of inertia introduces a damped oscillatory behaviour to the transient response which decays within the period of one oscillation.	97

5.4	High frequency ($\omega > 10 \text{ rad s}^{-1}$) response of a two mode Maxwell model ($\tau_1 = 0.01 \text{ s}$, $\tau_2 = 1.0 \text{ s}$, $\eta_1 = 1.0 \text{ Pa.s}$, $\eta_2 = 10.0 \text{ Pa.s}$, $I = 0.1 \text{ Pa.s}^2$) in the presence of instrument inertia (a,b) and in the inertia-less case (c,d). In all subfigures the red line shows the complete solution, the dashed black line shows the offset (γ_{off}), the black line shows the steady state periodic response (γ_p) and the blue line shows the transient response(γ_t). the transient response takes takes longer than one period of the waveform to decay to a negligible magnitude	98
5.5	Amplitude of the periodic stress component as a function of frequency for a two mode Maxwell model ($\tau_1 = 0.01 \text{ s}$, $\tau_2 = 1.0 \text{ s}$, $\eta_1 = 1.0 \text{ Pa.s}$, $\eta_2 = 10.0 \text{ Pa.s}$, $I = 0.1 \text{ Pa.s}^2$).	99
5.6	Pole plot for the ‘inertialess’ and ‘including inertia’ cases for a two mode Maxwell model ($\tau_1 = 0.01 \text{ s}$, $\tau_2 = 1.0 \text{ s}$, $\eta_1 = 1.0 \text{ Pa.s}$, $\eta_2 = 10.0 \text{ Pa.s}$, $I = 0.1 \text{ Pa.s}^2$). Whilst the inertialess transient is characterised by a single real pole at $s = -1/\lambda_k$, inertia introduces a pair of complex conjugate poles which dominate the transient response and generate a dominant effective retardation time (λ^*).	101
5.7	G' (blue) & G'' (red) SAOS data using aluminium cone geometry for a 4.1 wt% solution of <i>CPyCl</i> fitted with Eqn 5.37 & Eqn 5.38. The lines show a two mode Maxwell model fit to the experimental data using the discrete relaxation spectra. The discrete relaxation spectra is $\tau_1 = 0.0122 \text{ s}$, $\tau_2 = 0.3038 \text{ s}$, $\eta_1 = 0.0730 \text{ Pa.s}$ and $\eta_2 = 14.99 \text{ Pa.s}$	103
5.8	Transient data for start up of stress controlled oscillatory shear using aluminium cone geometry for a 4.1 wt% solution of <i>CPyCl</i> fitted with Eqn 5.36 using a stress and strain constant of 17683.9 Pa/N.m and 28.557 1/rad respectively. The red shapes are the experimental transient data for various frequencies and the blue lines are the model fits to the transient data.	104
6.1	Freely-jointed multi-bead-spring model composed of M beads and $M - 1$ springs.	109

6.2	The Hookean dumbbell model	111
6.3	The freely jointed bead-rod chain (Kramers chain) model for a polymer chain	115
6.4	Evolution of the reduced square end-to-end distance of a bead spring for a time step (Δt) of $\lambda_H/100$. Different chain populations have been employed & $\lambda_H = 1$. The simulated data is calculated from Eqn 6.21 & the red dashed line is calculated from Eqn 6.20.	117
6.5	Evolution of the reduced square end-to-end distance of a dumbbell after sudden thermal activation for different time steps in the BD simulation. The Square end-to-end distance is made dimensionless using the equilibrium value given by the kinetic theory. A population of 10^4 dumbbells has been employed. Reproduced from Ref [22] with permission from SPRINGER VERLAG.	118
6.6	The growth of the viscosity at several shear rates for seven bead chains where $N_{chains} = 1000$, $b = 100$ and $\Delta t = 0.1$ calculated using Eqn 6.22 & Eqn 6.7. The top image shows the results of the simulations and the bottom shows the results publish by Tanner & Wiest [93].	120
6.7	The BD prediction for storage and loss modulus at SAOS compared to the Rouse model represented by a solid blue line at various frequencies, ω . . .	121
6.8	The Lissajous curves of a viscoelastic material represented by a tilted ellipse from which the storage and loss modulus may be obtained.	123
6.9	Lissajous plots of BD simulations at increasing frequencies of 0.1 rad s^{-1} , 0.4 rad s^{-1} & 8 rad s^{-1} for a BD total time of 200 s and $\gamma_0 = 0.1$. These curves are normalized stress versus normalized strain. The red lines are calculated with Eqn 6.30 & 6.31 while the blue circles represent stress and strain from the BD simulations.	125
6.10	The BD predictions for storage modulus (G') and loss modulus (G'') at $\dot{\gamma}$ or $Pe = 0$ for different chain populations (N_{chains}) at different timesteps (Δt) at $\omega = 2.91 \text{ rad s}^{-1}$ compared to the Rouse chain predictions (G' & G'') represented with a solid black line at the same frequency (ω).	126

6.11	The BD predictions for storage modulus (G') and loss modulus(G'') at $\dot{\gamma}$ or $Pe = 0$ vs Δt for different chain populations, N_{chains} at $\omega = 2.91 \text{ rad s}^{-1}$ compared to the Rouse chain predictions (G' & G'') represented with a solid black line at the same frequency, ω	128
6.12	The CPU time required to complete BD simulations for different number of Chains, N_{chains} at $\omega = 2.91 \text{ rad s}^{-1}$ for different timesteps (Δt).	129
6.13	Parallel Superposition Rheometry performed by a BD simulation at low shear rates (shapes, open shapes represent absolute values of any negative data) and compared with the Rouse model (solid blue line). The black dashed lines are used to denote the region of acceptable data.	130
6.14	Parallel Superposition Rheometry performed by a BD simulation at High shear rates (shapes), open shapes represent absolute values of any negative data.	131
6.15	The Lissajous curves for BD simulations at the appearance of negative values G'_{\parallel} at $\gamma_0 = 0.1$ & $\Delta t = 0.001$ and 5000 chains and a simulation time of 200 s. These curves are normalized stress versus normalized strain. The red lines are calculated with Eqn 6.30 & 6.31 while the blue circles represent stress and strain from the BD simulations.	133
6.16	The Lissajous curves for 10 s^{-1} at $\omega = 0.63 \text{ rad s}^{-1}$ for 5000 chains , $\Delta t = 0.001$, total time = 200 s and decreasing oscillation amplitude, γ_0 . The red lines are calculated with Eqn 6.30 & 6.31 while the blue circles represent stress and strain from the BD simulations.	134
6.17	The Lissajous curves for 10 s^{-1} at $\omega = 0.63 \text{ rad s}^{-1}$ for 5000 chains, $\Delta t = 0.01$ and increasing total time, t at $\gamma_0 = 0.01$. The red lines are calculated with Eqn 6.30 & 6.31 while the blue circles represent stress and strain from the BD simulations.	135
6.18	Experimental Lissajous curves for a WLM using ARES G2 with double wall concentric cylinder at various frequencies.	136

A.1	The determination of the PSR pseudo-linear viscoelastic range for 4.1wt% <i>CPyCl</i> at 0.1(Δ), 1(\circ), 10(\triangleleft), 100(+) <i>rad s⁻¹</i> at 0, 0.1, 0.4 <i>s⁻¹</i> respectively. The blue shapes are storage moduli (G'_{\parallel}) and the green shapes are the loss moduli (G''_{\parallel}). The low-torque limit effects (red dashed) line is calculated from Eqn A.1.	144
A.2	The determination of the PSR pseudo-linear viscoelastic range for 4.1wt% <i>CPyCl</i> at 0.1(Δ), 1(\circ), 10(\triangleleft), 100(+) <i>rad s⁻¹</i> at 1,4, 10 <i>s⁻¹</i> respectively. The blue shapes are storage moduli (G'_{\parallel}) and the green shapes are the loss moduli (G''_{\parallel}). The low-torque limit effects (red dashed) line is calculated from Eqn A.1.	145
A.3	The frequency sweeps of 4.1wt% <i>CPyCl</i> at 0, 0.1, 0.4 <i>s⁻¹</i> respectively using strains of 1, 2, 4, 10, 20, 40%. The blue shapes are storage moduli (G'_{\parallel}) and the green shapes are the loss moduli (G''_{\parallel}). The low-torque limit effects (red dashed) line is calculated from Eqn A.1.	146
A.4	The frequency sweeps of 4.1wt% <i>CPyCl</i> at 1, 4, 10 <i>s⁻¹</i> respectively using strains of 1, 2, 4, 10, 20, 40%. The blue shapes are storage moduli (G'_{\parallel}) and the green shapes are the loss moduli (G''_{\parallel}). The low-torque limit effects (red dashed) line is calculated from Eqn A.1.	147
A.5	The variation of the minimum torque (T_{min}) with shearrate ($\dot{\gamma}$) for PSR.	148
A.6	The determination of the OSR pseudo-linear viscoelastic range for 4.1wt% <i>CPyCl</i> at 0.1(Δ), 1(\circ), 10(\triangleleft), 40(+) <i>rad s⁻¹</i> at 0, 0.1, 0.4 <i>s⁻¹</i> respectively. The blue shapes are storage moduli (G'_{\perp}) and the green shapes are the loss moduli (G''_{\perp}). The low-torque limit effects (red dashed) line is calculated from Eqn A.1.	149
A.7	The determination of the OSR pseudo-linear viscoelastic range for 4.1wt% <i>CPyCl</i> at 0.1(Δ), 1(\circ), 10(\triangleleft), 40(+) <i>rad s⁻¹</i> at 1,4, 10 <i>s⁻¹</i> respectively. The blue shapes are storage moduli (G'_{\perp}) and the Green shapes are the loss moduli (G''_{\perp}). The low-torque limit effects (red dashed) line is calculated from Eqn A.1.	150

A.8	The orthogonal superposition frequency sweeps of 4.1wt% <i>CPyCl</i> at 0, 0.1, 0.4 s^{-1} respectively using strains of 1,2,3,4,5 %. The blue shapes are storage moduli (G'_{\perp}) and the green shapes are the loss moduli (G''_{\perp}). The low-torque limit effects (red dashed) line is calculated from Eqn A.1. . . .	151
A.9	The orthogonal superposition frequency sweeps of 4.1wt% <i>CPyCl</i> at 1, 4, 10 s^{-1} respectively using strains of 1,2,3,4,5 %. The blue shapes are storage moduli (G'_{\perp}) and the green shapes are the loss moduli (G''_{\perp}). The low-torque limit effects(red dashed) line is calculated from Eqn A.1. . . .	152
A.10	The variation of the minimum torque (T_{min}) with shearrate ($\dot{\gamma}$) for OSR.	153
B.1	The determination of the LVR for 4.1wt% <i>CPyCl</i> at 0.1(Δ), 1(\circ), 10(\triangleleft), 100(+) <i>rad s⁻¹</i>	157

Chapter 1

Introduction

This thesis reports the results of three independent studies in the field of rheology/rheometry. The studies are broadly linked to the modelling, characterisation and interpretation of rheological experiments performed on solutions of Worm Like Micelles (which provide a convenient experimental system since their rheology can be described using a discrete relaxation spectrum with a limited number of modes). The thesis begins (in chapter 2) with a broad overview of the basic principles of rheology and rheometry, which is included for completeness. The chemistry, rheology and applications of worm like micelles are then discussed in chapter 3 before each of the three studies is reported as a self contained chapter with relevant literature being reviewed and experimental/numerical procedures being discussed within each chapter.

The first study (chapter 4) explores the use of the Corotation Maxwell (CRM), the Gordon Schowalter (GS) and the Giesekus (GIE) constitutive models for describing the rheology of WLMs in superposition rheometry. Superposition flows involve the application of a unidirectional flow component, which drives the material into a non-equilibrium configuration, upon which is superimposed a small amplitude oscillatory flow which can be used to probe the microstructural changes that occur in response to the unidirectional flow component. The oscillation may be applied in the same direction as the unidirectional flow component (Parallel Superposition Rheometry, PSR) or in a perpendicular

direction (Orthogonal Superposition Rheometry, OSR). It has been suggested in the literature that the CRM is better able to capture the rheology of WLMs than the Giesekus model [58] and, separately, that the GS model may also be used to describe these systems. Expressions for the PSR and OSR superposition moduli appear in the literature for the CRM [24][23] and approximate solutions appear for the Giesekus model [54], however, the GS model remains unexplored in the context of superposition experiments. Hence, novel expressions for superposition moduli for the GS constitutive model are derived and a robust set of experimental data is generated before a comparison of the ability of the various models (CRM/GS/Giesekus) to describe superposition flows is made.

In chapter 5, the impact of inertia on the start-up of stress controlled oscillatory shear is explored. It is well known that data acquired using combined motor transducer rheometers is subject to the influence of inertia. Several authors have explored this in the context of creep experiments in which the coupling of elasticity and inertia gives rise to inertio-elastic ringing. In the context of an oscillatory shear experiment, it is usual to delay the acquisition of data until steady state oscillations have been established. In a recent paper, Hassager derived expressions for the start up of stress controlled oscillations in order to explore the timescale for establishment of the steady state response [41]. He concluded that for a two mode discrete relaxation spectrum, the timescale is set by the longest retardation time. However, Hassager's analysis excluded the impact of inertia on the dynamics. Here, Hassager's analysis is extended to include the impact of inertia which modifies the timescale for establishment of a steady state response. In order to test the model, small amplitude oscillatory shear data is acquired on an aqueous WLM system which is then used to parameterise a two mode discrete relaxation spectrum. Model predictions for the response to start up of oscillatory stress are then compared with transient experimental data over a wide range of frequencies.

In chapter 6, the meaning of the negative values of parallel storage modulus found at low frequencies and sufficiently high shear rates, as observed for parallel superposition experiments in chapter 3 (and often reported in the literature) is investigated via Brownian Dynamics. Such values are also predicted by the Corotational Maxwell

Model (CRM) [24], K-BKZ [85], Gordon-Schowalter (GS) [38], Giesekus (GIE) [36] and Lodge [25] type constitutive models. However, the microstructural origins of the phenomena are not revealed by these constitutive models. Brownian Dynamics (BD) is an established computational tool which allows polymer chain dynamics under various flow conditions to be investigated. Brownian Dynamics simulations for steady shear flows [93], SAOS [22] and orthogonal flows [64] appear in the literature but, to the authors knowledge, no study of parallel superposition flows has been reported. Here, an integration scheme derived by Somasi [81] is used to undertake BD simulations to model polymer behavior under shear flow, SAOS and parallel flows with the aim of investigating the polymer chain dynamics that result in negative values of parallel superposition storage modulus.

Publications resulting from the work presented in chapter 5 is presented in the appendix section. Overall conclusions and recommendations for further work are then presented in chapter 7.

Chapter 2

Basic principles of Rheology/Rheometry

2.1 Introduction

In 1929, E.C Bingham coined the term ‘rheology’ to describe the deformation and flow of materials, drawing inspiration from the Greek word for flow, ‘rheos’ [83]. The field of rheology is concerned with probing, modelling and exploiting the relationship between microstructure, flow and deformation properties in complex fluids. Typical examples include polymer solutions, polymer melts, colloidal suspensions, emulsions and foams. In the classical sense, solids and liquids are distinct descriptions of the physical states of matter; Hooke’s law describes the deformation of solids whilst Newton’s law of viscosity provides a mathematical description of shear fluid flow for simple (i.e. Newtonian) fluids. Many materials can be considered viscoelastic because they display solid-like and liquid-like characteristics depending on the time and length scales of the applied deformation. These materials are termed ‘Complex fluids’. The field of Rheology has three subsections: (i) ‘rheometry’ which is concerned with the experimental characterisation of complex fluids using ‘rheometers’, ii) constitutive modelling which involves the development of mathematical models that describe the flow and deformation that occur in response to an applied stress (or, equivalently, the stresses that evolve in response to an applied flow

condition), and iii) flow modelling which involves the use of constitutive models to predict flows in industrial conditions.

2.1.1 Rheology

Whilst the term ‘rheology’ was not used until 1929, the origins of rheology can be traced back to Issac Newton and Robert Hooke. Hooke’s description of the elastic solid was published before Newton’s study of fluid behaviour was published in the *principia* [91].

Hookean Solids

As shown in Fig 2.1, in the case of Hookean solid, a shear stress, σ applied to the surface $y = d$ leads to an instantaneous deformation . The ideal elastic or Hookean deformation is described with the expression:

$$\sigma = G\gamma \tag{2.1}$$

The Hookean solid displays an instantaneous but finite deformation when shear stress (σ) is applied to a system at rest. The deformation under a shear stress, σ is constant and γ is called the ‘strain’ [8]. A material is said to be purely elastic if it obeys Hooke’s law (Eqn 2.1). G is a constant of proportionality, also know as elastic modulus. The energy used to deform a Hookean body is completely stored within the deformed material and can be recovered without any loss allowing the material to return to its original configuration after the stress is removed.

If a tangential force (F) is applied on a face of the cube, it will displace the ‘Cube Face’ side by distance U (Fig 2.2). This allows stress (σ) to be expressed as the shear force divided by the surface area through which that force is applied, $\sigma = F(N)/A(m^2)$. The shear strain (γ) is defined as the ratio of the deformation to the height of the cube, $\gamma = U/h$.

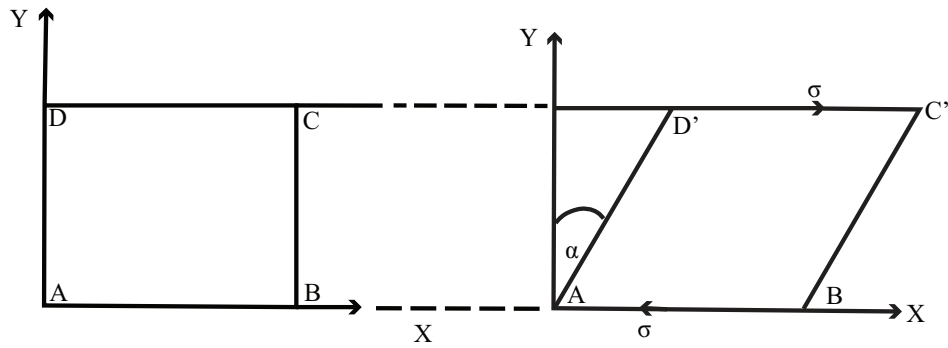


Figure 2.1: The result of the application of a shear stress, σ to a block of Hookean solid. On the application of the stress the material section ABCD is deformed and becomes ABC'D'.

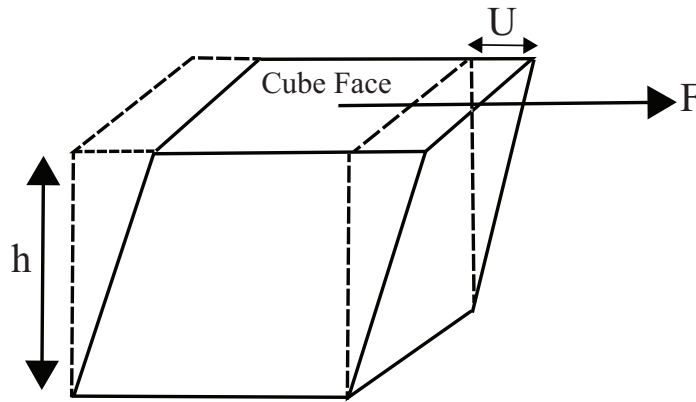


Figure 2.2: Schematic representation of a tangential force on the face of the cube.

Newtonian Liquids

Newtonian liquids display a linear relationship between shear rate ($\dot{\gamma}$) and shear stress (σ). When a shear stress (σ) is applied to a Newtonian system, the shear rate ($\dot{\gamma}$), is instantly established and remains constant until the stress is removed. Examples of Newtonian liquids are glycerine and water. After a load cycle, a Newtonian liquid will not revert back to its original state. Whilst Hookean solids may be characterised by their elastic modulus (G), Newtonian liquids are characterised by a constant (with respect to shear rate) coefficient of viscosity (μ).

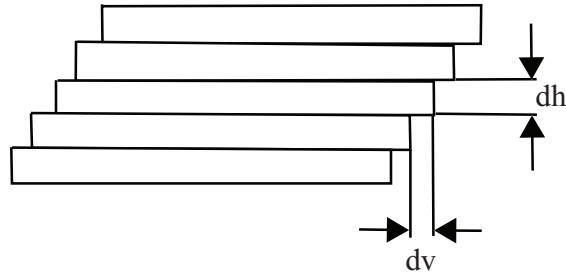


Figure 2.3: Laminar flow in the form of fluid layers

$$\sigma = \mu \dot{\gamma} \quad (2.2)$$

The shear rate ($\dot{\gamma}$), can be defined as the ratio of infinitesimally small velocity difference, dv between two neighbouring flowing layers to the infinitesimally small thickness, dh of one individual flowing layer (Fig 2.3). The velocity difference between neighbouring layers is the same value ($dv = \text{constant}$) because velocity decreases linearly in the shear gap between plates. The layers have the same thickness ($dh = \text{constant}$) and the shear rate is constant everywhere between the plates. Hence, it is clear why the shear rate is often referred to as a velocity gradient.

$$\dot{\gamma} = \frac{dv}{dh} = \text{constant} \quad (2.3)$$

Non-Newtonian Liquids

For non-Newtonian fluids, the relationship between shear stress (σ) and strain rate ($\dot{\gamma}$) is not linear and their apparent viscosity (defined as $\eta(\dot{\gamma}) = \sigma(\dot{\gamma})/\dot{\gamma}$) depends on shear rate. Materials are classed as shear thinning if the viscosity decreases as strain rate increases. Examples include lotions, creams, shampoos and chocolates. Materials are classed as shear thickening if the viscosity increases with shear rate e.g corn starch [19]. A third common class of materials are those that have a yield stress which must be lower than the applied stress to initiate viscous flow e.g sludge [79]. The stress-strain

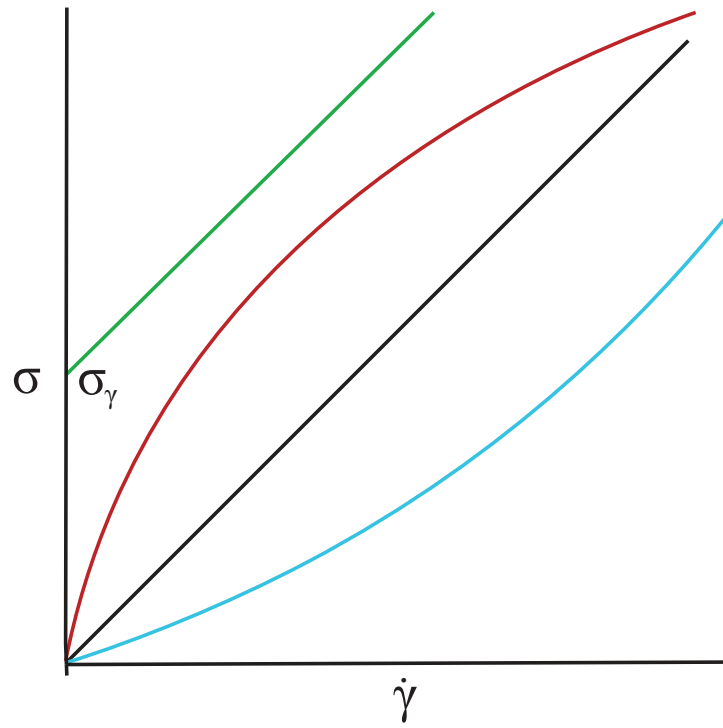


Figure 2.4: Flow curves for Newtonian (black), shear thinning (red), shear thickening (blue) and Bingham plastic (green) behaviour in fluids. The yield stress of the Bingham plastic is represented by σ_γ .

rate diagram, sometimes called a rheogram or flow curves for Newtonian, shear thinning, shear thickening and yield stress fluids are shown in Fig 2.4.

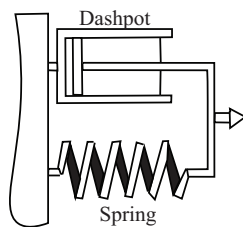


Figure 2.5: The viscoelastic solid contains a spring and dashpot arranged in parallel.

2.1.2 Viscoelasticity

A Material's flow curve has important engineering consequences and the steady flow curve is one of the most common ways to rheologically characterise industrial materials. In reality, many fluids cannot be characterized by viscosity alone since the material's microstructure also imparts an elastic contribution to the flow properties [83]. The term 'viscoelasticity' is the name for this important phenomena. One way of investigating the viscoelastic behaviour of materials is to use oscillatory deformations to probe material functions such as storage modulus (G'), loss modulus, (G'') and complex modulus (G^*) whose meanings are explained in the coming sections. Examples of viscoelastic materials include cement, paint etc. Materials can be classed as viscoelastic solids (VES) or viscoelastic liquids (VEL) depending on their microstructure. These two types of viscoelasticity are often represented by simple mechanical models e.g combinations of springs (elastic component) and dashpots (viscous component) [33].

Viscoelastic solids

The viscoelastic solid (VES) can be represented as a spring and dashpot connected in parallel as shown in Fig 2.5. It is also known as the Kelvin Voigt model. If a constant force, $F = F_0 = \text{constant}$, is suddenly applied to the end of the two component model shown in Fig 2.5 and that force is applied for an unlimited time, both components will resist the movement, with the spring stretching and the dashpot slowly pulling out of the cylinder. This is a continuous process until the spring is stretched to the length corresponding to the applied force. The total force in the system is $F = F_{sp} + F_{dash}$

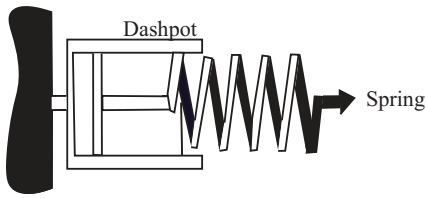


Figure 2.6: The viscoelastic liquid contains a spring and dashpot arranged in series.

where F_{sp} is the force acting on the spring and F_{dash} is the force acting on the dashpot. The Kelvin Voigt material is a solid because the application of constant force leads to a limited displacement.

One of the practical examples of the VES is found in the operation of shock absorbers. In a shock absorber containing a spring and dashpot combination, the spring keeps deflections within a defined limit while the dashpot slows down any rapid deflection movement caused by the impact. After impact, the absorber returns to its original configuration through the spring. In this case, a delayed but completely reversible process is desired.

Viscoelastic Liquid

The viscoelastic liquid (VEL) can be represented by spring and dashpot connected in series. This arrangement is called a Maxwell model. If a constant displacement, $X = X_0 = \text{constant}$, is suddenly created at the end of the jointed two component model in Fig 2.6 and fixed for an unlimited time. This displacement will immediately stretch out the spring. Then, the extended spring will pull the dashpot out of the cylinder and this process will continue for some time because the movement in a viscous liquid is not very fast. This process will continue until the spring comes to an equilibrium state. Hence, the total displacement, $X = X_{sp} + X_{dash}$, where X_{sp} is the displacement of the spring and X_{dash} is the displacement of the dashpot. The Maxwell material is liquid because the application of a constant force leads to unlimited movement of the dashpot.

Silly putty is an example of a viscoelastic liquid (VEL) because it shows elastic behaviour

on small time scales (a heavy mass dropped onto a piece of silly putty will bounce off the putty) and viscous behaviour on a long time scale (it can be squashed flat with pressure applied from a finger) [21].

Obviously, real springs and dashpots cannot be seen under the microscope. The elastic components are representative of any micro-structural system that stores energy. This is potential energy when a polymer segment is being stretched or entropic energy where an isolated polymer random coil being is being deformed from its spherical state. The dashpot represents the dissipation of energy when a system flows through a liquid continuous phase. These models are used when the configuration of springs and dashpots for a liquid is established [7]. In reality, the numbers of elements can be increased without limits resulting in a ‘relaxation spectrum’ that characterises the behaviour of polymers.

2.1.3 Small Amplitude Oscillatory Shear

The linear viscoelastic behaviour of materials can be investigated by applying sinusoidal varying perturbations (stress or strain) called Small Amplitude Oscillatory Shear (SAOS) or ‘Dynamic Mechanical Analysis’. The main advantage of this technique is that it preserves the integrity of the microstructure whereas other techniques like Large Amplitude Oscillatory Shear (LAOS) will break down the microstructure of materials. There are two major types of rheometers that can be used to subject complex fluids to a SAOS test. The Combined Motor Transducer (CMT) rheometer applies a sinusoidal stress wave through the upper geometry to the sample and the deformations are recorded on the same part of the geometry. The Separate Motor Transducer (SMT) rheometer applies a strain to one part and the deformation is recorded on another part of the geometry. It is imperative to conduct SAOS within the Linear Viscoelastic Region (LVR). This is the region in which the dynamic processes within the system can be probed without compromising the microstructure of the sample. In the LVR, the storage modulus (G') and the loss modulus (G'') are independent of the strain amplitude and the oscillatory wave response is sinusoidal [47].

In oscillatory shear, the applied shear strain is expressed as:

$$\gamma(t, \omega) = \gamma_0(\omega) \sin(\omega t) \quad (2.4)$$

where $\gamma(t, \omega)$ is the shear strain, $\gamma_0(\omega)$ is the applied strain amplitude, ω is the frequency and t is the time.

The stress response for ideal elastic (Hookean) solids is expressed as:

$$\sigma(\omega, t) = \sigma_0(\omega) \sin(\omega t) \quad (2.5)$$

For a Newtonian fluid ($\sigma = \mu \dot{\gamma}$), the stress response is 90° out of phase with the strain wave form and can be expressed as:

$$\sigma(\omega, t) = \sigma_0(\omega) \cos(\omega t) \quad (2.6)$$

For a viscoelastic fluid, the applied strain input and the shear stress response are both sinusoidal, however, the stress response is delayed by a phase angle (ψ), which is higher than 0° (Hookean solid) but less than 90° (Newtonian liquid).

$$\sigma(\omega, t) = \sigma_0 \sin(\omega t + \psi(\omega)) \quad (2.7)$$

Storage Moduli

The storage modulus (G') is a measure of the energy stored by the material during the deformation process [8]. It is also the magnitude of the stress in-phase with the strain. At the end of the deformation process, this energy is completely available to drive the reformation or partial reformation process for the material (Eqn 2.8).

$$G' = \frac{\sigma_0}{\gamma_0} \cos(\omega t) \quad (2.8)$$

Loss Moduli

The loss modulus (G'') is a measure of the energy dissipated by the material during the deformation process [7]. It is also the component of the stress which is 90° out of phase with the applied stress waveform (Eqn 2.9).

$$G'' = \frac{\sigma_0}{\gamma_0} \sin(\omega t) \quad (2.9)$$

Complex Modulus

The complex modulus (G^*) is a measure of the overall resistance of a material to deformation (rigidity). It is the ratio of the peak stress (σ_0) to the peak strain (γ_0) [14].

$$G^* = \frac{\sigma_0}{\gamma_0} \quad (2.10)$$

A sinusoidal shear process should be written in complex form. The complex modulus should always be marked with a ‘*’ to differentiate from its shear modulus counterpart. Alternatively, it may be calculated from real and imaginary parts of the response.

$$G^* = G' + iG'' \quad (2.11)$$

2.2 Rheometry

These types of rheometers have been used in this thesis.

ARES-G2 Strain Controlled Rheometer

The ARES-G2 (TA instruments) can apply strain, steady shear, oscillatory strains or a combination of steady shear & oscillatory shear to materials whilst measuring the torque generated. It is a SMT (separate motor and transducer) rheometer, meaning that the motor and transducer are separated from each other. The lower plate consists of a powerful motor that applies the required strain while the torque is recorded by the transducer at the stationery head (Fig 2.7).

The apparatus is also fitted with a Force Rebalance Transducer (FRT) that detects the torque and normal forces from the sample. Servo control systems keep the transducer shaft at a fixed position along the axial and angular directions. Importantly, Vermant et al [89] have shown how the FRT and servo control systems can be modified to perform orthogonal superposition experiments. These type of experiments have been described in chapter 4 . Since the torque sensing occurs at the stationary geometry part, inertia contributions are avoided.

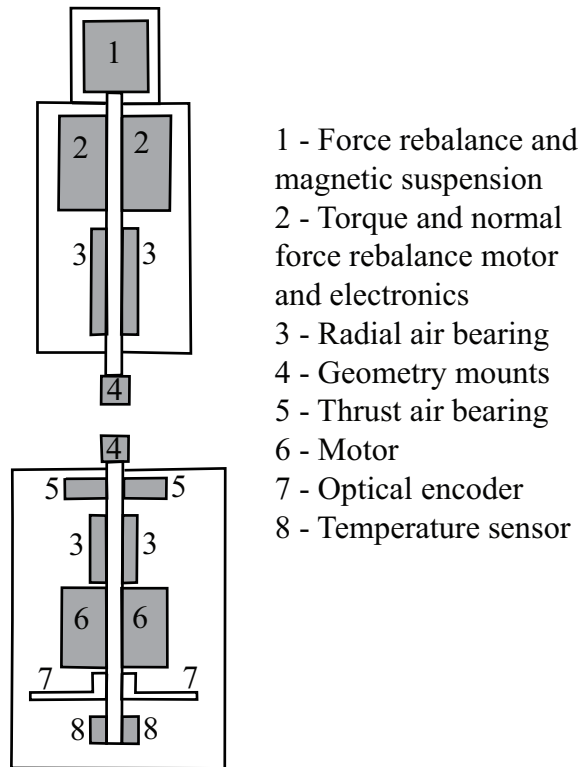


Figure 2.7: A schematic diagram of a Separate Motor Transducer (SMT) rheometer. The motor and the torque sensing element are separate thereby eliminating instrument inertial artefacts from the system.

Discovery Hybrid Rheometer 30 (HR-30)

The HR-30 is a Combined Motor Transducer (CMT) rheometer meaning that the deformation and response is measured by the same part of the equipment (Fig 2.8). This is a stress controlled rheometer that applies stress to the material and the generated strain is measured. The top part of the instrument rotates to generate stress while simultaneously recording the response meaning that inertial forces have to be accounted for by performing calibrations on the instrument. This equipment is capable of performing both stress controlled, (pseudo) strain controlled experiments or a combination of both.

The HR-30 is fitted with an optical dual encoder that improves phase angle precision by 70% which increases the accuracy of G' & G'' [1]. This instrument is capable of producing accurate results under challenging experimental conditions such as low stress, small strains and difficult samples. The dual reader also provides a $5\times$ improvement in displacement resolution, permitting more accurate measurements at lower strains. The magnetic thrust bearings reduce system friction by 70% compared to older models. By eliminating the contributions of high-pressure turbulent air flow from the measurement system, lower torques can be measured reliably and accurately. The advanced drag cup motor reduces system inertia, minimizing corrections to oscillation data, especially at higher measurement frequencies.

Peltier Plate

The peltier plate is used as the temperature control accessory attached via the Smart SwapTM system at the base of the CMT rheometer. It operates using the peltier thermoelectric effect to rapidly cool or warm the surface of the plate. The direction of the current applied between the semiconductors results in either heating or cooling of the peltier plate [94].

2.3 Geometries

Geometries are important in rheological procedures. It is always preferable to have a light geometry for minimal inertia effects but this does not apply to controlled strain

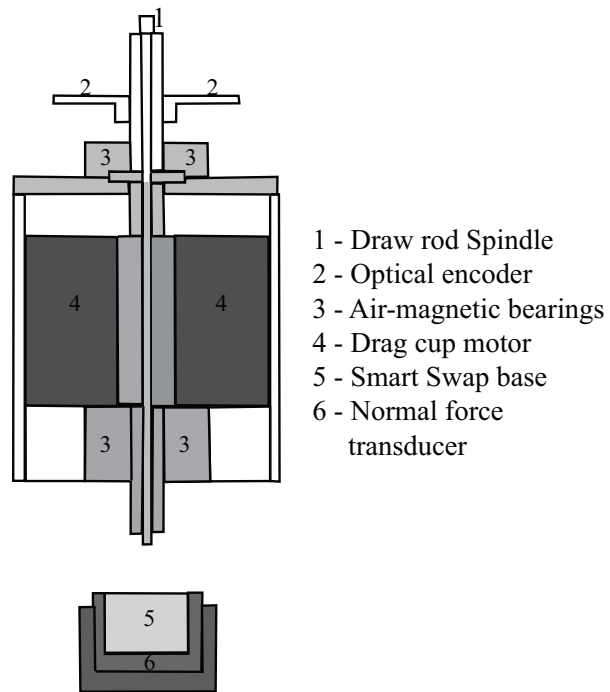


Figure 2.8: A schematic diagram of a Combined Motor Transducer (CMT) rheometer.

rheometers because they have negligible instrument inertia effects. This is because strain is directly applied by the powerful motor and the stress is measured separately by a stationary transducer. The geometry should be chemically inert to the samples. Stainless steel is quite heavy but it is used due to its low thermal expansion coefficient and can be used with a wide range of materials. In the case of aluminium, it is light hence inertia contributions are minimal. It has higher thermal expansion coefficient than steel but a lower chemical resistance. Plastics made from acrylic are transparent hence samples can be visually monitored. They are light hence inertia contributions are minimal to CMT rheometers but they are not suitable for use at high temperatures and have limited chemical compatibility. Geometry factors which depend on the specific geometries are used to convert displacement to strain and torque to stress.

The shear stress for a system is (Eqn 2.12):

$$\sigma = \kappa_{\sigma} M \quad (2.12)$$

where σ is the shear stress, κ_{σ} is the conversion factor which depends on the type of geometry used and M is the torque input. The shear rate is defined as (Eqn 2.13):

$$\dot{\gamma} = F_{\dot{\gamma}} \dot{\theta} \quad (2.13)$$

where $\dot{\gamma}$ is the shear rate, $\dot{\theta}$ is the angular velocity and $F_{\dot{\gamma}}$ is the conversion factor [67].

2.3.1 Parallel plate

The Parallel plate geometry consists of two flat plates positioned parallel to each other (Fig 2.9). The major advantage of a parallel plate geometry is that the gap distance can be easily controlled hence samples with particles are unlikely to get stuck as opposed to the cone and plate (CP) geometries where particles could get stuck in its truncation. However, the applied strain rate varies across the diameter for this geometry meaning that the material at the edges experiences greater strain/strain rate than material towards the centre. Hence, the overall strain is calculated as an average over the entire cross section [3]. The use of silicon oil at the edges will prevent evaporation which can reduce

result accuracy. The general benefits of this geometry include: 1) requires a small volume of sample 2) they can be used over a wide range of viscosity.

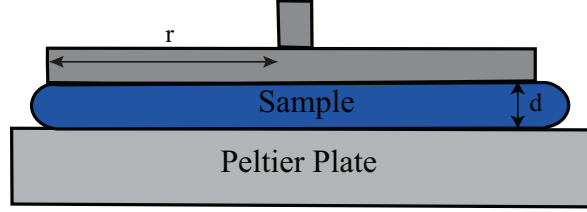


Figure 2.9: Schematic diagram of a parallel plate geometry system with radius (r) and gap (d).

The shear stress conversion factor for a parallel plate system is (Eqn 2.14):

$$\kappa_{\sigma} = \frac{2}{\pi r^3} \quad (2.14)$$

κ_{σ} is the conversion factor which depends on the type of geometry used, r is the radius of the geometry. The shear rate conversion factor for a parallel plate system is defined as (Eqn 2.15) where d is the gap [67]:

$$F_{\dot{\gamma}} = \frac{r}{d} \quad (2.15)$$

2.3.2 Cone and plate (CP) measuring system

The cone and plate measuring system consists of a circular cone with a truncated center, a radius (r) and a cone angle (α) (Fig 2.10). The cone is truncated at the center hence it is advisable to avoid samples with particles as they may lodge in the truncation area causing artefacts or bad data. Due to small gap size, this geometry is limited for use on single-phase homogeneous materials. Systems containing smaller particles up to $5\mu m$ can be measured without any issues. This geometry produces a homogeneous shear rate as the function of a radial position.

The shear stress conversion factor in a CP system is (Eqn 2.16):

$$\kappa_{\sigma} = \frac{3}{2\pi r^3} \quad (2.16)$$

The shear rate conversion factor in a CP system is (Eqn 2.17):

$$F_{\dot{\gamma}} = \frac{1}{\tan \alpha} \quad (2.17)$$

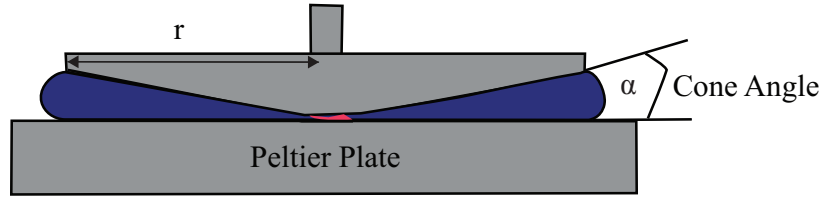


Figure 2.10: A schematic diagram of a cone and plate geometry set up with radius (r) and angle (α). The truncation gap is highlighted in red.

2.3.3 Narrow gap double wall concentric cylinder

Double gap concentric cylinders consists of an inner cylinder (bob) with an inner and outer surface placed in the center of the cup so the cross section of the cup is showing an annular gap (Fig 2.11). This geometry is often used to study low viscosity materials. It has a larger surface area than parallel plates and cone-plate system which is a major advantage hence this system is used for weakly structured materials that are strain sensitive i.e. gelling systems. It has a few disadvantages such as 1) large amount of sample is required 2) clean up after test is tedious and time consuming 3) flow instabilities are often observed when measuring low viscosity liquids at high rotational speeds. A modified version of this geometry is used in orthogonal superposition experiments as explained in chapter 4. The relevant stress and strain factors are given below.

$$\kappa_{\sigma} = \frac{R_4^2 - R_2^2}{4\pi H R_2^2 (R_4^2 + R_2^2)} \quad (2.18)$$

$$F_{\dot{\gamma}} = \frac{R_4^2 + R_2^2}{R_4^2 - R_2^2} \quad (2.19)$$

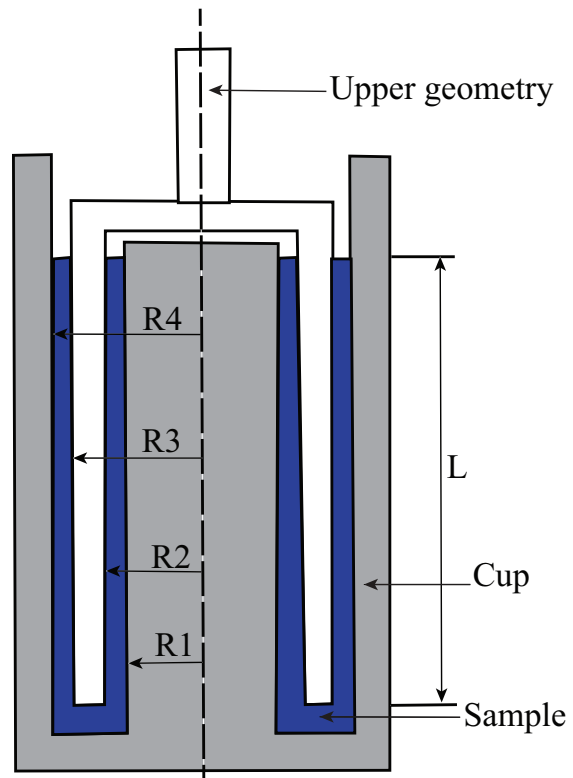


Figure 2.11: Schematic representation of the cross-section of a narrow gap double wall concentric cylinder geometry.

Chapter 3

Worm Like Micelles

3.1 Introduction

Surfactant is the short form of “surface active agent” i.e. active at a surface. Surfactant molecules in low concentrations in a system will absorb onto the surfaces of interface and will alter to a certain degree the interfacial free energies of those surfaces. Surfactants are used in a wide range of different products such as motor oils, detergents and drilling mud in oil production. Some micelles have special properties that allow them to mimic polymer behaviour making them the subject of detailed research in the field of rheology, chemical kinetics and biochemistry. They consist of a hydrophobic tail group which is insoluble and a hydrophilic head group which is soluble (Fig 3.1).

3.2 Micelle Formation

The hydrophobic group of a surfactant alters the structure of water when it is dissolved in water. The water molecules in proximity of the hydrophobic tail arrange themselves into a cage and resulting in the free energy of the system increasing. At the interface, the surfactant molecules have their hydrophobic tail directed away from the water in order to reduce the free energy of the system. The hydrophilic group anchors the surfactant preventing it from breaking away into a separate phase from the system.

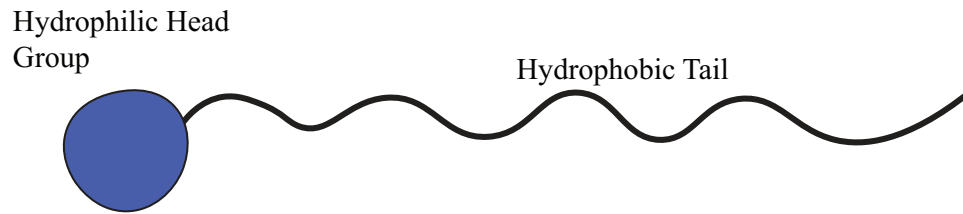


Figure 3.1: Schematic illustration of a surfactant

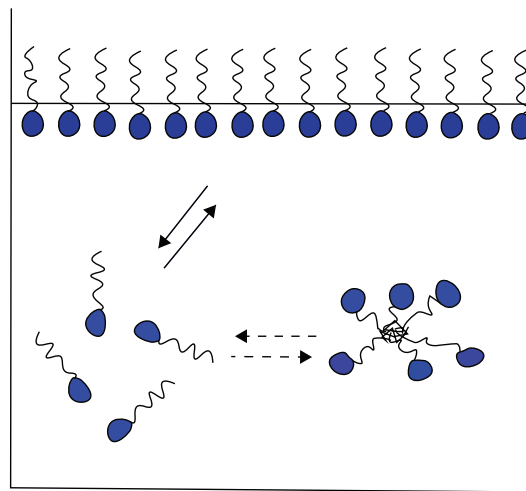


Figure 3.2: Schematic representation of the three states in which surfactant molecules reside in water.

This process reduces the surface tension of water. In general, the denser the surfactant packing at the interface the greater the reduction in surface tension. The aggregation of surfactant into micelles can reduce the distortion of the water structure. The hydrophilic head directs towards the water while the hydrophobic tail directs towards the interior of the cluster. This process is called micellization. Fig 3.2 shows the three ways surfactants behave in aqueous solutions. They either disperse as monomers in the aqueous phase, form micelles or form a film at the air/water interface. The surfactant molecules in the bulk will have a higher energy than those adsorbed at the interface or the ones forming the micelle [43]. The critical packing parameter ($p = v/a_0l$) introduced by Israelachvili [48] allows prediction of the geometry of micellar aggregates. l is the effective maximum

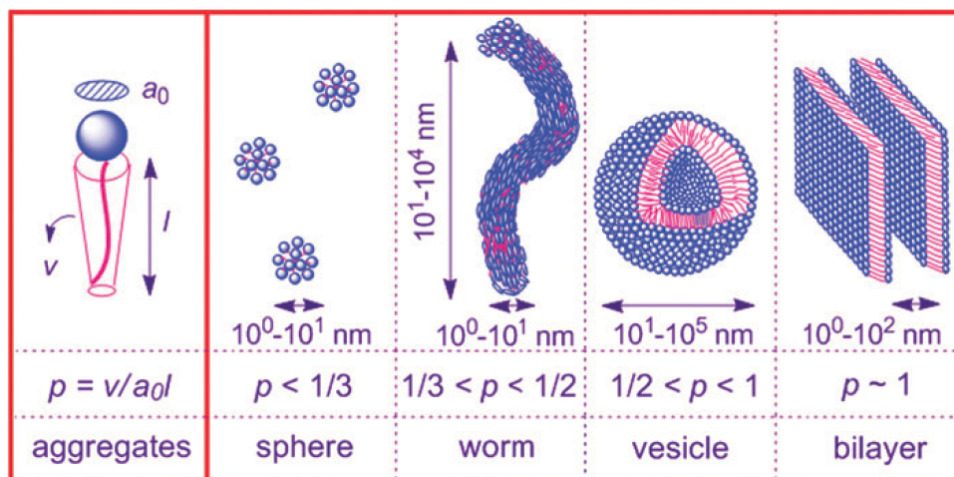


Figure 3.3: Schematic illustration of the relationship between the packing parameter (p) and the morphology of self-assembled surfactant aggregates. Reproduced from ref [18] with permission from the Royal Society of Chemistry.

length of the hydrophobic tail, v is the volume of the hydrophobic tail and a_0 is the effective surface area of per surfactant molecule constituting the aggregate. Surfactants can aggregate into different shapes of micelles. They can be cylindrical, wormlike, vesicles and bilayers. Temperature, salinity, concentration and structure determines which shape (p) will be formed [57]. The amphiphilic compounds are expected to assemble into spherical aggregates when $p < 1/3$, WLMs when $1/3 < p < 1/2$ and lamellar structures for $p \sim 1$ (Fig 3.3).

3.3 Rheological Behaviour of Wormlike Micelles

One of the more commonly studied WLM solutions is a system composed of the surfactant, Cetylpyridinium Chloride (*CPyCl*), Sodium Salicylate (*NaSal*) which is an hydrotropic salt that serves as counterions and Sodium Chloride (*NaCl*). Hydrotropic salts are known to promote micellar growth while simple salts control electrostatic interactions by screening of micellar charge by common-ion effects. The addition of *NaCl* and *NaSal* is known to reduce the Critical Micelle Concentration (CMC) which is the

concentration of surfactant required to promote growth of long WLMs. Viscoelasticity and viscosity are constant in dilute solutions of spherical micelles but by increasing the volume fraction of micelles ($> 30\%$), the viscosity can be increased. In “dilute” worm like micelles, the surfactant concentrations are so low that they do not entangle. Conversely, at sufficiently high concentration (above CMC), the worm like micelles (WLMs) can entangle in a similar manner to the behaviour of concentrated polymer solutions hence they are often called “living polymers”. The length distribution of polymers is determined by chemical synthesis while the length distribution of WLMs can depend on factors such as temperature, salinity and solution composition [16]. Entangled WLM solutions display strong viscoelastic properties like their polymer counterparts hence their rheological behavior can be compared to transient polymer networks.

In cases of high salinity and counter-ion concentration, the Maxwell type behavior with a single relaxation time is observed [30]. The similarities in term of rheological properties of entangled WLMs and concentrated polymers solutions suggest that the reptation theory for polymers can be applied to WLMs. The reptation theory derived by Pierre-Gilles de Gennes, Masao Doi, and Sir Sam Edwards states that polymers in a solution perform snake-like motions within an imaginary confined tube formed by entanglements of individual chains with their neighbour [29][39][26]. However, the dynamic relationship between the scission and recombination of WLMs must be accounted for meaning WLMs have two relaxation processes, one being a reptation type process and the other being the scission and recombination of constitutive units [16]. Cates [15][40][88][80] derived a model used to describe the dynamics of living polymers. This model accounts for both the reptation model of polymers and the reversible scission kinetics of WLMs. The two relevant time scales are the reptation time and the time required for a chain of length (L) to break into two pieces. WLMs are structured by weak forces of attraction that leads to continuous breaking and reformation with time whereas polymers have a backbone of covalently bonded and rigid form. WLMs can release stress through reptation by Brownian motion [57], breaking and reforming in a lower stress state [76] or when two entangled micelles pull right through each other, eliminating the entanglement point (ghost like crossing) [78]. The reptation and breakup relaxation mechanisms have characteristic time scales of t_{rep} and t_{br} respectively [53].

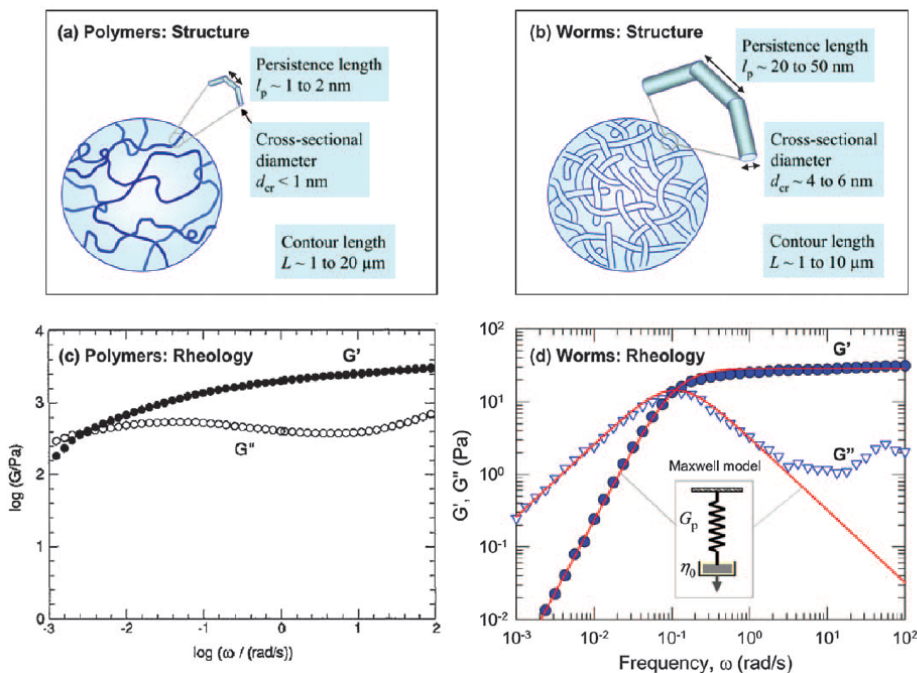


Figure 3.4: Contrasting the structure and rheology of polymers (in solution) and wormlike micelles. Reproduced from ref [30] with permission from the Royal Society of Chemistry.

Cates [15][16] postulated that the t_R (relaxation time) is a function of the t_{br} (time required for breakage and recombination) and t_{rep} (time required to reptate). The WLMs reptate while breaking and recombining which is an additional mode for stress relaxation. This allows for a single relaxation time (t_R) that involves both processes as a geometric mean of t_{br} and t_{rep} .

$$t_R = \sqrt{t_{br}t_{rep}} \quad (3.1)$$

In Fig 3.4, typical values for structural length scales are indicated in (a) for polymers and (b) for WLMs. Typical data from dynamic rheology are shown for the two systems in (c) and (d), with the elastic modulus, G' (filled symbols) and the viscous modulus, G'' (unfilled symbols) plotted against frequency. The data in (c) are for polystyrene of

$M = 4.7$ million at a concentration of 13.9 wt% in di(2-ethylhexyl)phthalate. Reprinted from K. Almdal et al., *Polym. Gels Networks*, 1993, 1, 5–17. According to the authors, this sample can be considered a gel (however, this is a contentious statements as the data does not display the characteristics of gel like behaviour) . The data in (d) are for WLMs formed by 100 mM *CPyCl* and 60 mM NaSal at a temperature of 20°C ; this data is replotted from the paper by Rehage and Hoffmann [76]. The solid lines are fits to the Maxwell model for viscoelastic fluids Eqn (3.2 & 3.3) . The Maxwell model combines an elastic spring and a viscous dashpot in series, as shown in the inset.

The spring has an elastic modulus, G and the dashpot has a viscosity, η_0 . The relaxation time is given as $t_R = Gp/\eta_0$. The relaxation time is the time that characterises a material’s stress relaxation after deformation i.e. the time it takes for an applied stress to dissipate in a viscoelastic material [69].

$$G'(\omega) = \frac{G_p \omega^2 t_R^2}{1 + \omega^2 t_R^2} \quad (3.2)$$

$$G''(\omega) = \frac{G_p \omega t_R}{1 + \omega^2 t_R^2} \quad (3.3)$$

Fig 3.4d shows how the rheology of typical WLMs fit with the Maxwell model. The important features are the elastic behaviour at high frequencies, ω (short timescales), $G' = \text{constant}$ and also $G' > G''$. Second, the viscous behavior at low frequencies, ω (long time scales) $G'' > G'$. Since both modulus are affected by frequency, the response is termed viscoelastic. The relaxation time (t_R) of a Maxwell fluid is given by $t_R = 1/\omega_c$. ω_c is the crossover frequency where G'' has its peak and G' crosses that peak. The WLM in Fig 3.4 have $\omega_c = 0.1 \text{ s}^{-1}$ hence $t_R = 10 \text{ s}$. Polymer solutions often have high molecular weights. For example, Polystyrene solutions which have $M = 4.7$ million [4] are classified as “Ultra high molecular weight”. The PS solutions show similar behavior of the WLM in terms of the behavior at high and low frequencies. The response does not follow that of a Maxwell fluid as evidenced by the shapes of the G' and G'' curves in Fig 3.4c. It has a spectrum of relaxation times instead of a single relaxation time. The crossover

frequency, ω_c for polymers is generally accepted as the longest relaxation time [59][57]. The question of why polymer solutions have a spectrum whereas WLMs have a single relaxation, t_R was answered by Cates [15]. The fundamental difference between WLMs and polymers is that WLMs are held together by weak forces of attractions which allows a given worm to break off, diffuse through water and latch on to another worm, hence the term “living polymers”. For PS solutions, the longest relaxation time is $t_R = 200\text{ s}$. It is emphasised [30] “if reptation was the only mode for stress relaxation, WLMs would have extremely long ($> 100\text{ s}$) relaxation times. It is only because WLMs break and recombine that their relaxation times are shorter.”

WLMs are used in multiple industrial processes hence the study of their chemical and rheological properties is important. In Oil and Gas industries, WLMs combine with oil produced from fractures to form small spherical micelles or microemulsions [63][60] that have lower viscosity hence facilitating the flow of residues out of fractures. It is known that fluids flowing through a pipe will experience a drag force caused by the conduit’s surface expressed as a drop in pressure in the fluid [97]. Polymers can be used as drag reducers but are not effective because the chains of high molecular weight polymers (polyacrylamide and polyisobutylene) [84] suitable for this purpose are broken down under high mechanical shear experienced in pipelines carrying crude oil. WLMs, on the other hand, are effective drag reducing agents because they have rapid self reparability after being subjected to the mechanical constraints of a pipeline. WLMs may then be suitable for applications in recirculating flow systems or multi-pump station pipeline flow systems [97].

3.4 Shear Banding Phenomena

Shear banding is the appearance of flow regimes with distinct local shear rates. It is the spontaneous separation of flows approximating simple shear into separate regions each with an individual shear rate [17]. A material can be suspected to shear band when the stress plateau hardly or slightly increases over range of shear rates. Shear banding can

be investigated by stress measurements [9][10]. Published works by Hu [45] & Cheng [17] have investigated the behaviours of shear banding and shear thinning entangled micellar solutions focusing on how WLM systems transition from shear thinning to shear banding for a range of concentrations of the same system (*NaSal*, *NaCl*, & *CPyCl*). By constructing the local flowcurve from the local stress and shear rate via the velocity profile, the authors showed that the slope of the stress plateau decreases with increasing surfactant (Cetylpyridium chloride) concentration and becomes zero at a critical concentration of 4.9wt%. Above this critical concentration, the local flow curve becomes discontinuous, suggesting a non-monotonic constitutive relationship, which signifies a transition from shear thinning to shearbanding in the system. When the surfactant concentration is increased, the entanglement and alignment of wormlike micelles become more pronounced. At higher surfactant concentrations, the network of micelles becomes more interconnected, creating regions of high viscosity. In shear banding, these regions coexist with regions of lower viscosity that experience shear thinning more readily. The material separates into alternating layers of higher viscosity (often referred to as bands) and lower viscosity within the flowing solution. The regions with higher viscosity essentially act as barriers to the flow, creating localized resistance and leading to this banding pattern [37]. Hence, above CMC (critical micelle concentration) > 4.9wt%, this material configuration will shear band concluding that 4.1wt% and 5.9wt% *CPyCl* solution are shearthinning (ST) and shearbanding (SB) materials respectively.

Chapter 4

Evaluation of Constitutive Models for WLMs

4.1 Superposition Rheometry

Superposition rheometry is a technique for probing the weakly nonlinear properties of viscoelastic materials by superimposing a time dependent perturbation in parallel (PSR) or orthogonal (OSR) direction in bulk flow on a steady simple shear. A small amplitude oscillatory perturbation of amplitude (γ_0) and angular frequency (ω) is superimposed upon a unidirectional flow with a constant strainrate ($\dot{\gamma}$). This was discussed by Yamamoto [95] where he derived the integral relationship between dynamic superposition modulus and rate dependent relaxation spectra in the parallel and orthogonal superposition of oscillatory shear on steady shear flow. The kinematics of superposition rheometry are:

$$x_1(t) = x_1(t') + [\dot{\gamma}(t - t') + a(e^{i\omega t} - e^{i\omega t'})]x_2(t') \quad (4.1)$$

$$x_2(t) = x_2(t') \quad (4.2)$$

$$x_3(t) = x_3(t') + b(e^{i\omega t} - e^{i\omega t'})x_2(t') \quad (4.3)$$

In PSR, the main flow and the small amplitude perturbation are applied in the same direction, where $a = \gamma_0$ & $b = 0$ in Eqn 4.1 & Eqn 4.3. In OSR, the main flow and the small amplitude perturbation are applied at the same time but in mutually perpendicular directions, where $a = 0$ & $b = \gamma_0$ in Eqn 4.1 & Eqn 4.3. Since the main flow and the small amplitude perturbation are in the same direction for the PSR, there is a coupling of the flow components. The accepted symbols for parallel and orthogonal flows are the subscripts \parallel and \perp respectively [71].

$$G'_{\parallel}(\omega, \dot{\gamma}) = \int_{-\infty}^{\infty} \left[H(\tau, \dot{\gamma}^2) + 4\dot{\gamma}^2 \frac{\partial H(\tau, \dot{\gamma}^2)}{\partial \dot{\gamma}^2} \frac{1}{1 + \omega^2 \tau^2} \right] \frac{(\omega\tau)^2}{1 + \omega^2 \tau^2} d \ln \tau \quad (4.4)$$

$$G''_{\parallel}(\omega, \dot{\gamma}) = \int_{-\infty}^{\infty} \left[H(\tau, \dot{\gamma}^2) + 2\dot{\gamma}^2 \frac{\partial H(\tau, \dot{\gamma}^2)}{\partial \dot{\gamma}^2} \frac{1 - \omega^2 \tau^2}{1 + \omega^2 \tau^2} \right] \frac{\omega\tau}{1 + \omega^2 \tau^2} d \ln \tau \quad (4.5)$$

Eqn 4.4 and Eqn 4.5 are expressions of parallel superposition moduli derived by Yamamoto [95] containing the perturbation spectrum associated with each shear rate ($H(\tau, \dot{\gamma}^2)$), but also the derivatives of the spectra. The perturbation spectra decreases with increasing shear rate which in turn leads to a decrease in parallel superposition moduli. In some cases, the magnitude of the derivative term can become larger than the first term resulting in a negative superposition moduli [89][13]. This means PSR moduli cannot be interpreted in the same way as its SAOS counterparts, G' & G'' .

The orthogonal moduli can be expressed as [89]:

$$G'_{\perp} = \int_{\infty}^{-\infty} H(\tau, \dot{\gamma}^2) \frac{(\omega\tau)^2}{1 + \omega^2 \tau^2} d \ln \tau \quad (4.6)$$

$$G''_{\perp} = \int_{\infty}^{-\infty} H(\tau, \dot{\gamma}^2) \frac{\omega\tau}{1 + \omega^2 \tau^2} d \ln \tau \quad (4.7)$$

In OSR, the two flows are in different directions, hence coupling does not occur. It has been claimed that OSR moduli are comparable to the theory of linear viscoelasticity where the physical meaning of storage and loss moduli are retained. The OSR storage and loss moduli, Eqn 4.6 and Eqn 4.7 respectively, do not violate the Kramers-Krönig

relationship. The differences discussed above show that it is not feasible to make a direct comparison between both OSR and PSR data. It is however possible to convert PSR to OSR data and vice versa [23]. The ability to switch between equivalent versions of PSR and OSR moduli gives the opportunity to derive new information by comparing data in both configurations.

The Kramers-Krönig relations are an important rule in physics that state that the real part of a signal can be represented in terms of the imaginary part and vice versa. According to Vermant [89], derivative terms in the storage and loss modulus differ otherwise it would be straightforward to obtain PSR storage modulus in terms of PSR loss modulus and vice versa. The OSR does not violate this rule. This is one of the reasons why PSR is less used than OSR despite its ease of access (OSR requires expensive specialized equipment). Recent publications by Curtis & Davies [23] have shown that the Kramers-Krönig relations for PSR flows are not violated. The schematic of the operating principle of a standard orthogonal kit is described in Fig 4.1. The axial motion of Couette bob causes the oscillatory shear deformation orthogonal to the main flow while the rotation of the Couette cup causes the steady shear flow. Vermant [89] used a hollow inner cup and a modified force rebalance transducer to perform orthogonal superposition measurements (OSR). The axial motion required to perform OSR experiments may cause annular pumping flow by displacing the fluid under the edge of the hollow bob leading to distortions in the flow field [98]. To minimize the pumping effect during OSR experiments, an opening is made in the inner wall of the cup that connects with a liquid reservoir in the center of the cup [89]. The schematic of the double walled Couette cell is shown in Fig 4.2 [86]. The bob in Fig 4.2a has 3 rectangular openings located at the top. The inner cylinder of the cup has 3 rectangular openings in Fig 4.2b. The outer cylinder of the cup can be removed for cleaning purposes. The characteristic geometric dimensions are shown in Fig 4.3 i.e., the inside cup radius (R_1), inside bob radius (R_2), outside bob radius (R_3), outside cup radius (R_4), inner cylinder height (l) and the immersed height (h).

Superposition rheometry has been used to study the dynamics of worm like micelles (WLMs) via the Giesekus model [54][50], the shearbanding in WLMs [5] more precisely

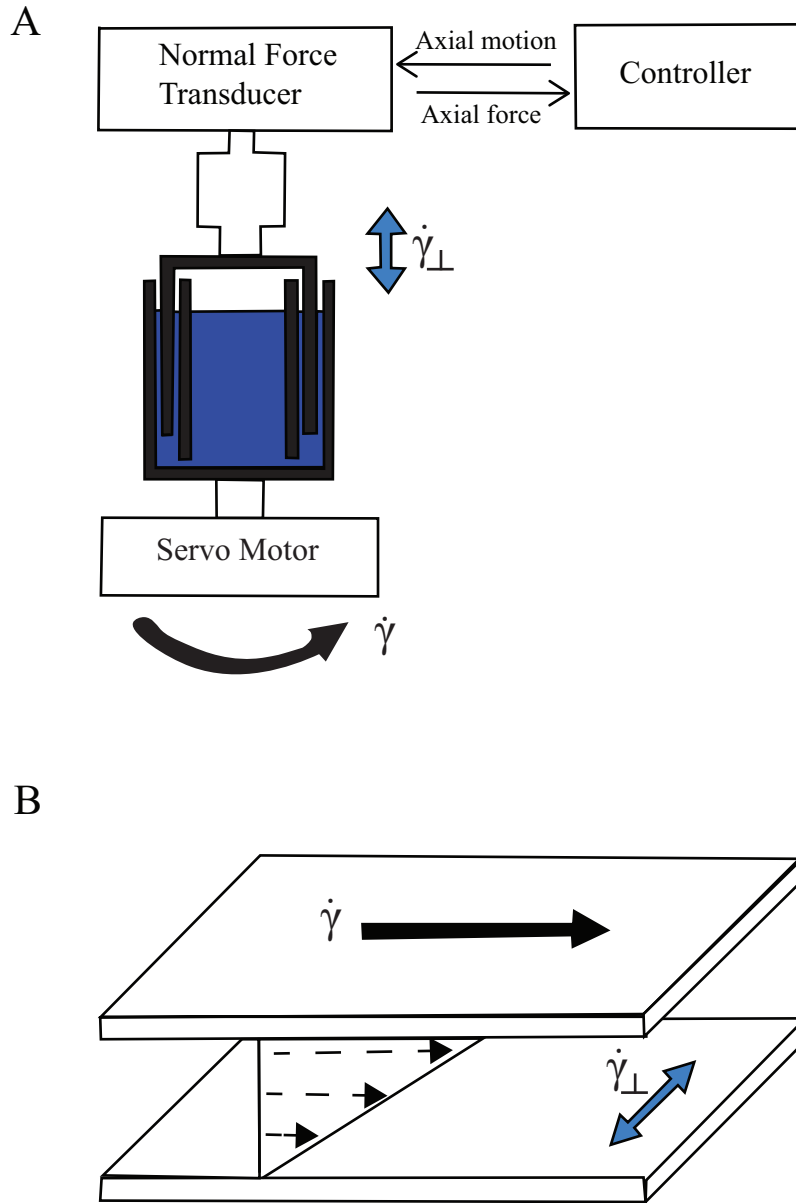


Figure 4.1: a) The orthogonal superposition equipment with a double wall Couette cell that has an opening in the inner wall of the cup connecting to the liquid reservoir in the center of the cup b) This flow is achieved by superimposition of an oscillatory flow in the orthogonal direction ($\dot{\gamma}_{\perp}$) onto the steady shear flow ($\dot{\gamma}$).

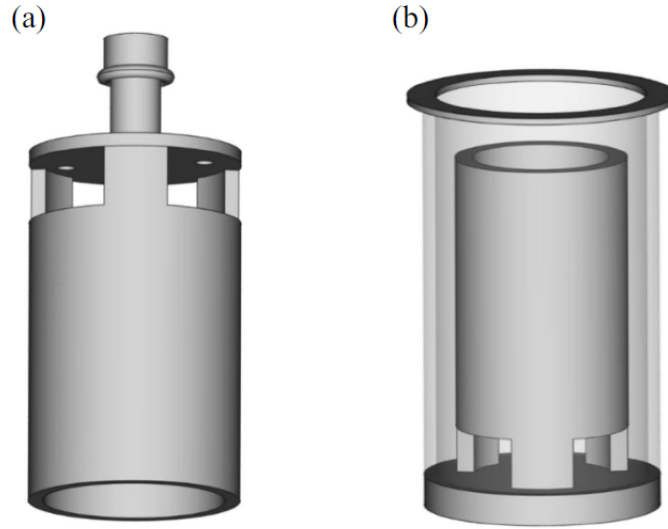


Figure 4.2: Schematics of (a) the bob, (b) the double-wall cup (the outer cylinder is shown as translucent). Reproduced with permission from Ref [86].

to access the dynamics of the interface between shear bands, the anisotropy in liquid crystalline polymers [90][68], structural changes during flow in polymeric fluids [72][13][65] and colloidal suspensions [66][98][28] etc. These works represent evidence of the validity of superposition rheometry as another rheological tool apart from LAOS (large amplitude oscillatory shear) to probe non linear behavior of complex fluids and investigate anisotropy, the property of a material which allows it to change or assume different properties in different directions. In the following sections, parallel and orthogonal superposition experiments are used to probe the structural changes of WLMs (living polymers) during flow. The studies aimed to assess the ability of the Giesekus, Corotational Maxwell and the Gordon Schowalter models to capture shear thinning and shear banding WLM dynamics under flow.

Models

Recent works have focused on using superposition moduli to probe anisotropy but it is possible to use superposition rheometry to assess the ability of constitutive models to describe particular fluids. In fact, this was noted as the main utility of the technique by

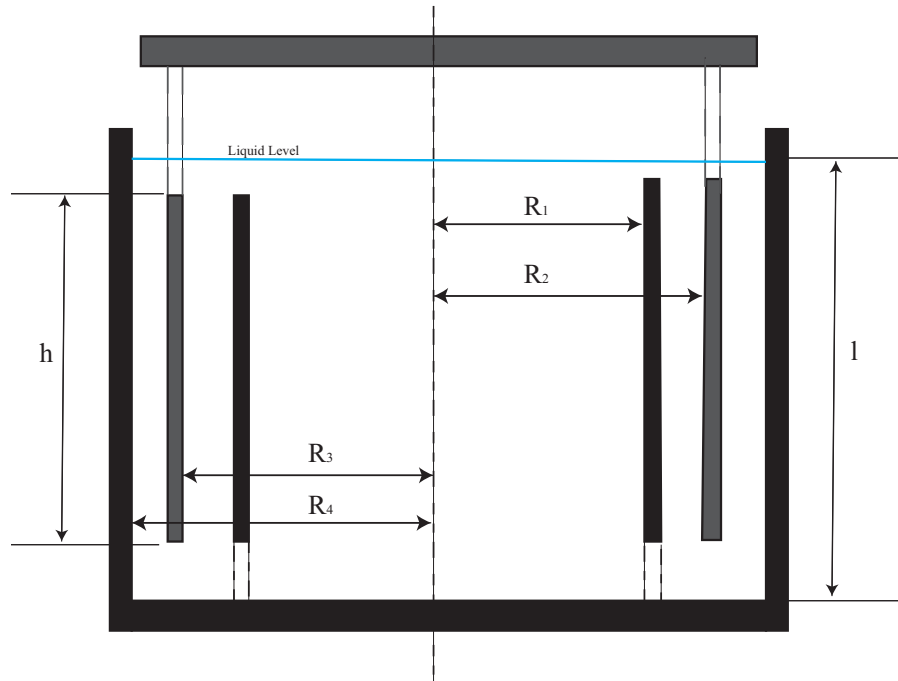


Figure 4.3: The vertical cross section of the OSP double-wall concentric cylinder geometry, displayed for the 0.5mm gap cell. The center cylinder (bob) is shown in gray. The outer and inner cylinders (cup) are shown in black. The top openings on the bob and bottom openings on the cylinder are depicted by dashed lines.

Yamamoto [95]. In this work, the ability of the Giesekus (GIE), Corotational Maxwell (CRM) and Gordon-Schowalter (GS) constitutive models to describe the dynamics of a wormlike micellar system (Cetylpyridinium Chloride/Sodium Salicylate) in superposition flows will be assessed. Expressions for the CRM were derived by Curtis & Davies [25] while the expressions for the GS model are derived, for the first time in section 4.1. Expressions for the superposition moduli of the GIE model were developed by Kim [54] and their expressions are used herein. The dynamics of a WLM described by the GIE model is analysed using a dimensionless mobility parameter (α) whereas the CRM and GS models are analysed under i) weakly and ii) strongly non-linear conditions. These conditions are defined by Malkin [61] who considered flows to be weakly non-linear where the underlying relaxation spectrum is not modified by the flow but strongly non-linear where the materials microstructural response to the imposed flow condition generates changes in its underlying relaxation properties - i.e. the flow shear stresses can no longer be predicted from the linear relaxation spectrum. The GS model is equivalent to the Johnson-Segalman (JS) model in the limit of a single mode [75] but there are subtle differences. Whilst the GS model is a differential model derived by introducing the GS convected derivative, the Johnson-Segalman model (JS) is an integral model derived by admitting a non-affine velocity gradient to the Lodge integral constitutive equation. Ramlawi *et. al* [75] stated in their study of the weakly non linear response of the JS model, the JS model is more general and is not restricted to a particular microstructure unlike its GS model counterpart which was derived for polymeric materials. The terms GS and JS have been used interchangeably in literature. In this work, the differential model is the basis hence the GS model will be referred throughout. Both models contain a “slip” or “affinity” parameter (a) which permits the polymer chains and the bulk solvent to experience different velocity gradients - i.e. the polymer chains slip relative to the velocity gradient imposed by the bulk deformation. If $a = 0$ both models reduce to the corotational Maxwell model, whilst for $a = 1$ the models reduce to the Upper Convected Maxwell model. A two mode spectrum with breaking and reptation times is used for modelling. The breaking time can be obtained from the minimum of the $G''(\omega)$ data [88][51] and in the present study is treated as a fixed parameter, the mode viscosity is allowed to vary. The other mode, often interpreted as being sensitive to reptation, is

allowed to vary with two degrees of freedom (λ_2, η_1).

Giesekus model (GIE)

Expressions for the parallel and orthogonal superposition moduli for the Giesekus model exist in the literature. The reader is referred to [54] for details of the derivation but the major equations are outlined below. For the quiescent case (unidirectional flow), the Giesekus model reduces to the standard Maxwell equations. $\chi = \lambda\omega$ is the reduced frequency, λ is the relaxation time, η_s is the effective medium viscosity, G' and G'' are the storage and loss modulus respectively.

$$G' = \frac{G\chi^2}{1 + \chi^2} \quad (4.8)$$

$$G'' = \frac{G\chi}{1 + \chi^2} + \eta_s\omega \quad (4.9)$$

The following equations can be used to fit experimental flow sweep data using the following equations derived by Giesekus [36].

$$\eta_0 = \lambda G \quad (4.10)$$

$$De = \lambda \dot{\gamma} \quad (4.11)$$

$$n_2 = \frac{1 - \Lambda}{(1 + (1 - 2\alpha)\Lambda)} \quad (4.12)$$

$$\Lambda = \left(\frac{1}{8\alpha(1 - \alpha)De^2} \left[\sqrt{1 + 16\alpha(1 - \alpha)De^2} - 1 \right] \right)^{1/2} \quad (4.13)$$

$$\sigma_{total} = \frac{\eta_0}{\lambda} \left[\frac{1 - n_2^2}{1 + (1 - 2\alpha)n_2} \right] \lambda \dot{\gamma} \quad (4.14)$$

$$\eta = \frac{\sigma_{total}}{\dot{\gamma}} \quad (4.15)$$

Where Λ is the effective relaxation time reduced by the relaxation time. It is important to note that the expression for Λ as defined by Kim [54] and Giesekus [36] is only valid for $0 < \alpha < 1$. When $\alpha = 0$ or $\alpha = 1$, the expressions reduce to the Upper Convected (UCM) or the CRM models respectively. In these cases, the expression for Λ is not required. De is the reduced shearrate, n_2 is the reduced second normal stress difference, η_0 is the zero shear frequency, λ is the effective relaxation time reduced by the relaxation time and α is the dimensionless mobility factor that ranges from zero to unity.

It is also possible to use analytical equations derived by Kim [54] to calculate the shear rate dependent response of PSR and OSR. It is important to note that there is an error in the published paper which was corrected by private correspondence with the author [55]. It is well established that PSR and OSR are not equivalent due to different tensor configurations so it follows that the analytical representations of both models will differ. The analytical descriptions of OSR and PSR for the Giesekus model are respectively:

$$G'_{\perp} = Gg'_{\perp} = G \frac{A\chi^6 + B\chi^4 + C\chi^2}{\chi^6 + D\chi^4 + E\chi^2 + F} \quad (4.16)$$

$$G''_{\perp} = Gg''_{\perp} + \eta_s\omega = G \frac{H\chi^5 + I\chi^3 + J\chi}{\chi^6 + D\chi^4 + E\chi^2 + F} + \eta_s\omega \quad (4.17)$$

$$G'_{\parallel} = Gg'_{\parallel} = G \frac{K\chi^6 + L\chi^4 + M\chi^2}{\chi^6 + N\chi^4 + O\chi^2 + P} \quad (4.18)$$

$$G''_{\parallel} = Gg''_{\parallel} + \eta_s\omega = G \frac{Q\chi^5 + R\chi^3 + S\chi}{\chi^6 + N\chi^4 + O\chi^2 + P} + \eta_s\omega \quad (4.19)$$

where $\chi = \lambda\omega$ is the reduced frequency and η_s is the effective medium viscosity. The coefficients indicated by capital letters are functions of the parameter α , λ , and plateau modulus (G) as well as the shear rate ($\dot{\gamma}$) and are given in the Appendix A.

Corotational Maxwell Model

The expressions for the parallel and orthogonal superposition moduli for the Corotational Maxwell model have been derived by Curtis & Davies [23] where a detailed derivation is published. A brief description of the results are presented below.

The Cauchy stress tensor can be expressed as:

$$\boldsymbol{\sigma} = -p\mathbf{I} + \boldsymbol{\tau} \quad (4.20)$$

for which the extra stress tensor, $\boldsymbol{\tau}$, can be written as:

$$\boldsymbol{\tau} + \lambda \frac{\mathcal{D}\boldsymbol{\tau}}{\mathcal{D}t} = \eta_0 \dot{\boldsymbol{\gamma}} \quad (4.21)$$

for the Corotational Maxwell model, the objective derivative is the corotational, or Jaumann derivative defined as:

$$\frac{\mathcal{D}\boldsymbol{\tau}}{\mathcal{D}t} = \frac{D\boldsymbol{\tau}}{Dt} + \frac{1}{2}[\boldsymbol{\omega} \cdot \boldsymbol{\tau} - \boldsymbol{\tau} \cdot \boldsymbol{\omega}] \quad (4.22)$$

For a parallel superposition flow, with arbitrary superimposed perturbation, $\epsilon\dot{\phi}(t)$ (e.g. oscillation, step, chirp) to the viscometric flow (characterised by a steady, unidirectional, shear rate $(\dot{\gamma})$). The velocity field can be written as:

$$\mathbf{u}_{\parallel} = [(\dot{\gamma} + \epsilon\dot{\phi})y, 0, 0]^T \quad (4.23)$$

whilst for an orthogonal experiment,

$$\mathbf{u}_{\perp} = [\dot{\gamma}y, 0, \epsilon\dot{\phi}y]^T \quad (4.24)$$

The vorticity and strain rate tensors can be written as:

$$\boldsymbol{\omega} = \nabla\mathbf{u} - \nabla\mathbf{u}^T \quad (4.25)$$

and

$$\dot{\boldsymbol{\gamma}} = \nabla \mathbf{u} + \nabla \mathbf{u}^T \quad (4.26)$$

For such flows, the material derivative in Eqn 4.22 reduces to the normal derivative and using a power series expansion about the viscometric flow case, the following expressions for the parallel and orthogonal moduli [23] can be written:

$$G'_{\parallel}(\dot{\boldsymbol{\gamma}}, \omega) = \frac{\eta_0 \omega^2 \lambda_1 (1 + \omega^2 \lambda_1^2 - 3 \lambda_1^2 \dot{\boldsymbol{\gamma}}^2)}{(1 + \lambda_1^2 \dot{\boldsymbol{\gamma}}^2) [(1 + \lambda_1^2 \dot{\boldsymbol{\gamma}}^2 - \omega^2 \lambda_1^2)^2 + 4 \omega^2 \lambda_1^2]} \quad (4.27)$$

$$G''_{\parallel}(\dot{\boldsymbol{\gamma}}, \omega) = \frac{\eta_0 \omega (1 + \omega^2 \lambda_1^2 - \lambda_1^2 \dot{\boldsymbol{\gamma}}^2)}{(1 + \lambda_1^2 \dot{\boldsymbol{\gamma}}^2 - \omega^2 \lambda_1^2)^2 + 4 \omega^2 \lambda_1^2} \quad (4.28)$$

$$G'_{\perp}(\dot{\boldsymbol{\gamma}}, \omega) = \frac{\eta_0 \omega^2 \lambda_1}{1 + \lambda_1^2 \dot{\boldsymbol{\gamma}}^2} \left[\frac{(1 + \frac{1}{2} \lambda_1^2 \dot{\boldsymbol{\gamma}}^2) \omega^2 \lambda_1^2 + (1 + \frac{1}{4} \lambda_1^2 \dot{\boldsymbol{\gamma}}^2) (1 - \frac{1}{2} \lambda_1^2 \dot{\boldsymbol{\gamma}}^2)}{(1 + \frac{1}{4} \lambda_1^2 \dot{\boldsymbol{\gamma}}^2 - \omega^2 \lambda_1^2)^2 + 4 \omega^2 \lambda_1^2} \right] \quad (4.29)$$

$$G''_{\perp}(\dot{\boldsymbol{\gamma}}, \omega) = \frac{\eta_0 \omega}{1 + \lambda_1^2 \dot{\boldsymbol{\gamma}}^2} \left[\frac{(1 + \frac{1}{4} \lambda_1^2 \dot{\boldsymbol{\gamma}}^2)^2 + \omega^2 \lambda_1^2 (1 + \frac{3}{4} \lambda_1^2 \dot{\boldsymbol{\gamma}}^2)}{(1 + \frac{1}{4} \lambda_1^2 \dot{\boldsymbol{\gamma}}^2 - \omega^2 \lambda_1^2)^2 + 4 \omega^2 \lambda_1^2} \right] \quad (4.30)$$

Parallel Superposition Moduli for the Gordon-Schowalter Model

The GS Model, introduced by Gordon & Schowalter [38], allows the polymer and solvent to experience a non-affine deformation with inclusion of a “slip parameter” ($-1 \leq a \leq 1$). This model recovers the Upper Convected, Lower Convected and Corotational Maxwell models when $a = -1, 1$ and 0 , respectively. To derive expressions for the GS superposition moduli, the Cauchy stress tensor can be written as Eqn 4.20 and the extra stress tensor can be written as Eqn 4.21.

The objective derivative is the Gordon-Schowalter[38] derivative defined as:

$$\frac{\mathcal{D}\boldsymbol{\tau}}{\mathcal{D}t} = \frac{D\boldsymbol{\tau}}{Dt} + \frac{1}{2} [(\boldsymbol{\omega} - a\dot{\boldsymbol{\gamma}}) \cdot \boldsymbol{\tau} - \boldsymbol{\tau} \cdot (\boldsymbol{\omega} + a\dot{\boldsymbol{\gamma}})] \quad (4.31)$$

As for the CRM, for superposition flows, the material derivative in Eqn 4.31 reduces to the normal derivative such that:

$$\frac{\mathcal{D}\boldsymbol{\tau}}{\mathcal{D}t} = \frac{d\boldsymbol{\tau}}{dt} + \frac{1}{2} [(\boldsymbol{\omega} - a\dot{\boldsymbol{\gamma}}) \cdot \boldsymbol{\tau} - \boldsymbol{\tau} \cdot (\boldsymbol{\omega} + a\dot{\boldsymbol{\gamma}})] \quad (4.32)$$

The extra stress tensor, $\boldsymbol{\tau}$ is symmetric and may be written as six component equations. For the parallel superposition case, (where the velocity field is defined by Eqn 4.23) the constraints $\tau_{13} = \tau_{23} = \tau_{33} = 0$ is admitted and the following set of linear differential equations in τ_{11} , τ_{22} and τ_{12} may be written:

$$\tau_{11} + \lambda_1 \left[\dot{\tau}_{11} - (\dot{\gamma} + \epsilon\dot{\phi}(t))\tau_{21}(1+a) \right] = 0 \quad (4.33)$$

$$\tau_{12} + \lambda_1 \dot{\tau}_{12} + \frac{\lambda_1}{2} (\dot{\gamma} + \epsilon\dot{\phi}(t)) [(1-a)\tau_{11} - (1+a)\tau_{22}] = \eta_0 (\dot{\gamma} + \epsilon\dot{\phi}(t)) \quad (4.34)$$

$$\tau_{22} + \lambda_1 \left[\dot{\tau}_{22} + (\dot{\gamma} + \epsilon\dot{\phi}(t))\tau_{21}(1-a) \right] = 0 \quad (4.35)$$

Further, the following equations are derived from Eqn 4.33 and Eqn 4.35,

$$\tau_{22} = - \left(\frac{1-a}{1+a} \right) \tau_{11} \quad (4.36)$$

which allows us to write the following pair of linear differential equations:

$$\tau_{11} + \lambda_1 \dot{\tau}_{11} - \lambda_1 \dot{\gamma} (1+a)\tau_{21} - \epsilon \lambda_1 \dot{\phi}(t) \tau_{21} (1+a) = 0 \quad (4.37)$$

$$\tau_{12} + \lambda_1 \dot{\tau}_{12} + \lambda_1 (1-a) \dot{\gamma} \tau_{11} + \epsilon \lambda_1 (1-a) \dot{\phi}(t) \tau_{11} = \eta_0 \dot{\gamma} + \epsilon \eta_0 \dot{\phi}(t) \quad (4.38)$$

Considering the viscometric case, i.e. $\epsilon = 0$, Eqn 4.37 and Eqn 4.38 reduce to:

$$\tau_{11} - \lambda_1 \dot{\gamma} (1+a)\tau_{21} = 0 \quad (4.39)$$

$$\tau_{12} + \lambda_1 (1-a) \dot{\gamma} \tau_{11} = \eta_0 \dot{\gamma} \quad (4.40)$$

From which the expressions for τ_{11} and τ_{12} can be written as:

$$\tau_{11}^{(0)} = \frac{\eta_0 \lambda_1 \dot{\gamma}^2 (1+a)}{1 + \lambda_1^2 \dot{\gamma}^2 (1-a^2)} \quad (4.41)$$

and

$$\tau_{12}^{(0)} = \frac{\eta_0 \dot{\gamma}}{1 + \lambda_1^2 \dot{\gamma}^2 (1-a^2)} \quad (4.42)$$

which, for $a = 0$ reduce the expressions for the Corotational Maxwell model as expected. $\tau_{11}^{(0)}$ and $\tau_{12}^{(0)}$ are viscometric expressions for a 1 dimensional flow whose derivatives return to zero.

Representing the extra stress tensor as a power series:

$$\boldsymbol{\tau} = \boldsymbol{\tau}^{(0)}(t) + \epsilon \boldsymbol{\tau}^{(1)}(t) + \epsilon^2 \boldsymbol{\tau}^{(2)}(t) + \dots \quad (4.43)$$

and substituting into Eqn 4.37 and Eqn 4.38:

$$[\tau_{11}^{(0)} + \epsilon \tau_{11}^{(1)}] + \lambda_1 [\dot{\tau}_{11}^{(0)} + \epsilon \dot{\tau}_{11}^{(1)}] - \lambda_1 \dot{\gamma} (1+a) [\tau_{12}^{(0)} + \epsilon \tau_{12}^{(1)}] - \epsilon \lambda_1 \dot{\phi}(t) [\tau_{12}^{(0)} + \epsilon \tau_{12}^{(1)}] (1+a) = 0 \quad (4.44)$$

$$\begin{aligned} [\tau_{12}^{(0)} + \epsilon \tau_{12}^{(1)}] + \lambda_1 [\dot{\tau}_{12}^{(0)} + \epsilon \dot{\tau}_{12}^{(1)}] + \lambda_1 (1-a) \dot{\gamma} [\tau_{11}^{(0)} + \epsilon \tau_{11}^{(1)}] \\ + \epsilon \lambda_1 (1-a) \dot{\phi}(t) [\tau_{11}^{(0)} + \epsilon \tau_{11}^{(1)}] = \eta_0 \dot{\gamma} + \epsilon \eta_0 \dot{\phi}(t) \end{aligned} \quad (4.45)$$

Noting that $\dot{\tau}_{11}^{(0)} = \dot{\tau}_{12}^{(0)} = 0$ and substituting Eqn 4.41 and Eqn 4.42 for $\tau_{11}^{(0)}$ and $\tau_{12}^{(0)}$, to first order in ϵ :

$$\tau_{11}^{(1)} + \lambda_1 \dot{\tau}_{11}^{(1)} - \lambda_1 \dot{\gamma} (1+a) \tau_{12}^{(1)} = \alpha \dot{\phi}(t) \quad (4.46)$$

$$\tau_{12}^{(1)} + \lambda_1 \dot{\tau}_{12}^{(1)} + \lambda \dot{\gamma} (1-a) \tau_{11}^{(1)} = \beta \dot{\phi}(t) \quad (4.47)$$

where

$$\alpha = \frac{\eta_0 \lambda_1 \dot{\gamma} (1 + a)}{1 + \lambda_1^2 \dot{\gamma}^2 (1 - a^2)} \quad (4.48)$$

$$\beta = \frac{\eta_0}{1 + \lambda_1^2 \dot{\gamma}^2 (1 - a^2)} \quad (4.49)$$

For a parallel superposition experiment with a single tone sinusoidal perturbation (i.e. a standard PSR experiment), the first order shear stress may be written in the form:

$$\tau_{12}^{(1)}(t) = G_{\parallel}^*(\dot{\gamma}, \omega) e^{i\omega t} \quad (4.50)$$

where $G_{\parallel}^*(\dot{\gamma}, \omega)$ denotes the usual rate-dependent parallel superposition complex modulus. Writing $\phi(t) = e^{i\omega t}$ in Eqn 4.46 and Eqn 4.47, it is also clear that $\tau_{11}^{(1)}$ will take the form:

$$\tau_{11}^{(1)}(t) = A(\dot{\gamma}, \omega) e^{i\omega t} \quad (4.51)$$

Eqn 4.46 and Eqn 4.47 can be written as:

$$A(\dot{\gamma}, \omega)(1 + \lambda_1 i\omega) - \lambda_1 \dot{\gamma} (1 + a) G_{\parallel}^*(\dot{\gamma}, \omega) = \alpha i\omega \quad (4.52)$$

$$G_{\parallel}^*(\dot{\gamma}, \omega)(1 + \lambda_1 i\omega) + \lambda_1 \dot{\gamma} (1 - a) A(\dot{\gamma}, \omega) = \beta i\omega \quad (4.53)$$

Solving for $G_{\parallel}^*(\dot{\gamma}, \omega)$:

$$G_{\parallel}^*(\dot{\gamma}, \omega) = \frac{\eta_0 i\omega}{1 + \lambda_1^2 \dot{\gamma}^2 (1 - a^2)} \left[\frac{(1 + \lambda_1 i\omega) - \lambda_1^2 \dot{\gamma}^2 (1 - a^2)}{(1 + \lambda_1 i\omega)^2 + \lambda_1^2 \dot{\gamma}^2 (1 - a^2)} \right] \quad (4.54)$$

which reduces to (i) the expressions for the Corotational Maxwell model when $a = 0$ and (ii) the linear viscoelastic modulus when $\dot{\gamma} = 0$.

Resolving Eqn 4.54 into its real and imaginary parts, expressions for the parallel storage and loss moduli, respectively, can be obtained.

$$G'_{\parallel}(\dot{\gamma}, \omega) = \frac{\eta_0 \omega^2 \lambda_1 (1 + \omega^2 \lambda_1^2 - 3\lambda_1^2 \dot{\gamma}^2 (1 - a^2))}{(1 + \lambda_1^2 \dot{\gamma}^2 (1 - a^2))[(1 + \lambda_1^2 \dot{\gamma}^2 (1 - a^2) - \omega^2 \lambda_1^2)^2 + 4\omega^2 \lambda_1^2]} \quad (4.55)$$

$$G''_{\parallel}(\dot{\gamma}, \omega) = \frac{\eta_0 \omega (1 + \omega^2 \lambda_1^2 - \lambda_1^2 \dot{\gamma}^2 (1 - a^2))}{(1 + \lambda_1^2 \dot{\gamma}^2 (1 - a^2) - \omega^2 \lambda_1^2)^2 + 4\omega^2 \lambda_1^2} \quad (4.56)$$

It is interesting to consider the conditions for which negative value of the parallel moduli may appear. Noting that $\lambda_1 > 0$, $\omega > 0$ and $-1 \leq a \leq 1$, the following observations can be made:

1. The condition for $G''_{\parallel}(\dot{\gamma}, \omega)$ to be globally positive (i.e. $G''_{\parallel}(\dot{\gamma}, \omega) > 0$ for all positive ω) is that

$$\lambda_1^2 \dot{\gamma}^2 (1 - a^2) < \frac{1}{3}.$$

From the equation above, it is possible to obtain a frequency independent, critical shear rate that identifies the transition boundary from positive to negative values of G''_{\parallel} . This critical shear rate can be obtained as:

$$\lambda_1^2 \dot{\gamma}^2 (1 - a^2) = \frac{1}{3}.$$

$$\dot{\gamma} = \sqrt{\frac{1}{3(1-a^2)\lambda_1^2}}.$$

This critical shear rate is observed as vertical lines in Fig 4.4 calculated with different values of the non-affine parameter (a). As the non-affine parameter is increased, this boundary appears at higher shear rates. In region located on the left side of the line, all values of parallel storage moduli are positive. In the region located on the right side, parallel storage moduli is negative, $G''_{\parallel}(\dot{\gamma}, \omega) < 0$, where

$$\omega^2 \lambda_1^2 < 3\lambda_1^2 \dot{\gamma}^2 (1 - a^2) - 1.$$

From the equation above, it is possible to obtain a shear rate dependent, critical frequency at which the transition from positive values to negative values of G''_{\parallel} occurs. This critical frequency can be obtained as:

$$\omega^2 \lambda_1^2 = 3\lambda_1^2 \dot{\gamma}^2 (1 - a^2) - 1.$$

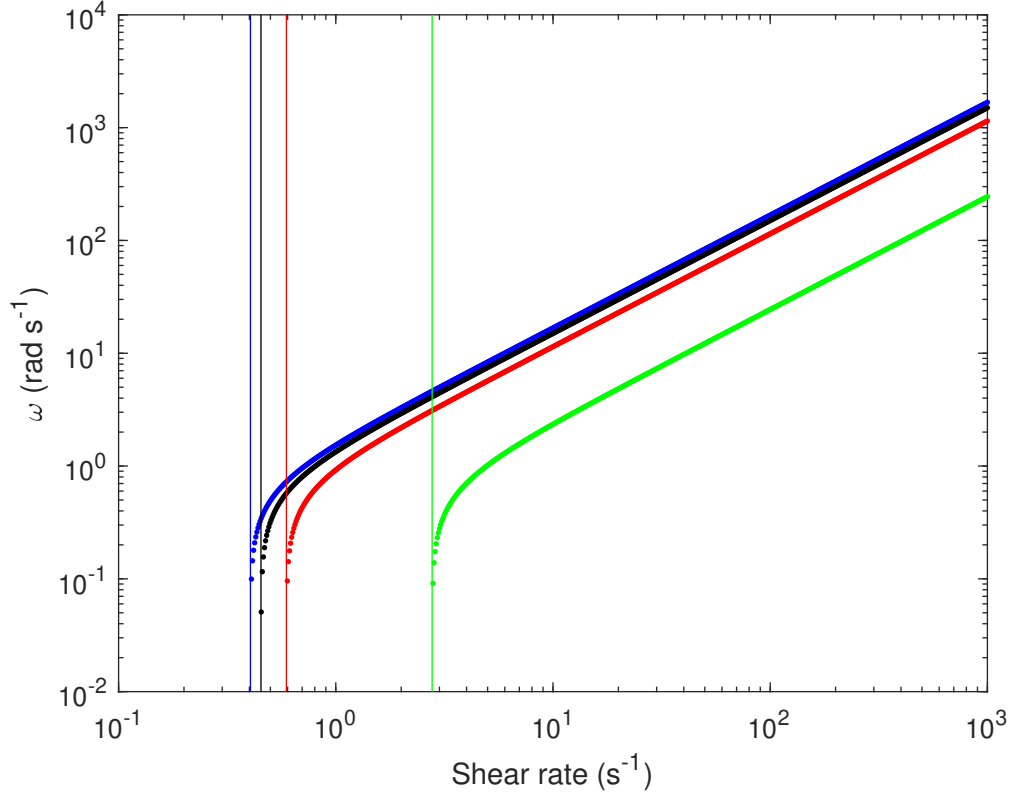


Figure 4.4: Critical frequency against shear rate with different values of the non-affine parameter (a). $a = 0.25$ (blue), 0.5 (black), 0.75 (red), 0.99 (green) and $\lambda_1 = 1.4739$ s.

$$\omega = \sqrt{3\dot{\gamma}^2(1 - a^2) - \frac{1}{\lambda_1^2}}$$

The critical frequency, where $G''_{\parallel} = 0$, for different values of the non-affine parameter (a) is shown in Fig 4.4. As shear rate increases, the critical frequency shifts to higher frequencies i.e. negative values of parallel storage moduli can be found at higher frequencies if the superimposed shear rate is increased as well.

2. The condition for $G''_{\parallel}(\dot{\gamma}, \omega)$ to be globally positive (where $\eta_s = 0$) is that

$$\lambda_1^2 \dot{\gamma}^2 (1 - a^2) < 1.$$

Otherwise, $G_{\parallel}''(\dot{\gamma}, \omega) < 0$ where

$$\omega^2 \lambda_1^2 < \lambda_1^2 \dot{\gamma}^2 (1 - a^2) - 1.$$

Hence, as observed experimentally [23], for a given frequency, $G_{\parallel}'(\dot{\gamma}, \omega)$ will become negative at lower $\dot{\gamma}$ than $G_{\parallel}''(\dot{\gamma}, \omega)$.

Kramers-Krönig (KK) Compliance

Yamamoto's work [95] in which he derived expressions for $G_{\parallel}'(\dot{\gamma}, \omega)$ and $G_{\parallel}''(\dot{\gamma}, \omega)$ for a Lodge-type integral constitutive equation (“Lodge-type” because Yamamoto allowed the memory function of the Lodge model to become shear rate dependent) has been used to justify claims that the parallel superposition moduli do not satisfy the Kramers-Krönig relations. Curtis & Davies [25] showed that the expressions could be rewritten as a pair of Kramers-Krönig compliant moduli. Since then, the K-BKZ and Wagner I models [24], and the CRM model [23] have also been shown to have Kramers-Krönig compliant parallel moduli. The parallel moduli for the GS model (Eqn 4.55 & Eqn 4.56) also satisfy the Kramers-Krönig relations since $G_{\parallel}^*(\dot{\gamma}, \omega)$, apart from at its poles, is an analytic function of ω throughout the complex frequency plane.

Orthogonal Superposition for the Gordon-Schowalter model

For orthogonal superposition experiments, in which the flow field is defined by Eqn 4.24, expansion of the extra stress tensor around the viscometric case leads to a set of six linear simultaneous differential equations. Of these, the τ_{13} and τ_{23} components define a solvable pair from which the orthogonal moduli can be determined:

$$\tau_{13}^{(1)} + \lambda_1 \dot{\tau}_{13}^{(1)} - \frac{1}{2} \lambda_1 \dot{\gamma} (1 + a) \tau_{23}^{(1)} = \frac{1}{2} \alpha \dot{\phi} \quad (4.57)$$

$$\tau_{23}^{(1)} + \lambda_1 \dot{\tau}_{23}^{(1)} + \frac{\lambda_1}{2} \dot{\gamma} (1 - a) \tau_{13}^{(1)} = \frac{1}{2} (\beta + \eta_0) \dot{\phi} \quad (4.58)$$

For an orthogonal superposition experiment with a single tone sinusoidal perturbation, the first order orthogonal shear stress (τ_{23}) can be written:

$$\tau_{23}^{(1)}(t) = G_{\perp}^*(\dot{\gamma}, \omega)e^{i\omega t} \quad (4.59)$$

where $G_{\perp}^*(\dot{\gamma}, \omega)$ denotes the usual rate-dependent orthogonal superposition complex modulus. Writing $\phi(t) = e^{i\omega t}$ in Eqn 4.57 and Eqn 4.58, it is also clear that $\tau_{13}^{(1)}$ will take the form:

$$\tau_{13}^{(1)}(t) = B(\dot{\gamma}, \omega)e^{i\omega t} \quad (4.60)$$

Hence, Eqn 4.57 and Eqn 4.58 can be written as:

$$B(\dot{\gamma}, \omega) + \lambda_1 i \omega B(\dot{\gamma}, \omega) - \frac{1}{2} \lambda_1 \dot{\gamma} (1 + a) G_{\perp}^*(\dot{\gamma}, \omega) = \frac{1}{2} \alpha i \omega \quad (4.61)$$

$$G_{\perp}^*(\dot{\gamma}, \omega) + \lambda_1 i \omega G_{\perp}^*(\dot{\gamma}, \omega) + \frac{\lambda_1}{2} \dot{\gamma} (1 - a) B(\dot{\gamma}, \omega) = \frac{1}{2} (\beta + \eta_0) i \omega \quad (4.62)$$

Solving for $G_{\perp}^*(\dot{\gamma}, \omega)$:

$$G_{\perp}^*(\dot{\gamma}, \omega) = \frac{\eta_0 i \omega}{1 + \lambda_1^2 \dot{\gamma}^2 (1 - a^2)} \left[\frac{(1 + i \omega \lambda_1) + \frac{1}{4} \lambda_1^2 \dot{\gamma}^2 (1 - a^2) (1 + 2i \omega \lambda_1)}{(1 + i \omega \lambda_1)^2 + \frac{1}{4} \lambda_2 \dot{\gamma}^2 (1 - a^2)} \right] \quad (4.63)$$

which can be resolved into its real and imaginary parts to find $G'_{\perp}(\dot{\gamma}, \omega)$ and $G''_{\perp}(\dot{\gamma}, \omega)$, respectively:

$$G'_{\perp}(\dot{\gamma}, \omega) = \frac{\eta_0 \omega^2 \lambda_1}{1 + \lambda_1^2 \dot{\gamma}^2 (1 - a^2)} \times \left[\frac{(1 + \frac{1}{2} \lambda_1^2 \dot{\gamma}^2 (1 - a^2)) \omega^2 \lambda_1^2 + (1 + \frac{1}{4} \lambda_1^2 \dot{\gamma}^2 (1 - a^2)) (1 - \frac{1}{2} \lambda_1^2 \dot{\gamma}^2 (1 - a^2))}{(1 + \frac{1}{4} \lambda_1^2 \dot{\gamma}^2 (1 - a^2) - \omega^2 \lambda_1^2)^2 + 4 \omega^2 \lambda_1^2} \right] \quad (4.64)$$

$$G''_{\perp}(\dot{\gamma}, \omega) = \frac{\eta_0 \omega}{1 + \lambda_1^2 \dot{\gamma}^2 (1 - a^2)} \left[\frac{(1 + \frac{1}{4} \lambda_1^2 \dot{\gamma}^2 (1 - a^2))^2 + \omega^2 \lambda_1^2 (1 + \frac{3}{4} \lambda_1^2 \dot{\gamma}^2 (1 - a^2))}{(1 + \frac{1}{4} \lambda_1^2 \dot{\gamma}^2 (1 - a^2) - \omega^2 \lambda_1^2)^2 + 4 \omega^2 \lambda_1^2} \right] \quad (4.65)$$

It is again interesting to note the conditions for which negative values of the moduli may appear. Noting that $\lambda_1 > 0$, $\omega > 0$ and $-1 \leq a \leq 1$ we see that:

1. The condition for $G'_\perp(\dot{\gamma}, \omega)$ to be globally positive (i.e. $G'_\perp(\dot{\gamma}, \omega) > 0$ for all positive ω) is that

$$\lambda_1^2 \dot{\gamma}^2 (1 - a^2) < 2$$

Otherwise, $G'_\perp(\dot{\gamma}, \omega) < 0$ where

$$\omega^2 \lambda_1^2 < \frac{(1 + \frac{1}{4} \lambda_1^2 \dot{\gamma}^2 (1 - a^2))(2 - \lambda_1^2 \dot{\gamma}^2 (1 - a^2))}{2 + \lambda_1^2 \dot{\gamma}^2 (1 - a^2)}$$

2. $G''_\perp(\dot{\gamma}, \omega)$ is always globally positive

The Upper Convected Maxwell fluid

In the limit of $a = 1$, the GS model reduces to that of Upper Convected Maxwell (UCM) fluid. In this limit, the expressions for the superposition moduli are:

$$G'_{\parallel}(\dot{\gamma}, \omega) = G'_{\perp}(\dot{\gamma}, \omega) = G'(\dot{\gamma}, \omega) = \frac{\eta_0 \lambda_1 \omega^2}{1 + \omega^2 \lambda_1^2} \quad (4.66)$$

$$G''_{\parallel}(\dot{\gamma}, \omega) = G''_{\perp}(\dot{\gamma}, \omega) = G''(\dot{\gamma}, \omega) = \frac{\eta_0 \omega}{1 + \omega^2 \lambda_1^2} \quad (4.67)$$

In the UCM model, the parallel and orthogonal moduli reduce to the linear moduli meaning that the shear rate dependency that can lead to negative values of the superposition moduli is lost. This result is unsurprising since the UCM model does not display shear thinning in the viscometric case.

4.2 Experimental Methods

Materials

Cetylpyridinium chloride (*CPyCl*) and sodium salicylate (*NaSal*) (Sigma-Aldrich) were dissolved at a molar ratio of 2:1 in 0.5 M sodium chloride (*NaCl*) solutions prepared using deionized H_2O . Appropriate quantities of dry of *NaCl*, *NaSal* and *CPyCl*, in powdered form, were added to H_2O in a fume hood. The mixtures were stirred for 24 hours at 40°C (in a sealed beaker atop a heated plate) to completely disperse the powder before measurements were performed. All chemicals were used as received without further purification. Two *CPyCl/NaSal* samples were prepared. The first was formulated to contain 5.9 wt% *CPyCl* which has been reported in the literature [17] to display shear banding, herein, this sample is referred to as the shear banding formulation, SB. The second contained 4.1 wt% *CPyCl* which has been reported to display shear thinning characteristics, this is referred to as the shear thinning solution, ST, herein. This procedure has been reported in literature albeit at different temperatures [44][45].

Rheometry

Rheological measurements of the SB and ST samples were performed on a TA Instruments ARES-G2 rheometer adapted to permit orthogonal superposition experiments. The instrument was fitted with a double gap concentric cylinder with inside and outside cup diameters of 27.732 mm and 22.995 mm, respectively, and inside and outside bob diameters of 29.396 mm and 32.08 mm, respectively. The geometry features rectangular windows in the top of the bob and the bottom of the cup, the former allows the free surface of the sample to sit within the window hence minimising surface tension effects during orthogonal experiments. The latter, allows the sample to move freely between the “measurement annulus” and a sample reservoir which sits within the inner cup, in this manner, pumping flows are minimised and a uniform velocity gradient is achieved during orthogonal superposition experiments. The gap at the bottom of the bob was 8 mm. Prior to measurements being performed on the SB and ST samples, geometry end-effect correction factors were calibrated using a 970 mPa.s Newtonian silicone oil

(from Brookfield). Measurements were then performed at 21°C for the SB solution, and 20°C for the ST solution with temperature control being achieved via the TA instruments advanced peltier system. A thin layer of silicon oil was added to the free surface of the sample (positioned in the centre of the bob windows) to prevent solvent evaporation during measurement. The sample was loaded and conditioned (at rest) for 900 *s* at the desired temperature before being pre-sheared at 1 *s*⁻¹ for 60 *s*. The sample was then allowed to rest for a further 60 *s* before rheological measurements were performed.

Rheological characterisation involved (i) determination of the linear viscoelastic range using a strain sweep, (ii) acquisition of frequency sweep data $0.64 \text{ rad s}^{-1} \leq \omega \leq 100 \text{ rad s}^{-1}$ at a strain amplitude within the LVR, (iii) acquisition of a flow sweep which was performed in the reverse direction (100 *s*⁻¹ to 0.1 *s*⁻¹) (iii) identification of the “pseudo linear range” (p-LVR) for parallel superposition measurements using strain sweeps (iv) acquisition of parallel superposition frequency sweep at the strain amplitude within the p-LVR for PSR, (v) identification of the “pseudo linear range” (p-LVR) for orthogonal superposition measurements using orthogonal strain sweeps (for which the strain range is limited by a maximum axial displacement of 50 μm , and (vi) acquisition of orthogonal superposition frequency sweep data at a strain amplitude within the p-LVR for OSR. The results of this analysis are shown in Appendix A.

4.3 Data Processing

Data was processed using two fitting algorithms. The first (procedure A) assumes a weakly nonlinear response in that the underlying linear viscoelastic spectrum is not permitted to be a function of shear rate, the second (procedure B) allows the underlying viscoelastic spectrum to be rate dependent thus permitting strongly-nonlinear behaviour [61].

Data Analysis Procedure A

Analysis procedure A involved simultaneously fitting (i) linear viscoelastic data ($G'(\omega)$, $G''(\omega)$) to a 2 mode Maxwell model with a Newtonian solvent contribution, and viscom-

entry data ($\eta(\dot{\gamma})$) to Eqn 4.42. For the SB sample, the viscosity data in the shear banding region (characterised by a plateau in the shear stress which occurred for $\dot{\gamma} > 4 \text{ s}^{-1}$) was not admitted to the fitting procedure. For WLM systems, it has previously been suggested that the shorter mode characterises the breakup of chains [15]. Further, this break up timescale (λ_{br}) has been observed to be independent of $\dot{\gamma}$ in several studies. This timescale can be determined from the angular frequency at which the dip in $G''(\omega)$ reaches its minimum. Hence, the timescales of the shorter mode were fixed at $\lambda_2 = 0.0176 \text{ s}$ and $\lambda_2 = 0.0442 \text{ s}$ for the ST (Fig 4.5) and SB samples (Fig 4.6), respectively. Further, the solvent viscosity was found to be approximately $\eta_s = 0.03 \text{ Pa.s}$ and $\eta_s = 0.1727 \text{ Pa.s}$ for the ST and SB samples, respectively and this value was also fixed in all subsequent analysis. This procedure involved 4 degrees of freedom ($[\lambda_1, \eta_0, \eta_1, a]$) which were then used to predict the parallel and orthogonal data ($G'_{\parallel}, G''_{\parallel}$ and G'_{\perp}, G''_{\perp} , respectively) for the CRM ($a = 0$) and GS models. The predicted superposition moduli were then compared to the measured superposition moduli to assess the ability of the GS and CRM models to capture the dynamics of the systems.

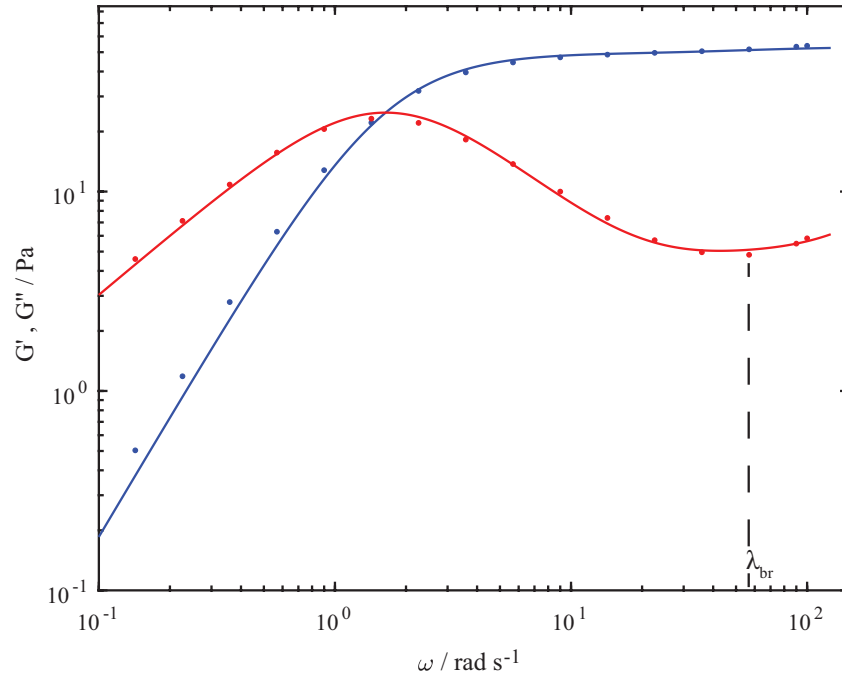


Figure 4.5: The linear viscoelastic moduli of the ST solution showing experimental values (symbols) and calculated values (solid lines) obtained from a two mode Maxwell model with a solvent viscosity. The storage modulus (G') is represented by blue shapes and lines. The loss modulus (G'') is represented by red shapes and lines. The black dashed line represents $\lambda_{br} = 1/G''_{min}$.

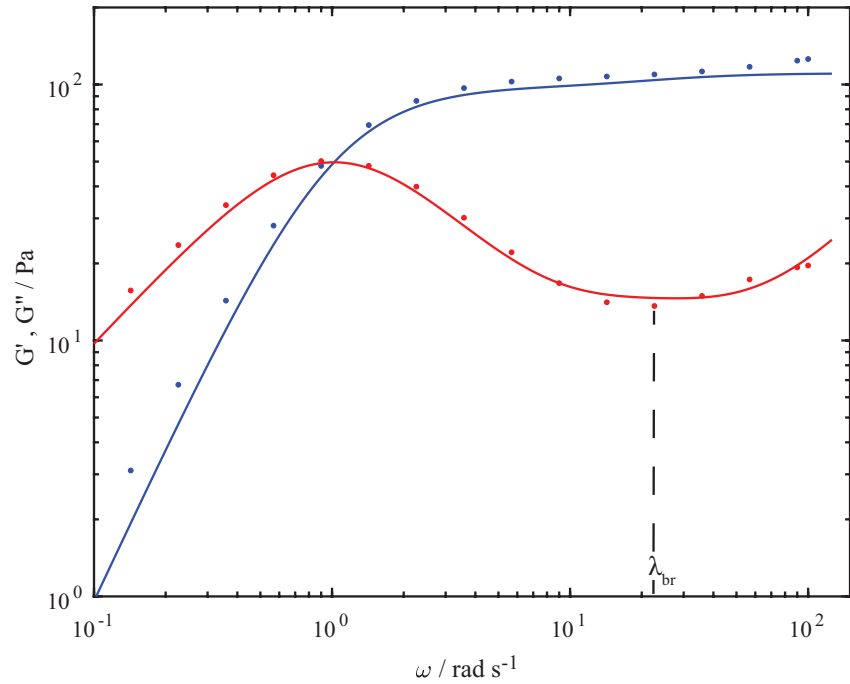


Figure 4.6: The linear viscoelastic moduli of the SB solution showing experimental values (symbols) and calculated values (solid lines) obtained from a two mode Maxwell model with a solvent viscosity. The storage modulus (G') is represented by blue shapes and lines. The loss modulus (G'') is represented by red shapes and lines. The black dashed line represents $\lambda_{br} = 1/G''_{min}$.

Data Analysis Procedure B

Analysis procedure B involved treating the data such that each shear rate defined a discrete and independent material state. Parallel and orthogonal moduli were simultaneously fitted at each shear rate. This approach admitted the possibility of shear induced modification of the underlying relaxation spectrum thus allowing strong non-linearity [61]. The solvent viscosity and the relaxation time of the short mode were fixed as per procedure A. In contrast to analysis A, for which 4 degrees of freedom were used in an attempt to fit the entire data set $(\eta, G^*(\omega), G_{\parallel}^*(\omega, \dot{\gamma}), G_{\perp}^*(\omega, \dot{\gamma}))$, analysis B involved 4 degrees of freedom $([\eta_0, \lambda_2, \eta_1, a])$ **at each shear rate** and thus permitted changes in these parameters to be tracked as a function of $\dot{\gamma}$. The Giesekus model showed good performance under analysis A hence, analysis B is not necessary for the model.

4.4 Results & Discussion

Shear Thinning Case: Analysis A & B

Analysis A

For the ST solution modelled with the Giesekus model in Fig 4.7, there is good agreement between experimental and model prediction up to $\dot{\gamma} = 1 \text{ s}^{-1}$ with discrepancies appearing at 4 s^{-1} & 10 s^{-1} (It is important to note that models have been plotted as the absolute values of G'_{\parallel} and that there is no singularity within the frequency range). It should be noted that the Giesekus model was originally intended to model the nonlinear rheological behaviour of polymers in solutions but was later found to have a wide range of applications especially for WLMs [54].

For the ST solution in Fig 4.8, the CRM model can predict WLM dynamics for $\dot{\gamma} < 1 \text{ s}^{-1}$ for parallel flows and orthogonal flows. At $\dot{\gamma} = 1 \text{ s}^{-1}$, the model correctly predicts flow behaviour at $\omega > 2 \text{ rad s}^{-1}$ under parallel conditions but succeeds in modelling flows under orthogonal conditions. At $\dot{\gamma} = 4 \text{ s}^{-1}$ & $\dot{\gamma} = 10 \text{ s}^{-1}$, the model does not capture the dynamics for PSR and OSR flows.

Whilst the CRM is known to excessively shear thin, GS model moderates the excessive shear thinning by using the slip parameter (a). The GS model predicts a non-monotonic flow curve which is a characteristic of shear banding systems. For the ST solution in Fig 4.9, the GS model shows good predictions for WLM dynamics for both parallel and orthogonal flows for $\dot{\gamma} = 0.1 \text{ s}^{-1}$, $\dot{\gamma} = 0.4 \text{ s}^{-1}$ & $\dot{\gamma} = 1 \text{ s}^{-1}$. In the high shear rate region of $\dot{\gamma} = 4 \text{ s}^{-1}$ & $\dot{\gamma} = 10 \text{ s}^{-1}$, the GS model cannot capture WLM dynamics for both parallel and orthogonal flows.

Analysis B

In Data Analysis B, each shear rate was treated as a separate state with parallel superposition and orthogonal superposition data being fitted simultaneously at each shear rate but independent of data at other rates. The viscosity at the shear rate of interest was also admitted to the fitting routine via Eqn 4.42 with $a = 0$ for the CRM model and a serves as a free parameter for the GS model. The CRM model for the ST solution in Fig 4.10, shows good performance for $\dot{\gamma} = 0.1 \text{ s}^{-1}$, $\dot{\gamma} = 0.4 \text{ s}^{-1}$ & $\dot{\gamma} = 1 \text{ s}^{-1}$ in PSR and OSR flows. In the high shear rate region of $\dot{\gamma} = 4 \text{ s}^{-1}$ & $\dot{\gamma} = 10 \text{ s}^{-1}$, the CRM model cannot capture WLM dynamics for both parallel and orthogonal flows. The GS model for the ST solution in Fig 4.11 where a is a free parameter can capture WLM dynamics for both parallel and orthogonal flows for all shear rates except $\dot{\gamma} = 10 \text{ s}^{-1}$ where slight discrepancies between experimental and model predictions are observed.

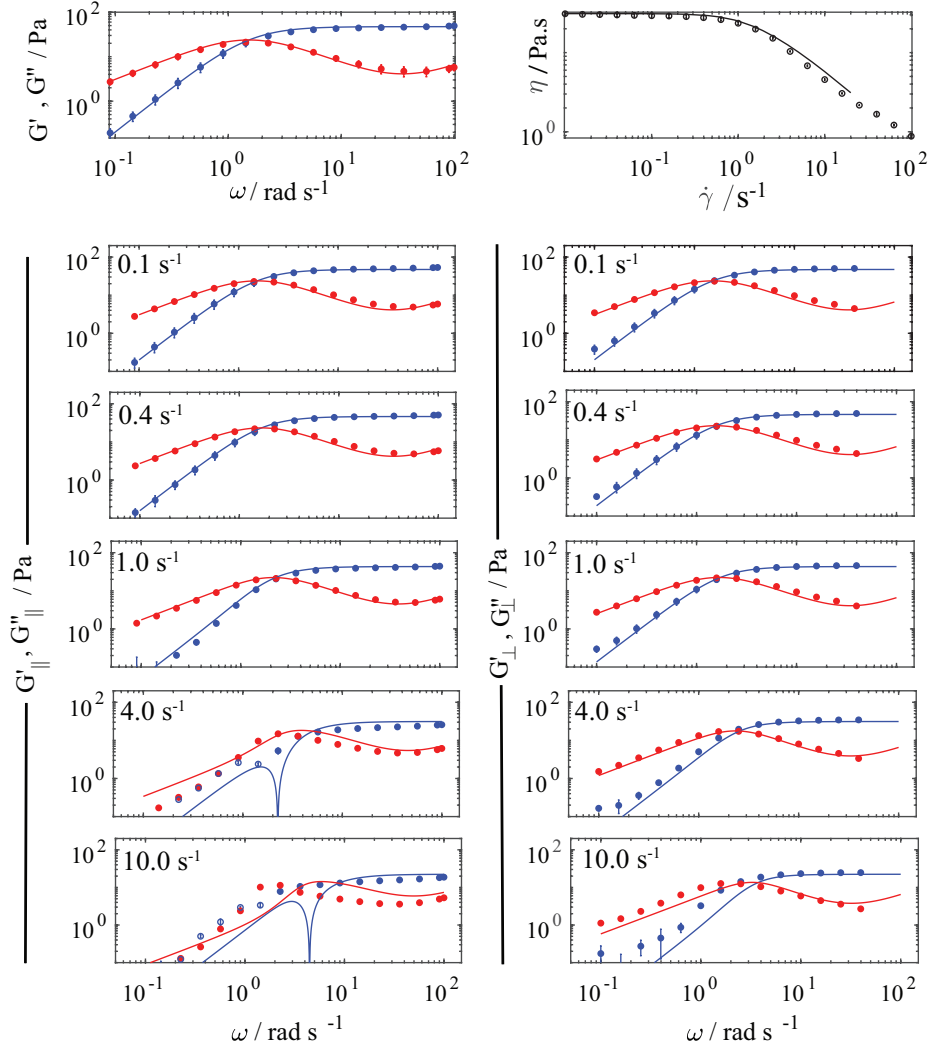


Figure 4.7: Data analysis procedure A for the shear thinning (ST) formulation using the Giesekus (GIE) model. The blue and red circles are experimental G' and G'' , respectively. The solid lines are fits with the GIE model. The open shapes are absolute values of any negative experimental data. Parameters from the SAOS data given as $G = 51.8 \text{ Pa}$, $\lambda = 0.6546 \text{ s}$, $\alpha = 0.3$ & $\eta_s = 0.059 \text{ Pa.s}$ is used to calculate model fits for PSR (Eqn 4.19 & Eqn 4.18(left)) and OSR (Eqn 4.17 & Eqn 4.16 (right)).

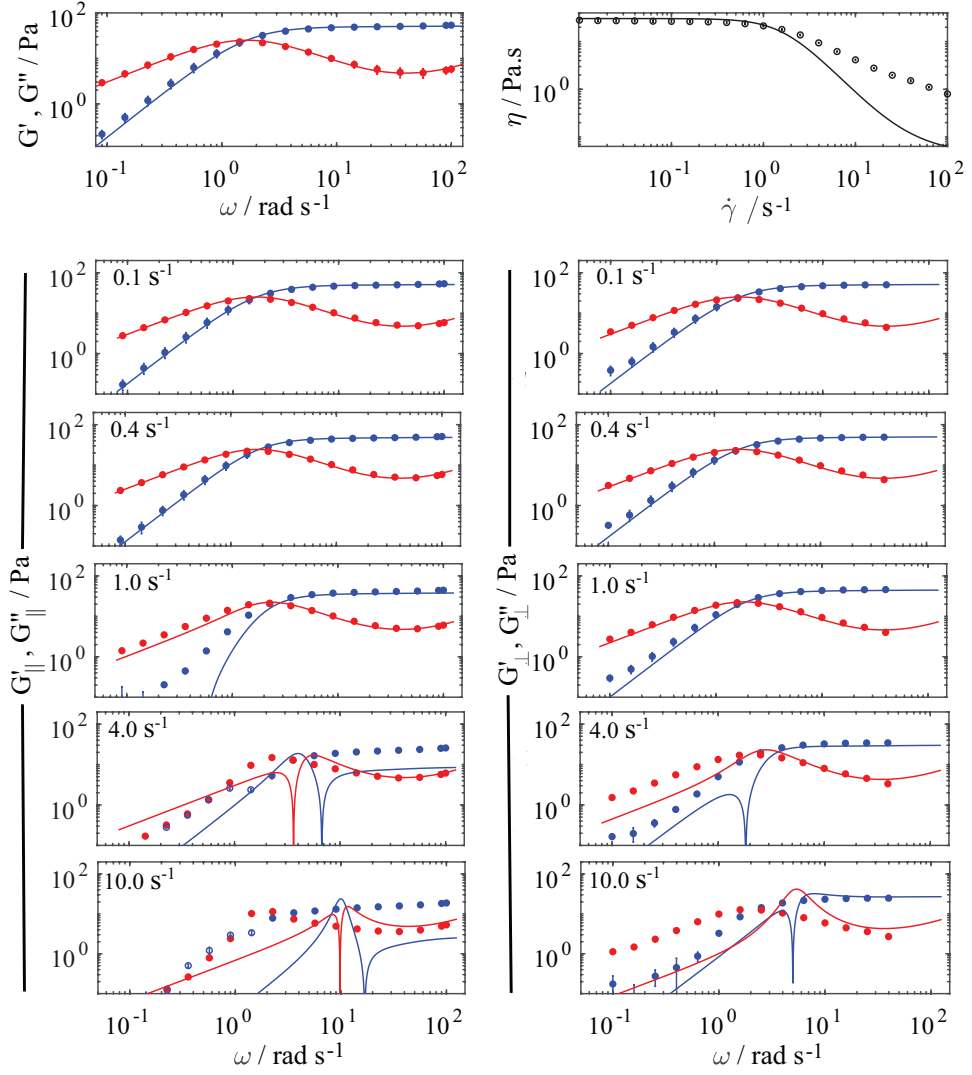


Figure 4.8: Data analysis procedure A for the shear thinning (ST) formulation using the Corotational Maxwell model (CRM). The blue and red circles are experimental G' and G'' , respectively and the solid lines are fits with the CRM model (PSR (Eqn 4.27 & Eqn 4.28), OSR (Eqn 4.29 & Eqn 4.30)). The open shapes are absolute values of any negative experimental data and $a = 0$.

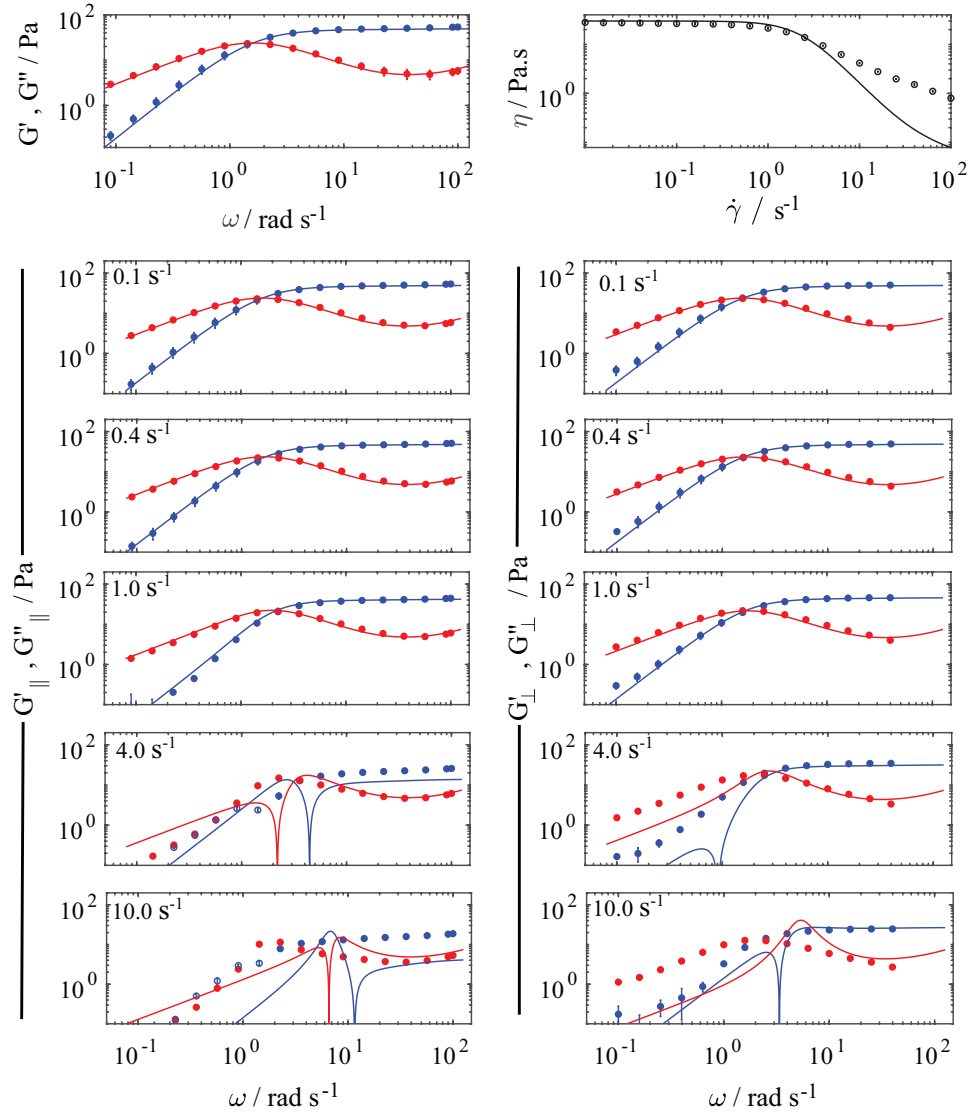


Figure 4.9: Data analysis procedure A for the shear thinning (ST) formulation using the Gordon-Schowalter model (GS). The blue and red circles are experimental G' and G'' , respectively and the solid lines are fits with the GS model (PSR (Eqn 4.55 & Eqn 4.56), OSR (Eqn 4.64 & Eqn 4.65)). The open shapes are absolute values of any negative experimental data.

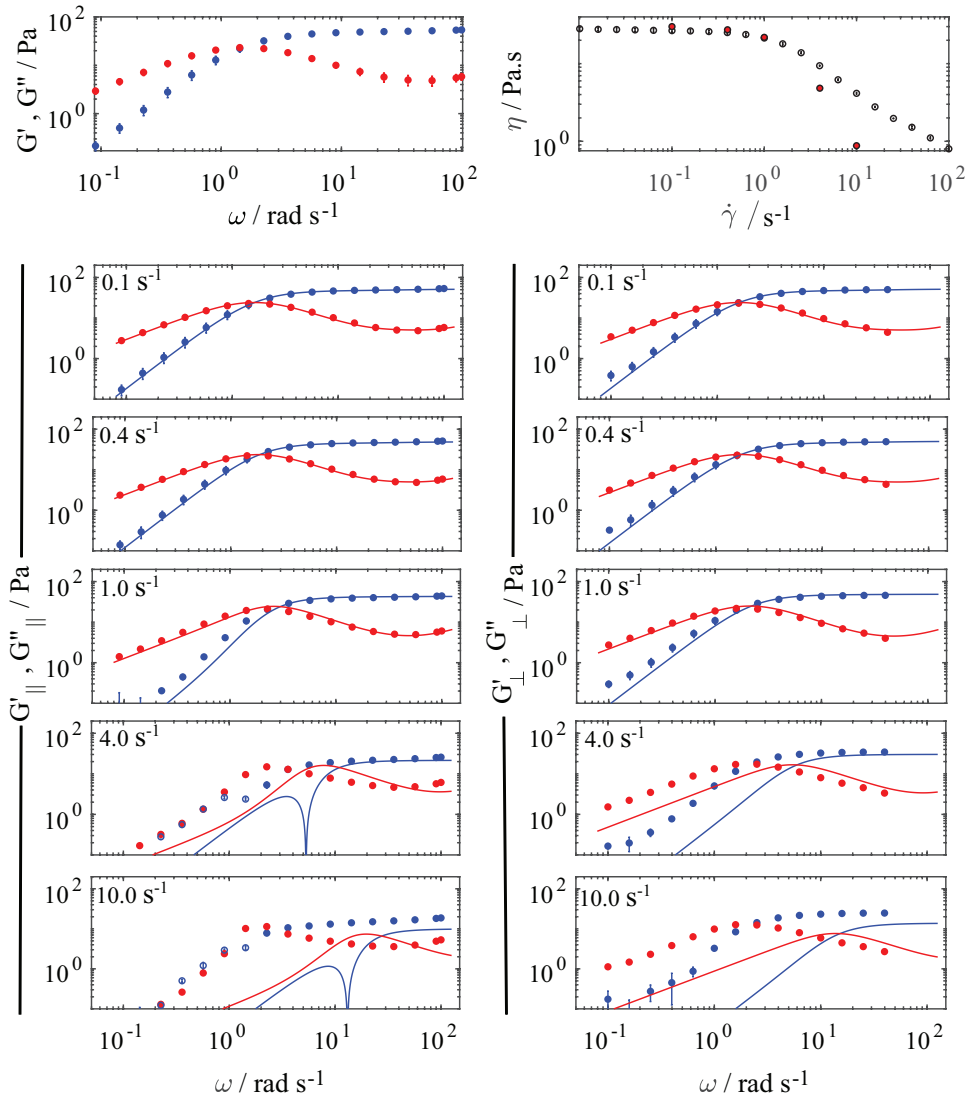


Figure 4.10: Data analysis procedure B for the shear thinning (ST) formulation using the Corotational Maxwell model (CRM). The blue and red circles are experimental G' and G'' , respectively and the solid lines are fits with the CRM model (PSR (Eqn 4.27 & Eqn 4.28), OSR (Eqn 4.29 & Eqn 4.30)). The open shapes are absolute values of any negative experimental data and $a = 0$.

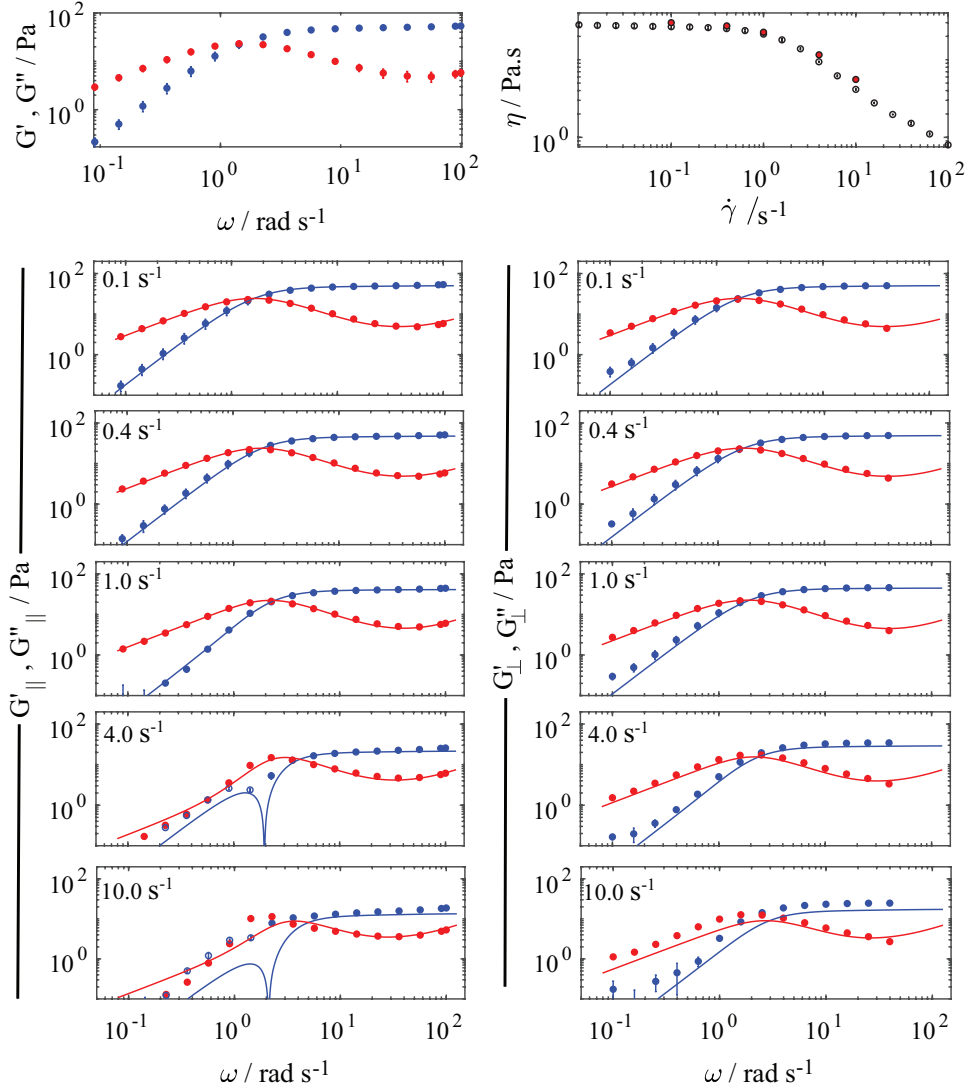


Figure 4.11: Data analysis procedure B for the shear thinning (ST) formulation using the Gordon-Schowalter model (GS). The blue and red circles are experimental G' and G'' , respectively and the solid lines are fits with the GS model (PSR(Eqn 4.55 & Eqn 4.56), OSR(Eqn 4.64 & Eqn 4.65)). The open shapes are absolute values of any negative experimental data.

Shear Banding Case: Analysis A & B

Analysis A

For the SB solution in Fig 4.12 modelled with the GIE model , there is good agreement between model and experimental data up to $\dot{\gamma} = 1 \text{ s}^{-1}$ while discrepancies begin to appear at $\dot{\gamma} = 4 \text{ s}^{-1}$ and $\dot{\gamma} = 10 \text{ s}^{-1}$. The GIE model performs relatively well when describing the dynamics of a shear banding WLM except at high shear rates of 10 s^{-1} . For the SB solution in Fig 4.13, the CRM model can predict WLM dynamics for both parallel and orthogonal flows for $\dot{\gamma} = 0.1 \text{ s}^{-1}$, $\dot{\gamma} = 0.4 \text{ s}^{-1}$ & $\dot{\gamma} = 1 \text{ s}^{-1}$. In the region of shear banding, $\dot{\gamma} = 4 \text{ s}^{-1}$ & $\dot{\gamma} = 10 \text{ s}^{-1}$, the CRM model cannot capture the dynamics under both parallel and orthogonal conditions. The same trends can be observed in the GS model for the SB solution in Fig 4.14.

Analysis B

The CRM model for the SB solution in Fig 4.15, shows good performance for $\dot{\gamma} = 0.1 \text{ s}^{-1}$, $\dot{\gamma} = 0.4 \text{ s}^{-1}$ & $\dot{\gamma} = 1 \text{ s}^{-1}$ in PSR and OSR flows. In the high shear rate region of $\dot{\gamma} = 4 \text{ s}^{-1}$ & $\dot{\gamma} = 10 \text{ s}^{-1}$, the CRM model cannot capture WLM dynamics for both parallel and orthogonal flows. The GS model for the SB solution in Fig 4.16 where a is a free parameter can capture WLM dynamics for both parallel and orthogonal flows for all shear rates except for $\dot{\gamma} = 10 \text{ s}^{-1}$ which is in the shear banding region.

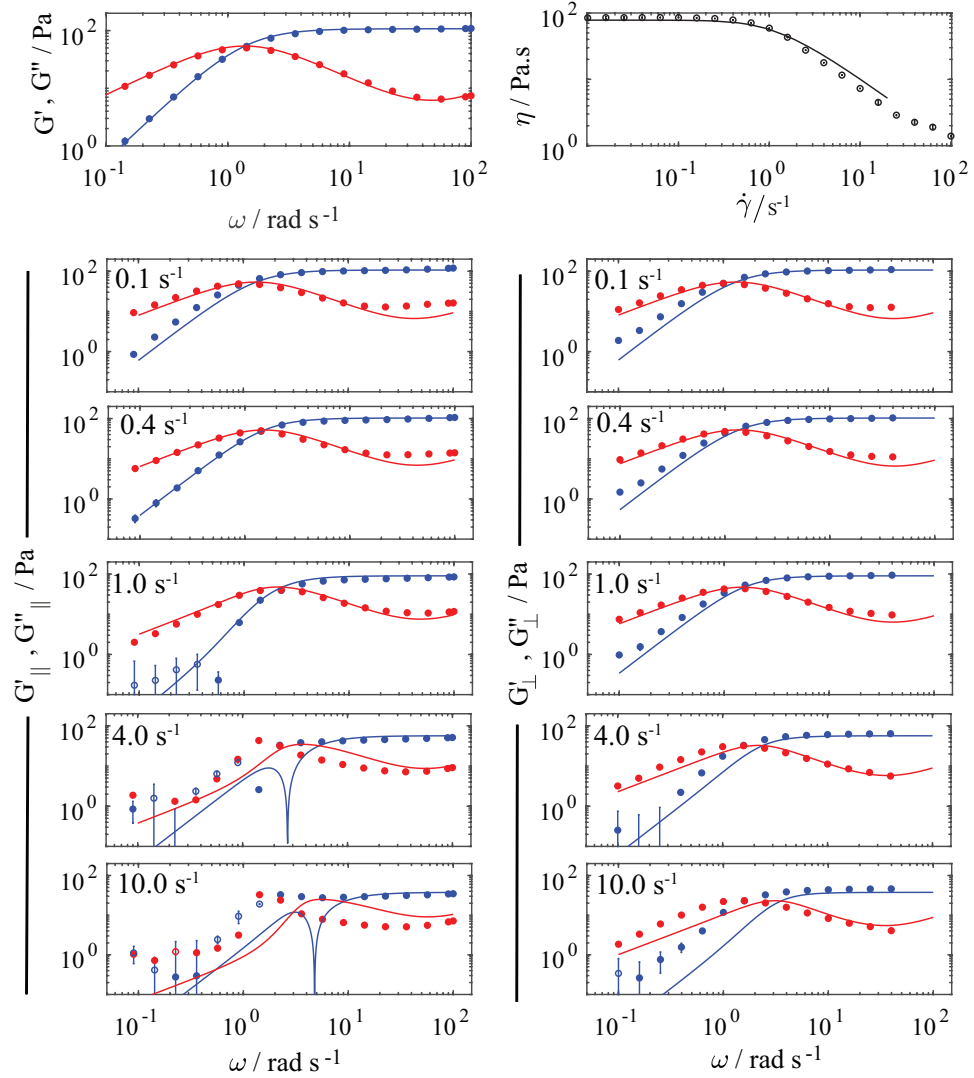


Figure 4.12: Data analysis procedure A for the shear banding (SB) formulation using the Giesekus (GIE) model. The blue and red circles are experimental G' and G'' , respectively. The solid lines are fits with the GIE model. The open shapes are absolute values of any negative experimental data. Parameters from the SAOS data given as $G = 115 \text{ Pa}$, $\lambda = 1.0606 \text{ s}$, $\alpha = 0.5$ & $\eta_s = 0.2793 \text{ Pa.s}$ is used to calculate model fits for PSR(Eqn 4.19 & Eqn 4.18(left)) and OSR(Eqn 4.17 & Eqn 4.16 (right)).

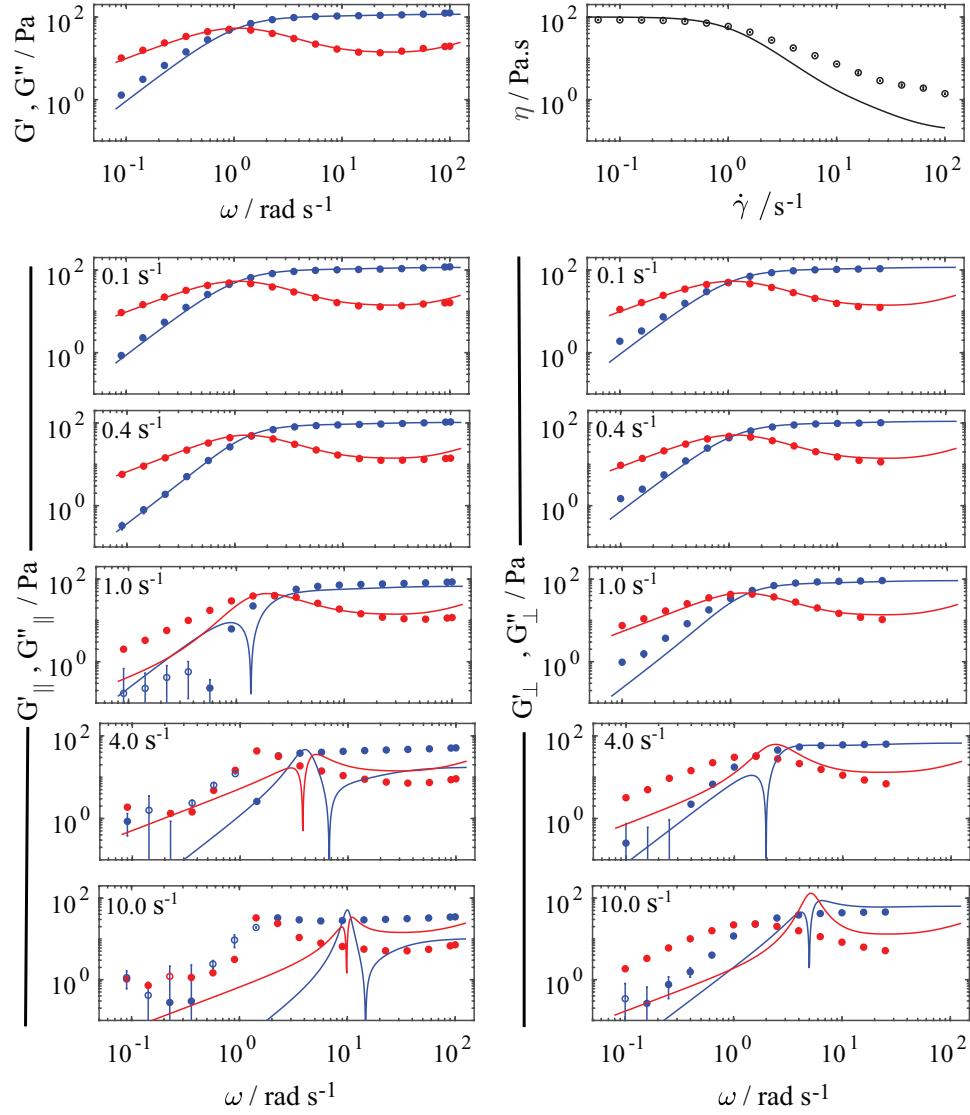


Figure 4.13: Data analysis procedure A for the shear banding (SB) formulation using the Corotational Maxwell model (CRM). The blue and red circles are experimental G' and G'' , respectively and the solid lines are fits with the CRM model (PSR(Eqn 4.27 & Eqn 4.28), OSR(Eqn 4.29 & Eqn 4.30)). The open shapes are absolute values of any negative experimental data and $a = 0$.

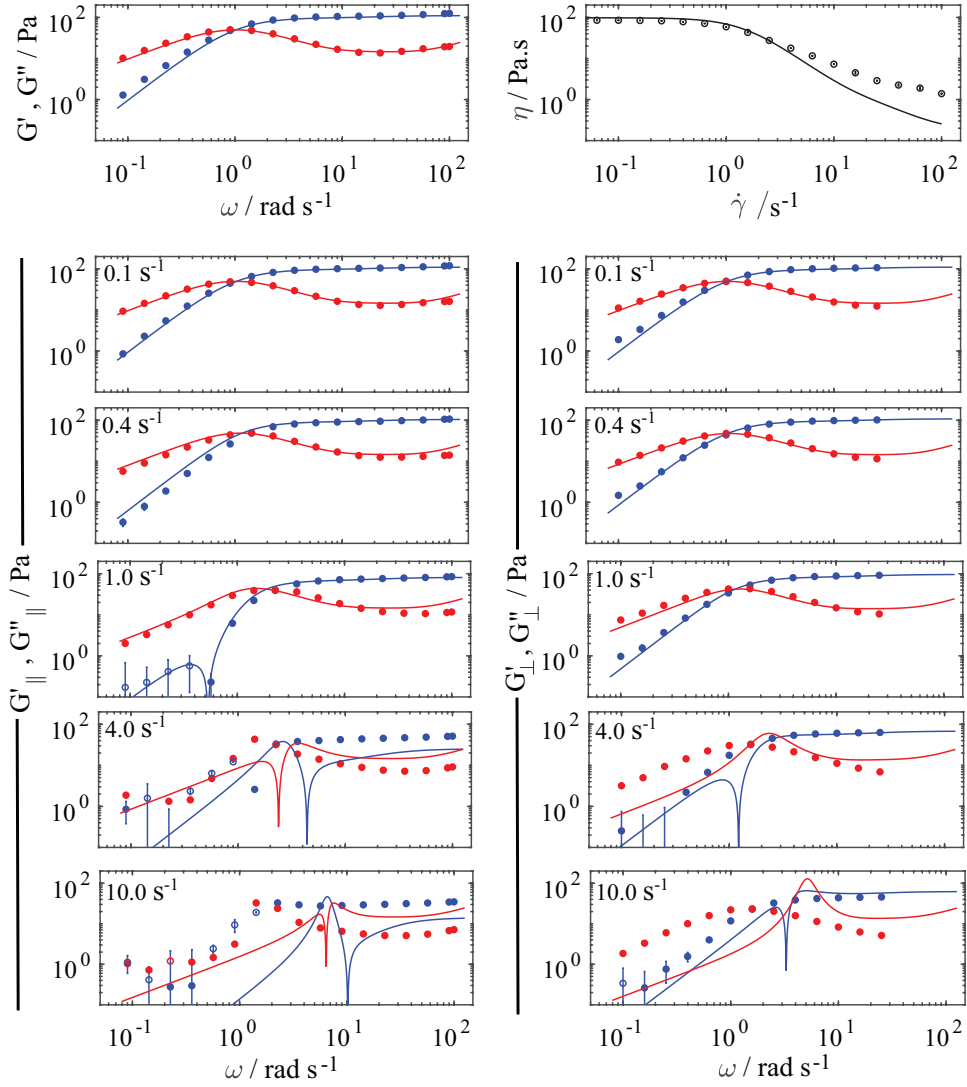


Figure 4.14: Data analysis procedure A for the shear banding (SB) formulation using the Gordon-Schowalter model (GS). The blue and red circles are experimental G' and G'' , respectively and the solid lines are fits with the GS model (PSR(Eqn 4.55 & Eqn 4.56), OSR(Eqn 4.64 & Eqn 4.65)). The open shapes are absolute values of any negative experimental data.

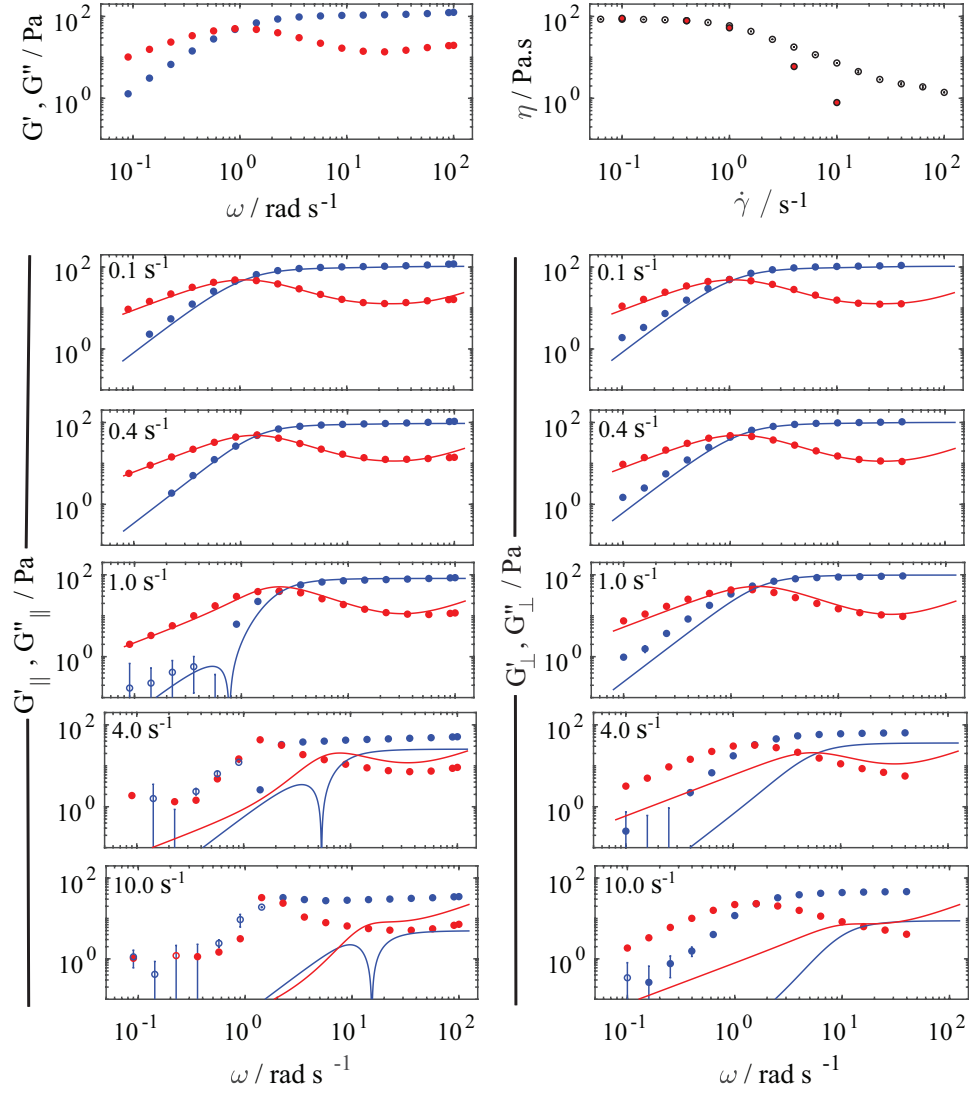


Figure 4.15: Data analysis procedure B for the shear banding (SB) formulation using the Corotational Maxwell model (CRM). The blue and red circles are experimental G' and G'' , respectively and the solid lines are fits with the CRM model (Eqn 4.27, Eqn 4.28, Eqn 4.29 & Eqn 4.30). The open shapes are absolute values of any negative experimental data and $a = 0$.

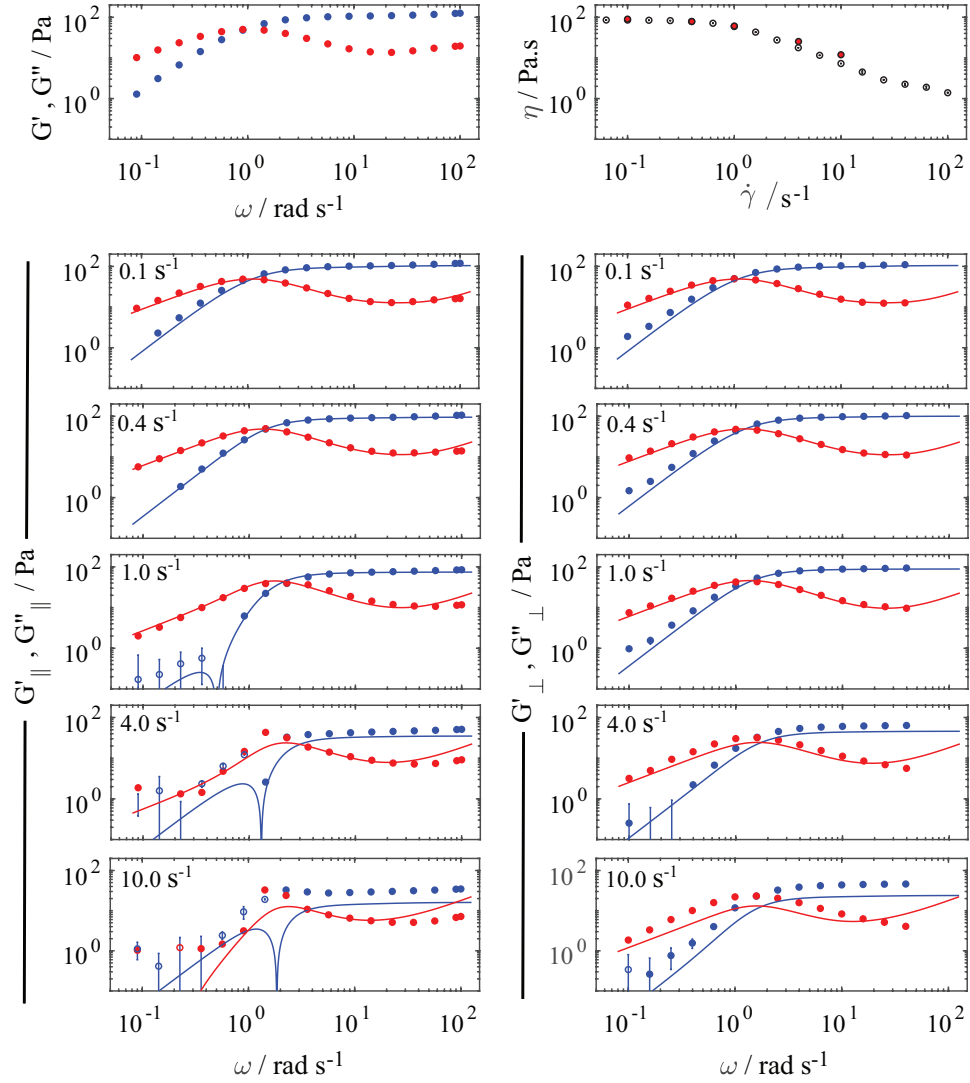


Figure 4.16: Data analysis procedure B for the shear banding (SB) formulation using the Gordon-Schowalter model (GS). The blue and red circles are experimental G' and G'' , respectively and the solid lines are fits with the GS model (PSR(Eqn 4.55 & Eqn 4.56) , OSR(Eqn 4.64 & Eqn 4.65)) . The open shapes are absolute values of any negative experimental data.

In analysis A, the models are fitted to the experimental SAOS data to obtain parameters which are subsequently used to predict experimental data under superimposed flows. For the GIE, CRM and GS models using both ST (Figures 4.7, 4.8 & 4.9 respectively) and SB samples (Figures 4.12, 4.13 & 4.14 respectively), this method shows good results up to $\dot{\gamma} = 1 \text{ s}^{-1}$ because non-linear effects are insignificant at low shear rates (i.e. the microstructural changes caused by superimposing a steady shear insignificant), hence, the SAOS parameters can still characterise the material. For shear rates of $\dot{\gamma} > 1 \text{ s}^{-1}$, substantial nonlinear effects are observed such that parameterisation based on the SAOS data is insufficient. Remarkably, the GIE model can replicate experimental data up to $\dot{\gamma} = 4 \text{ s}^{-1}$ and even shows some agreement (albeit limited) with experimental data at $\dot{\gamma} = 10 \text{ s}^{-1}$ for the ST and SB sample (Figures 4.7 & 4.12 respectively). This is due to the presence of the dimensionless mobility parameter (α) introduced by Giesekus [36] to describe the nonlinear rheological properties of polymer solutions.

In analysis B, the models are fitted individually to each shear rate i.e. each shear rate is assumed to be a different material. The CRM model shows good performance up to $\dot{\gamma} = 1 \text{ s}^{-1}$ for the ST sample (Fig 4.10). The CRM model is known to be excessively shear thinning and lacks the required non-linear parameter to account for non-linear effects hence the model fails at 4 s^{-1} & 10 s^{-1} . The GS model (Fig 4.11) which was introduced to fix the inefficiencies of the CRM model, shows good performance by capturing WLM dynamics at all shear rates for the ST sample. For the SB sample (Fig 4.15), the CRM shows good performance up to $\dot{\gamma} = 1 \text{ s}^{-1}$ beyond which shear banding instabilities cause the model to fail. Interestingly, the GS model (Fig 4.16) shows good performance up to $\dot{\gamma} = 4 \text{ s}^{-1}$ most likely because of its slip parameter that allows non-affine deformation (this non-linearity parameter (a) can model shear banding instabilities up to a point as model failure is observed at $\dot{\gamma} = 10 \text{ s}^{-1}$). The efficiency of a constitutive model is measured by its ability to predict polymer or WLM behaviour under various deformation conditions with as few adjustable parameters as possible. The Giesekus and Gordon-Schowalter models have a single adjustable parameter that encompasses non-linear behaviour [52] which is noticeably absent from the CRM model. It is important to note that the experimental data at low frequencies ($\omega < 2 \text{ rad s}^{-1}$) for high shear rates $\dot{\gamma} > 0.4 \text{ s}^{-1}$ cannot be trusted

due to high noise in those regions as evidenced by the LVR plots in Appendix A.

4.5 Conclusion

The aim of this chapter was to explore the behaviour of WLMs under parallel and orthogonal flows for shear banding and shear thinning WLMs and evaluate the constitutive models that can be used to capture flows under various conditions. The Giesekus model has often been used in literature to model WLM behaviour but rarely under superposition flows and the works in the literature do not differentiate between shear banding and shear thinning WLMs. The Giesekus model performs well at all shear rates (some discrepancies are observed at 10 s^{-1}) for the ST and SB sample. This is due to the presence of the dimensionless mobility parameter (α) that accounts for non-linear behaviour of the system. The CRM model fails to capture chain dynamics at high shear rates ($\dot{\gamma} = 4 \text{ s}^{-1}$ & $\dot{\gamma} = 10 \text{ s}^{-1}$) under analysis A and analysis B because the model is known to excessively shear thin and lacks the single parameter required to account for non-linear behaviour hence the GS model was introduced with a nonlinear slip parameter (a). The GS model was able to capture chain dynamics for both PSR and OSR flows under analysis B for all shear rates for the ST solution but fails to capture the dynamics at $\dot{\gamma} = 10 \text{ s}^{-1}$ for the SB solution because of the presence of shear banding instabilities. In this work, evidence is provided to show that the GS model is better than the CRM model for predicting WLM behaviour under superposition flows especially when analysis B is used. Evidence shows that the GIE model shows good performance under all conditions except at very high shear rates and when shear banding instabilities are present. This procedure can be improved via the introduction of damping functions that modify the parameters of the model as a function of shear rate. This is beyond the scope of this analysis and are recommendations for further work.

Chapter 5

Influence of Inertia on Startup of Stress Controlled Oscillatory Shear

5.1 Introduction

Classical physics defines inertia as “a property of matter by which it remains at rest or in uniform motion in the same straight line unless acted upon by some external force” [70]. In rheometry, stress controlled rheometer (Combined Motor Transducers) are designed such that torque is measured at the moving surface hence the moment of inertia of the moving parts can affect the data accuracy. In essence, oscillatory tests performed using a CMT rheometer involve a periodic acceleration and deceleration of the motor shaft. This means that the total torque output includes the torque required to overcome the instrument inertia and the torque deforming the sample. Hence, instrument inertia often looks like real data and careful analysis is required. For example, Ewoldt [31] identified where instrument inertia can masquerade as real data in the short time experimental data of hagfish gel (Fig 5.1).

According to TA instruments [34], the real and imaginary parts of the measured complex modulus (G^*) are obtained from the measured position ($\Phi_m(t) = \Phi_m^o \cos(\omega t + \delta_m)$) and stress ($M_m(t) = M_m^o \cos(\omega t)$) where δ_m is the raw phase and ω is the frequency. The

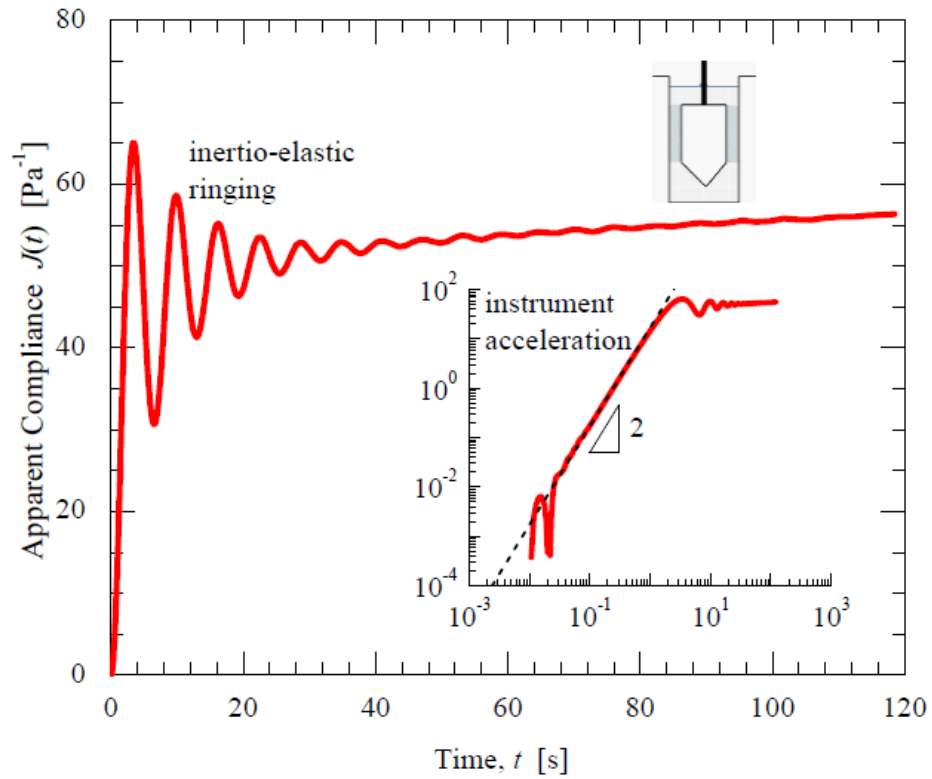


Figure 5.1: Step torque test with hagfish gel in concentric cylinder geometry plotted as apparent compliance. The first 80 seconds of data are caused by a coupling of instrument inertia and elasticity leading to creep ringing effects which are identified by the damped oscillations. This data can be misinterpreted as real material data whereas it is a result of instrument artefacts. Reproduced from Ref [31] permission from Springer New York.

raw phase gives a measure of inertia contributions and instrument inertia can often be detected if the raw phase is greater than 90° because the absence of inertia will always result in a phase angle within the viscoelastic range, $0^\circ < \delta < 90^\circ$. The problem of inertia has been studied widely in different contexts. Methods of accurately determining the motor inertia of a stress-controlled rheometer were proposed by Klemuk et al [56] and commercial rheometers undertake corrections that remove the impact of inertia as part of their data processing routines [12]. For materials that are weakly elastic, there is a coupling of the elasticity and instrument inertia which is called “creep ringing” or “inertio elastic ringing”. These “creep ringing” events are observed as the damped oscillation part which persists for about ≈ 80 s in the angular displacement and measured at the start of a creep test as shown in Fig 5.1 [32]. The Maxwell-Jeffrey’s model is often used to demonstrate creep-ringing in the literature, this model consists of one spring and two dashpots arranged in series or parallel.

One of the major problems caused by inertio elastic ringing is exposed when studying the properties of weak gels, the existence of apparatus inertia and viscoelasticity leads to a coupling frequency which prevents frequency sweep experiments from being carried out at constant shear stress (i.e. the coupling frequency leads to a shear stress sweep). Carson et al [6] has modeled this phenomenon using the Maxwell Jeffrey’s model. Herein, the effect of inertia on the startup of stress controlled oscillatory shear is modelled. It is a common practise to measure the transient response during the startup of shear flow in stress controlled rhoemetry. This transient is dominant at the start of oscillatory flow leading to disorder in the signal and potential measurement errors. Typical methods for analysing small amplitude oscillatory flow involves including a delay until steady time-periodic oscillations have been attained, followed by the use of Fourier transformations to obtain a complex modulus [49]. This method is favoured because Fourier transformations are easy to apply, but result in loss of information on the strain measured from initial configurations. Hassager [41] approached this problem via the general theory of linear viscoelasticity showing that the response to the initiation of stress controlled oscillations contains offset, periodic & transient contributions. This analysis neglects the impact of instrument inertia on the establishment of the steady periodic response. In this work,

inertia contributions are introduced to the framework resulting in both inertio-elastic ringing and an additional phase shift in the periodic part of the response.

5.2 Modelling

Start Up of Oscillatory Shear

In Combined Motor Transducer rheometers (CMT), torque is applied and deformation is recorded by the moving element of the geometry which is undergoing continuous acceleration in oscillatory flows. This means both sample inertia and instrument inertia contribute to the total stress recorded by the instrument. Sample inertia is negligible in the limit of the gap loading [77] hence total stress for a CMT rheometer can be expressed as:

$$\sigma_{total} = \sigma_{sample} + I\ddot{\gamma} \quad (5.1)$$

I is the calibrated system inertia constant and γ is the strain. According to the Boltzmann's superposition principle [62], the convolution of the stress relaxation modulus ($G(t)$) and the deformation history ($\dot{\gamma}$) gives stress (σ). The total inertia effect is calculated as:

$$I = (I_g + I_{ins}) \frac{\sigma_c}{\gamma_c} \quad (5.2)$$

where I_g is the geometry inertia, I_{ins} is the instrument inertia, σ_c is the stress constant and γ_c is the strain constant.

$$\sigma_{sample} = \int_{t'=0}^t G(t-t') \dot{\gamma}(t') dt' \quad (5.3)$$

such that,

$$\sigma_{total} = \int_{t'=0}^t G(t-t') \dot{\gamma} dt' + I\ddot{\gamma} \quad (5.4)$$

Using the following Laplace transformations, Eqn 5.4 can be expressed in Laplace space as:

$$x(s) = \int_{t=0}^{\infty} e^{-st} \sigma_t(t) dt \quad (5.5)$$

$$g(s) = \int_{t=0}^{\infty} e^{-st} G(t) dt \quad (5.6)$$

$$y(s) = \int_{t=0}^{\infty} e^{-st} \gamma(t) dt \quad (5.7)$$

$$\dot{y}(s) = sy(s) \quad (5.8)$$

$$\ddot{y} = s^2 y(s) \quad (5.9)$$

$$y(s) = \frac{1}{s} \frac{x(s)}{(g(s) + Is)} \quad (5.10)$$

Eqn 5.8 and 5.9 are derived with the initial value theorem using initial conditions: $\gamma = 0$ and $\dot{\gamma} = 0$. The absence of inertia ($I = 0$) reduces Eqn 5.10 to equation (7) in Hassager's original work [41].

A sinusoidal applied stress, with an amplitude (σ_0), initiated at time zero is expressed

mathematically as:

$$\sigma_t(s) = \sigma_0 H(t) \sin(\omega t + \psi) \quad (5.11)$$

where $H(t)$ is the heavy-side step function and ψ is the initial phase of the perturbation waveform (for sine perturbations, $\psi = 0$ and cosine perturbations, $\psi = \pi/2$). The following analysis is based on $\psi = 0$. Solving Eqn 5.5 results in:

$$x(s) = \frac{\sigma_0}{s^2 + \omega^2} (\omega \cos \psi + s \sin \psi) \quad (5.12)$$

by substituting Eqn 5.12 into Eqn 5.10, $\gamma(s)$ can be written as:

$$y(s) = \frac{\sigma_0 (\omega \cos \psi + s \sin \psi)}{s(g(s) + Is)(s^2 + \omega^2)} \quad (5.13)$$

The inverse laplace transform of Eqn 5.13 then gives the expression for $\gamma(t)$ after the initiation of the sinusoidal stress. The inverse Laplace transform may be obtained by considering the poles of Eqn 5.13 [82]. The analysis involves 3 components i) the pole at $s = 0$, will give the strain offset ($\gamma_{off}(t)$), ii) the poles at $s = \pm i\omega$ will give the periodic response ($\gamma_p(t)$), iii) the zeroes of the function, $g(s) + Is$ will give the transient component ($\gamma_t(t)$).

Firstly, the contribution to $\gamma(t)$ from the pole at $s = 0$ can be determined by noting that $g(0) = \eta_0$ in conjunction with the final value theorem [82]. The final value theorem states that the value of a function as it goes to infinity in the time domain is equal to the multiplication of s in the Laplace domain with the Laplace transform of the function as s tends to zero.

$$\lim_{t \rightarrow \infty} \gamma(t) = \lim_{s \rightarrow 0} s y(s) \quad (5.14)$$

such that:

$$\gamma_{off}(t) = \frac{\sigma_0 \cos(\psi)}{\eta_0 \omega} \quad (5.15)$$

This is similar to Hassager's inertialess condition confirming that instrument inertia does not affect strain offset. Next, the periodic contribution to the signal ($s = \pm i\omega$) is evaluated with $f(s) = (\omega^2 + s^2)y(s)$ at $s = i\omega$,

$$f(i\omega) = \frac{\sigma_0(\omega \cos \psi) + (i\omega \sin \psi)}{i\omega(g(s) + Ii\omega)} = \frac{\sigma_0\omega(\cos \psi + i \sin \psi)}{i\omega g(i\omega) - I\omega^2} \quad (5.16)$$

The complex modulus [87], $G^*(\omega)$ is:

$$G^*(\omega) = i\omega \int_{t=0}^{\infty} G(t)e^{-i\omega t} dt = i\omega g(i\omega) \quad (5.17)$$

Eqn 5.16 can be re written as:

$$f(i\omega) = \frac{\sigma_0\omega(\cos \psi + i \sin \psi)}{G^*(\omega) - I\omega^2} \quad (5.18)$$

The complex moduli $G^*(\omega)$ can be resolved into its real part $G'(\omega)$ also known as the storage moduli and imaginary part $G''(\omega)$ also known as loss moduli to obtain:

$$f(i\omega) = \frac{\sigma_0\omega(\cos \psi + i \sin \psi)}{(G'(\omega) - I\omega^2) + iG''(\omega)} \quad (5.19)$$

Multiplying top and bottom by the complex conjugate of the denominator leads to expressions for the real and imaginary parts of f as follows where G' represents $G'(\omega)$ & G'' represents $G''(\omega)$:

$$f_r = \frac{\sigma_0\omega((G' - I\omega^2) \cos \psi + G'' \sin \psi)}{(G' - I\omega^2)^2 + (G'')^2} \quad (5.20)$$

$$f_i = \frac{\sigma_0\omega((G' - I\omega^2) \sin \psi - G'' \cos \psi)}{(G' - I\omega^2)^2 + (G'')^2} \quad (5.21)$$

Hence, the contribution from the poles ($s = i\omega$) is expressed as:

$$\gamma_p(t) = \frac{\sigma_0[(G' - I\omega^2)\sin(\psi + \omega t) - G''\cos(\psi + \omega t)]}{(G'' - I\omega^2)^2 + (G')^2} \quad (5.22)$$

The complex moduli and the complex compliance are related via $J^* = 1/G^*$, where the real and imaginary parts are related through the expressions [49].

$$J' = \frac{G'}{G'^2 + G''^2} \quad (5.23)$$

$$J'' = \frac{G''}{G'^2 + G''^2} \quad (5.24)$$

Eqn 5.20 and Eqn 5.21 reduce to Hassager's [41] Eqn 13 and Eqn 14 when $I = 0$:

$$f_r = \sigma_0\omega(J' \cos \psi + J'' \sin \psi) \quad (5.25)$$

$$f_i = \sigma_0\omega(J' \sin \psi - J'' \cos \psi) \quad (5.26)$$

Finally, the poles associated with the roots of the term $g(s) + Is$ in the denominator of Eqn 5.13 are analysed. Without inertia, the function $g(s)$ has singularities associated with each relaxation time (τ_i), with one root (i.e. a pole of $y(s)$) intermediate between these singularities which corresponds to the retardation times (λ_j) of the multimode spectrum [41]. With inertia, the two mode Maxwell model has 3 roots instead of one. The function $g(s) + Is$ can be written as:

$$Is + \frac{\eta_1}{1 + s\tau_1} + \frac{\eta_2}{1 + s\tau_2} \quad (5.27)$$

By equating to zero, Eqn 5.27 can be rewritten as:

$$0 = (\eta_1)(1 + s\tau_2) + (\eta_2)(1 + s\tau_1) + Is(1 + s\tau_2)(1 + s\tau_1) \quad (5.28)$$

Expanding Eqn 5.28 leads to a 3rd polynomial, $as^3 + bs^2 + cs + d = 0$, with coefficients:

$$a = I\tau_2\tau_1 \quad (5.29)$$

$$b = (I\tau_2 + I\tau_1) \quad (5.30)$$

$$c = (\eta_1\tau_2 + \eta_2\tau_1 + I) \quad (5.31)$$

$$d = \eta_1 + \eta_2 \quad (5.32)$$

which can have one, two or three roots denoted as ρ_k , which easily can be found numerically. Having found the roots of the function $p(s) = g(s) + Is$ which appears in the denominator of Eqn 5.13, expanding $p(s)$ around the root to give:

$$p(s) = (s - \rho_k)(p'(\rho_k)) \quad (5.33)$$

where

$$p'(\rho_k) = I - \sum_i \frac{\eta_i\tau_i}{(1 + \rho_k\tau_i)^2} \quad (5.34)$$

and hence, the contribution to $y(s)$ corresponding to the 3 poles can be determined by taking the sum of the residuals of $y(s)e^{st}$ evaluated at each pole:

$$\gamma_t(t) = \sum_k \frac{\sigma_0(\omega \cos \phi + \rho_k \sin \phi) \exp(\rho_k t)}{\rho_k(p'(\rho_k))(\rho_k^2 + \omega^2)} \quad (5.35)$$

The strain profile can then be expressed as the sum of the offset, transient and periodic parts.

$$\gamma(t) = \gamma_{off} + \gamma_t(t) + \gamma_p(t) \quad (5.36)$$

5.2.1 Frequency Dependency

In order to gain a full understanding of inertial effects, the normalised strain profiles (normalised by the peak periodic strain (σ_0/G^*) because $G^* = \sigma_0/\gamma_0$) for the start up

of stress controlled oscillatory shear with and without inertia are compared for low, intermediate and high frequency ranges. A specified frequency is termed “low frequency” if the transient is negligible, “intermediate frequency” if there is an observable transient that decays to negligible magnitude within a single period of the oscillation and “high frequency” if the transient response persists beyond a single period.

In Fig 5.2 where $\omega = 0.1 \text{ rad s}^{-1}$, the inclusion of inertia in the model has negligible effects because the transient response is dwarfed by the periodic and offset components of the signal. It is clear that there is no difference between the inertia (Fig 5.2(a)) & inertialess cases (Fig 5.2(b)). In Fig 5.3, where $1.0 \text{ rad s}^{-1} \leq \omega \leq 10 \text{ rad s}^{-1}$, the increase in frequency leads to changes of the transient part in the initial response. In this case, the introduction of inertia in the model causes a damped oscillatory behaviour in the transient response which decays within the period of one oscillation. In Fig 5.4 where ($\omega > 10 \text{ rad s}^{-1}$), the inclusion of inertia in the model at these frequencies results in a response that shows damped oscillatory behaviour. In this case, the transient response takes longer than one period of the waveform to decay to a negligible magnitude hence these frequencies are termed “high frequency”. At high frequencies, special attention must be paid when undertaking experiments with regards to (i) inertia correction and (ii) allowing a sufficient conditioning time for the transients to decay prior to data acquisition. Finally, it can be observed that for the inertia-less cases, the amplitude of the signal remains independent of the applied frequency, but inclusion of inertia effects results in a reduction of the amplitude of the periodic signal in the high frequency range because most of the applied torque is used to accelerate the geometry/instrument. A coupling frequency is also caused by the presence of inertia and sample elasticity as observed in weak gels [6]. In Fig 5.5, the periodic shear stress amplitude is constant for low frequencies then gradually rises as frequency is increased until a peak (i.e. the coupling/resonant) frequency is reached then a steep decline is observed as frequency increases even further. This coupling frequency (between 1 and 100 Hz) is a regular occurrence in experiments performed with stress controlled (CMT) rheometers when sample elasticity is less than 10,000 Pa . Frequency sweeps performed around and above this coupling frequency corresponds to a shear stress sweep. When inertia effects are involved, the effective shear stress felt by the

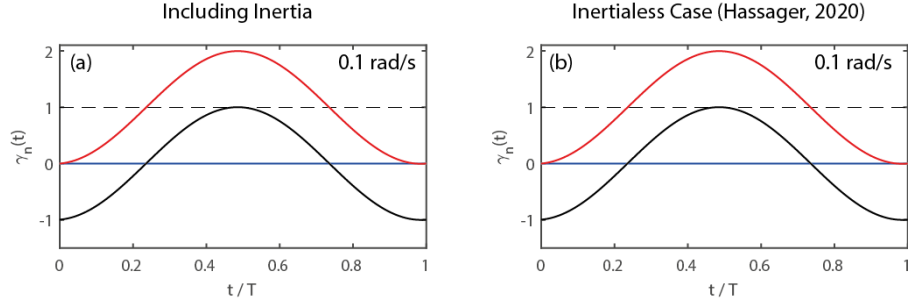


Figure 5.2: Low frequency ($\omega = 0.1 \text{ rad s}^{-1}$) response of a two mode Maxwell model ($\tau_1 = 0.01 \text{ s}$, $\tau_2 = 1.0 \text{ s}$, $\eta_1 = 1.0 \text{ Pa.s}$, $\eta_2 = 10.0 \text{ Pa.s}$, $I = 0.1 \text{ Pa.s}^2$) in the presence of instrument inertia (a) and in the inertia-less case (b). In both subfigures, the red line shows the complete solution, the dashed black line shows the offset (γ_{off}), the black line shows the steady state periodic response (γ_p) and the blue line shows the transient response (γ_t). At low frequencies, including inertia in the model has negligible effect as the transient response is insignificant in comparison to the periodic and offset terms.

material is different from the applied shear stress. Around the coupling frequency, the effective shear stress exceeds the applied shear stress. Above the coupling frequency, the effective shear stress is decreased and falls to zero at high frequencies. Simple analytical methods to improve the accuracy of oscillatory have been published [6]. This fundamental limitation of the CMT rheometer can be overcome by designing special transducer for an active control of the effective shear stress.

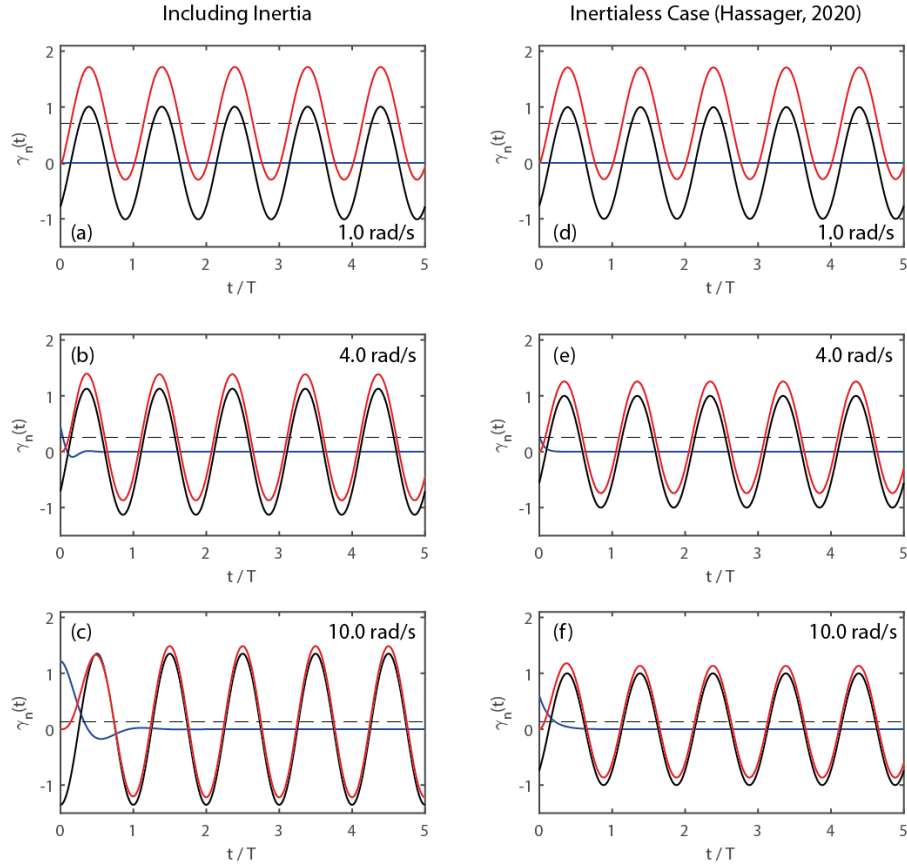


Figure 5.3: Intermediate frequency ($1.0\text{rad/s} \leq \omega \leq 10\text{rad/s}$) response of a two mode Maxwell model ($\tau_1 = 0.01\text{ s}$, $\tau_2 = 1.0\text{ s}$, $\eta_1 = 1.0\text{ Pa}\cdot\text{s}$, $\eta_2 = 10.0\text{ Pa}\cdot\text{s}$, $I = 0.1\text{ Pa}\cdot\text{s}^2$) in the presence of instrument inertia (a-c) and in the inertialess case (d-f). In all subfigures, the red line shows the complete solution, the dashed black line shows the offset (γ_{off}), the black line shows the steady state periodic response (γ_p) and the blue line shows the transient response (γ_t). As frequency increases the effect of the transient terms becomes more important in the initial response. At these frequencies the inclusion of inertia introduces a damped oscillatory behaviour to the transient response which decays within the period of one oscillation.

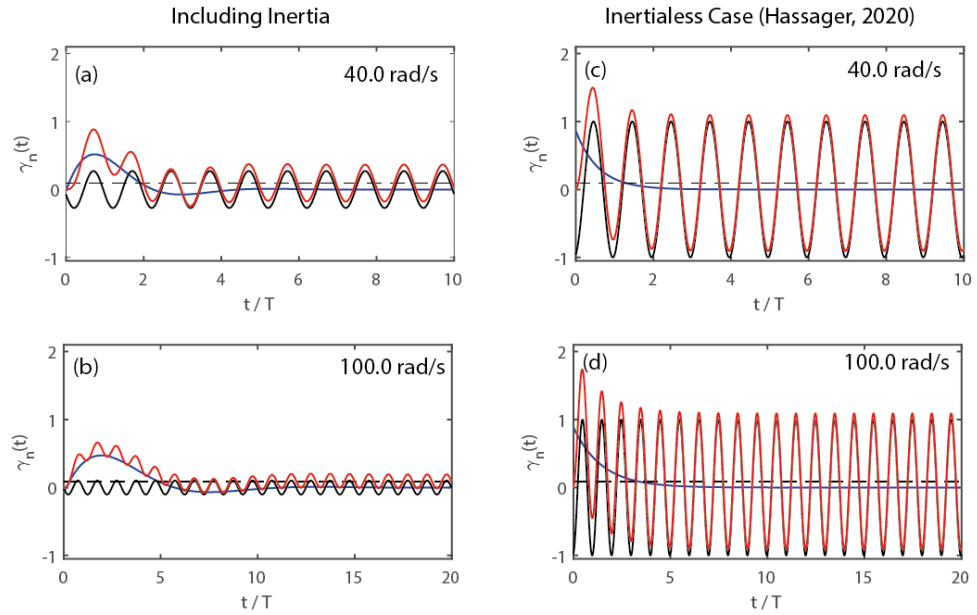


Figure 5.4: High frequency ($\omega > 10 \text{ rad s}^{-1}$) response of a two mode Maxwell model ($\tau_1 = 0.01 \text{ s}$, $\tau_2 = 1.0 \text{ s}$, $\eta_1 = 1.0 \text{ Pa.s}$, $\eta_2 = 10.0 \text{ Pa.s}$, $I = 0.1 \text{ Pa.s}^2$) in the presence of instrument inertia (a,b) and in the inertia-less case (c,d). In all subfigures the red line shows the complete solution, the dashed black line shows the offset (γ_{off}), the black line shows the steady state periodic response (γ_p) and the blue line shows the transient response (γ_t). the transient response takes takes longer than one period of the waveform to decay to a negligible magnitude

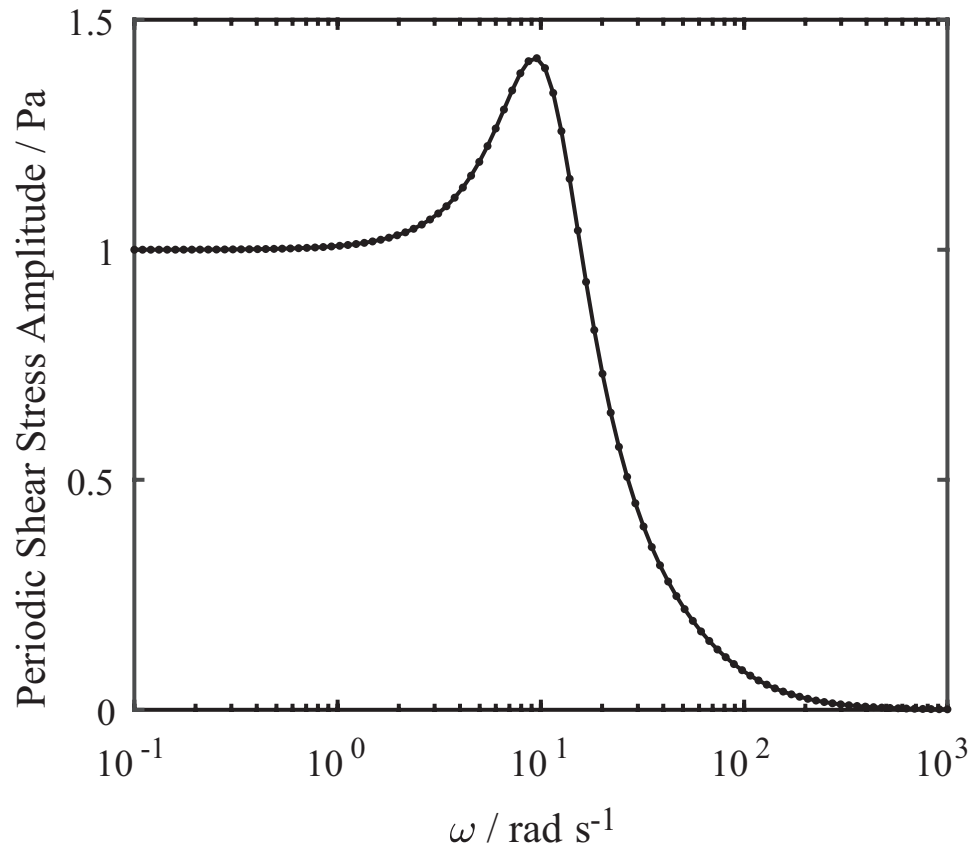


Figure 5.5: Amplitude of the periodic stress component as a function of frequency for a two mode Maxwell model ($\tau_1 = 0.01 \text{ s}$, $\tau_2 = 1.0 \text{ s}$, $\eta_1 = 1.0 \text{ Pa.s}$, $\eta_2 = 10.0 \text{ Pa.s}$, $I = 0.1 \text{ Pa.s}^2$).

5.2.2 Effect of Inertia on Conditioning Time

Conditioning time can be defined as the time which is allowed to elapse between the initiation of perturbation waveform and the collection of periodic data. The selection of a conditioning time is an important factor when designing stress controlled oscillatory experiments. According to Hassager [41], the transient response decay for an inertia-less case is $\exp(-t/\lambda_k)$. Hence, a conditioning time (t) of $\approx 4\lambda_k$ leads to a transient decay of about $\approx 2\%$ of its initial magnitude. In Fig 5.3 and Fig 5.4, the presence of inertia causes the transient term to persist for longer than its inertialess counter part for all frequencies. In Fig 5.6, the presence of inertia causes the pair of complex conjugate poles to be dominant over the single pole (i.e. they appear closer to the imaginary axis) and the real part of the complex conjugate pair lies to the right of the single pole of the inertialess case. The rate of decay of the transient response is predominantly determined by an effective retardation time, $\lambda_k = -1/Re[\rho_k^+]$ (where ρ_k^+ is the dominant pole). Hence, the selection of an appropriate conditioning time should involve the assessment of inertio-elastic effects with $t \approx 4\lambda^*$ which allows the transient to decay to $\approx 2\%$ of its initial magnitude. Direct observation of transient response is the quickest way to determine an appropriate conditioning time.

5.3 Experimental

5.3.1 Materials & Methods

Cetylpyridinium chloride (*CPyCl*) and sodium salicylate (*NaSal*) (Sigma-Aldrich) were dissolved at a molar ratio of 2:1 in 0.5 M sodium chloride (*NaCl*) solutions prepared using deionized H_2O . Appropriate quantities of dry of *NaCl*, *NaSal* and *CPyCl*, in powdered form, were added to H_2O in a fume hood. The mixtures were stirred for 24 hours at 40°C (in a sealed beaker atop a heated plate) to completely disperse the powder before measurements were performed. All chemicals were used as received without further purification [17]. A 4.1 wt% *CPyCl* solution has been reported to display shear thinning characteristics, this is referred to as the shear thinning solution (ST), herein.

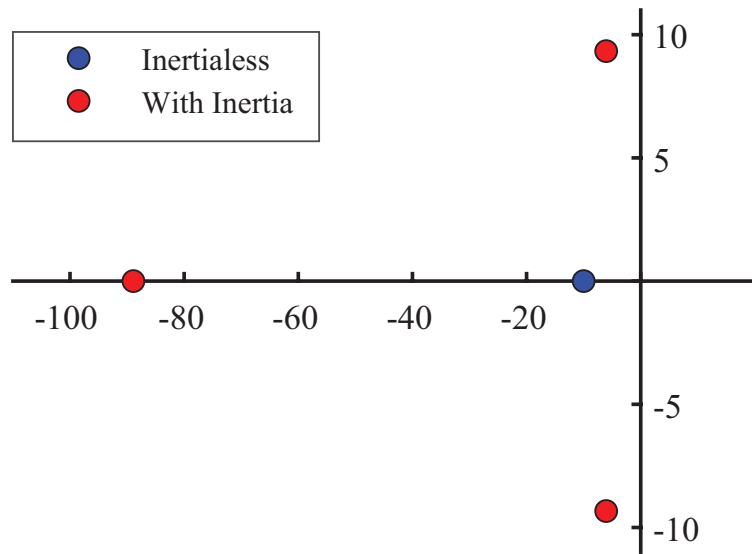


Figure 5.6: Pole plot for the ‘inertialess’ and ‘including inertia’ cases for a two mode Maxwell model ($\tau_1 = 0.01 s$, $\tau_2 = 1.0 s$, $\eta_1 = 1.0 Pa.s$, $\eta_2 = 10.0 Pa.s$, $I = 0.1 Pa.s^2$). Whilst the inertialess transient is characterised by a single real pole at $s = -1/\lambda_k$, inertia introduces a pair of complex conjugate poles which dominate the transient response and generate a dominant effective retardation time (λ^*).

This procedure has been reported in literature albeit at different temperatures [44][45]. The Small Amplitude Oscillatory tests (SAOS) as well as the transient experiments were carried out using a CMT HR-30 manufactured by TA instruments with a 60.0mm 2.00639° aluminium cone with a geometry inertia and instrument inertia of 8.79 and 21.02 μNms^2 , respectively. The sample was loaded and a thin layer silicon oil was added to prevent evaporation and scale formation which might introduce artefacts to the results. All experiments were carried out at 25°C. The peak stresses (σ_0), at each frequency were obtained via amplitude sweeps (Appendix B) with each peak stress safely in the linear viscoelastic region. The fitting procedure was made to include all frequencies ($\omega = 0.1, 1, 10, 100 \text{ rad s}^{-1}$) to minimize errors and obtain a uniform discrete relaxation spectra that describes the system. The storage and loss moduli transient expressions for a polymer melt without solvent viscosity is given as:

$$G' = \frac{\eta_1 \tau_1 \omega^2}{1 + \omega^2 \tau_1^2} + \frac{\eta_2 \tau_2 \omega^2}{1 + \omega^2 \tau_2^2} \quad (5.37)$$

$$G'' = \frac{\eta_1 \omega}{1 + \omega^2 \tau_1^2} + \frac{\eta_2 \omega}{1 + \omega^2 \tau_2^2} \quad (5.38)$$

5.3.2 Results & Discussion

In this section, the inertia effects caused by aluminium cone with a geometry inertia of 8.80 μNms^2 is investigated using a HR-30 CMT rheometer with a 4.1wt% *CPyCl* shear thinning (ST) WLM. In Fig 5.7, the SAOS data is fitted with a two mode Maxwell model (Eqn 5.37 & 5.38) to obtain the discrete relaxation spectrum (DRS) ($\tau_1, \tau_2, \eta_1, \eta_2$). It was established this particular WLM system can be captured accurately by a two mode Maxwell model, further increases in the number modes does not result in any noticeable improvement in capturing the data. In Fig 5.8, the predictions of Eqn 5.36 (blue lines) obtained from the discrete relaxation spectrum and the experimental transient data (red symbols) show excellent agreement between prediction and measured data over three decades of frequency. At $\omega = 0.1$ & $\omega = 1 \text{ rad s}^{-1}$, the low frequency regions, there are no interesting features noticed in the experimental (red symbols) and model (blue lines)

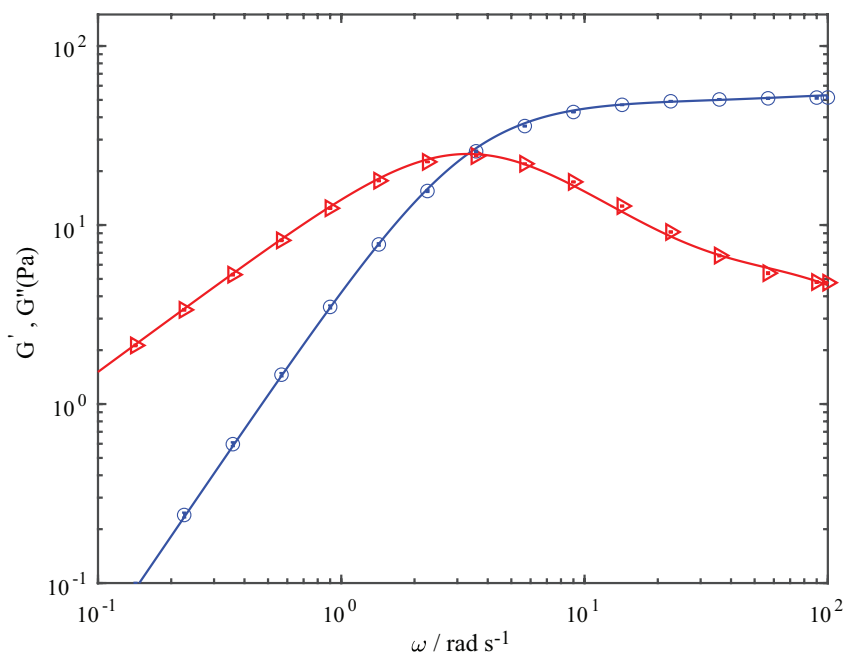


Figure 5.7: G' (blue) & G'' (red) SAOS data using aluminium cone geometry for a 4.1 wt% solution of *CPyCl* fitted with Eqn 5.37 & Eqn 5.38. The lines show a two mode Maxwell model fit to the experimental data using the discrete relaxation spectra. The discrete relaxation spectra is $\tau_1 = 0.0122$ s, $\tau_2 = 0.3038$ s, $\eta_1 = 0.0730$ Pa.s and $\eta_2 = 14.99$ Pa.s.

data with great agreement between both. At $\omega = 10$ rad s⁻¹, the intermediate frequency region, there is a slight rapidly decaying effect on the transient term captured by the experimental data and replicated by the inertia model (Eqn 5.36). At $\omega = 100$ rad s⁻¹, the high frequency region, there are noticeable effects on the transient part captured by the experimental data and replicated by the inertia model that lasts for ≈ 1 s before decaying into a steady state response. In essence, the validation of the measured strain waveforms with the predicted strain waveforms allows increased confidence in the data and discrete relaxation spectrum (DRS) from the SAOS data since small errors in the dynamic moduli ($G'(\omega)$ & $G''(\omega)$) lead to large deviations in the DRS.

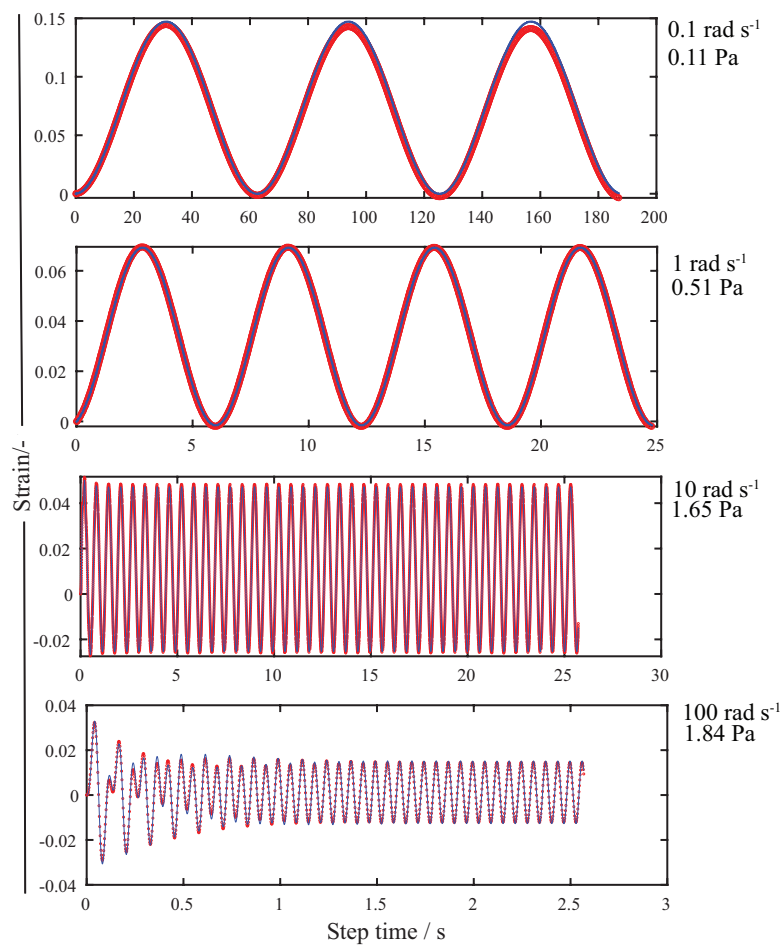


Figure 5.8: Transient data for start up of stress controlled oscillatory shear using aluminium cone geometry for a 4.1 wt% solution of *C_PyCl* fitted with Eqn 5.36 using a stress and strain constant of $17683.9 \text{ Pa}/N.m$ and 28.557 1/rad respectively. The red shapes are the experimental transient data for various frequencies and the blue lines are the model fits to the transient data.

5.4 Conclusion

Most users of rheometers are not equipped to deal with the complexities of inertia effects believing that simple calibrations via software are sufficient to reduce errors in the results. Herein, protocols are established for the inclusion of rheometer inertia in the analysis of the steady state periodic response to a stress controlled oscillatory perturbation, via the theory of linear viscoelasticity. In the inertia-less case devised by Hassager [41], the transient terms decay exponentially with time constants set by the retardation times of the discrete spectrum whereas the inclusion of inertia modifies the response to include inertio-elastic ringing similar to that seen in creep experiments [6][32][96]. The presence of rheometer inertia has an effect on the timescale for the establishment of the steady state periodic response. Hence, the inclusion of an appropriate conditioning time when designing experiments that rely on the steady state response for direct determination of dynamic moduli via the strain offset is important. One of the ways to select an appropriate conditioning time is to observe the transient response during the preliminary experiments. Recommendations for further research include investigating the effect of instrument inertia on experiments involving more complex waveforms like optimally windowed chirps [35] because these experiments rely on the transient response to the evolving frequency of the perturbation waveform to probe the materials rheological properties.

Chapter 6

Investigation of Negative Storage Modulus G'_{\parallel} in Parallel Superposition Rheometry via Brownian Dynamics

6.1 Introduction

Computational rheology is a subfield of rheology concerned with the design, development and implementation of numerical techniques that can simulate the behaviour of viscoelastic fluids [20][74]. Computational rheologists are tasked with the formulation of accurate numerical schemes that will predict the behaviour of viscoelastic fluids in complex flows. The process of creating accurate simulation techniques include two major steps which are the development of numerical algorithms and coarse graining procedures. Coarse graining can be simply defined as the simulation of complex systems using simplified forms i.e. from a molecular level to a mesoscopic level (bead-rod and bead-spring chains) [81].

It is possible to coarse grain from the atomic level to the bead-rod chain (Fig 6.3) and finally the bead-spring chain (Fig 6.1) (see section 6.2). This means that the Kuhn

steps, the distance between the beads of the bead-rod chain, are replaced by the entropic spring of the bead-spring chain which can be subjected to the FENE (finitely extensible nonlinear elastic) force law. It is possible for the coarse graining approximation to reach such a level that a whole single molecule can be presented by a single dumbbell with an entropic spring. Brownian dynamics has been used to investigate polymer chain dynamics under orthogonal conditions where small amplitude oscillatory shear is superimposed on a steady shear flow in different directions [64]. In this work, Brownian dynamic simulations are used with numerical techniques to investigate polymer chain dynamics under steady shear, SAOS and the superimposition of a steady shear flow on small amplitude oscillatory shear in the same direction (PSR), which can lead to the appearance of negative values of G'_{\parallel} under sufficiently low frequencies and high shear rates. The dynamics of polymer chains at conditions where negative values of G'_{\parallel} appear is an open question.

Theory of Polymer Models

The use of mechanical models has made understanding the complicated behaviour of macromolecules in solutions or melts easier. As described [11]: “An actual polymer molecule is an extremely complex mechanical system with an enormous number of degrees of freedom. To study the detailed motions of this complicated system and their relations to the nonequilibrium properties would be prohibitively difficult. As a result it has been customary for polymer scientists to resort to mechanical models to simulate the mechanical behavior of the macromolecule.” The complicated behaviour of macromolecules in melts and solutions is made easier with the use of molecular models. This is made possible because the macroscopic behaviour is dominated by microscale properties due to the large size of the macromolecules. Polymer molecules can be represented by a collection of beads linked by rigid rods or springs under Brownian motion. The multiple interactions between the molecules can be simplified through the analogy of a surrounding tube where the behaviour of a single molecule is compared to the average behaviour of its neighbours. This analogy was first proposed by De Gennes [27] and was mathematically described by Doi & Edwards [29].

The concept is simpler when dilute solutions are involved because the molecules are far apart and the hydrodynamic interactions are limited to the individual molecules. The Rouse chain represents single chain dynamics that have three model parameters: the number of beads, the Hookean force constant and hydrodynamic friction coefficient. The Rouse model can be used to obtain zero-shear rate viscosity and multiple relaxation modes in dilute polymers. In terms of non-linear rheological properties, the mathematical complexities mean that the chain is reduced to just two beads and a spring (the elastic dumbbell). The elastic dumbbell is the simplest representation of polymer molecules and can be used to predict conformational changes like orientation and stretch. They are useful in explaining the relationship between polymer dynamics and rheological phenomena [11]. The linear elastic dumbbell kinetic theory describes polymer chains as beads and interconnected springs in a newtonian solvent. The two beads have position vectors r_1, r_2 connected by an entropic spring (Fig 6.2). The equation of motion for the beads is the resultant of the spring force (F_i^S), the drag force (F_i^D) increases model accuracy and is dependent on the dumbbell end-to-end distance, and Brownian force (F_i^B) acting on the i th bead [74]. The simplicity of the elastic dumbbell means it cannot describe non-linear behaviour of dilute polymers. Although, the linear model described above can predict some polymer chain dynamics, it is limited by its unphysical properties in the sense that the chains can be stretched with no limit which is contrary to how polymers behave in reality. This is fixed by placing a non-linear force (Finitely Extensible Nonlinear Elastic (FENE)) law on the dumbbell model. The non-linear relationship between spring force and the deformation of the dumbbell means the spring will not stretch infinitely. In the FENE models, there is a link between the viscoelastic response and the conformation of the polymer chains. This non-linearity means that FENE models lack simple analytical solutions and needs to be solved via Brownian dynamics simulations to obtain the polymeric stress tensor [42].

Bead-Spring Simulation

The bead-spring chain (the Rouse model) in Fig 6.1 is made up of M beads connected by $N_s = M - 1$ entropic springs. The process of coarse graining leads to loss of internal

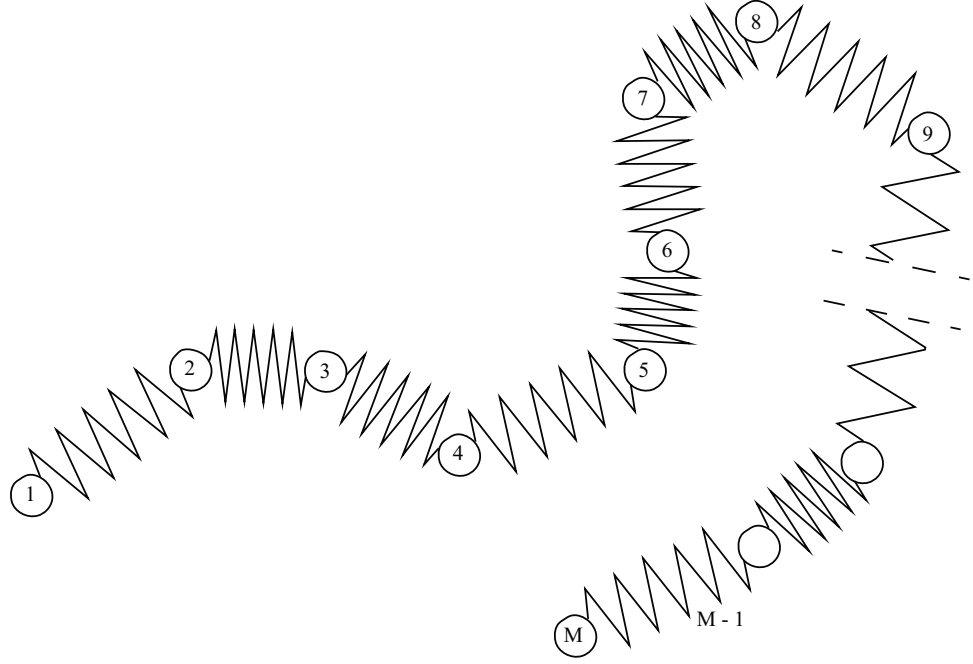


Figure 6.1: Freely-jointed multi-bead-spring model composed of M beads and $M - 1$ springs.

degrees of freedom which causes entropic effects that are represented by the springs. The beads serve as interaction points with the solvent. The sum of external forces acting on the beads is:

$$\mathbf{F}_i^H + \mathbf{F}_i^E + \mathbf{F}_i^B = 0, i = 1, 2, \dots, M \quad (6.1)$$

The subscript i is the bead number and $\mathbf{F}_i^H, \mathbf{F}_i^E, \mathbf{F}_i^B$ are the hydrodynamic drag force, the effective spring force and Brownian force respectively. The effective spring force acting on bead i is:

$$\mathbf{F}_i^E = \mathbf{F}_1^s; \quad \text{if } i = 1 \quad (6.2)$$

$$\mathbf{F}_i^E = \mathbf{F}_i^s - \mathbf{F}_{i-1}^s; \quad \text{if } 1 < i < M \quad (6.3)$$

$$\mathbf{F}_i^E = \mathbf{F}_{M-1}^s; \quad \text{if } i = M \quad (6.4)$$

where \mathbf{F}_i^s is the spring force of spring, i

The original FENE spring force as proposed by Warner [92] is:

$$\mathbf{F}^{FENE} = \frac{H_s \mathbf{Q}_i}{1 - Q^2/Q_0^2} \quad (6.5)$$

where H_s is the spring constant, Q is a three dimensional connector vector of the beads, $\mathbf{Q}_i = \mathbf{r}_{i+1} - \mathbf{r}_i$ is the connector vector of the i th spring, and Q_0 is the maximum possible spring length. The non-linearity of the spring force means that there are no simple analytical solutions available and closed constitutive equations for the polymeric stress tensor are non-existent.

The Hookean dumbbell (Fig 6.2) is used to describe dilute solutions of linear flexible polymers. It consists of two beads linked by a Hookean spring submerged in an incompressible newtonian fluid which is completely characterized by its viscosity (η_s) [73]. The dilute nature of the polymer solutions means there are no interactions between different chains. The beads represent chain segments of numerous monomers and the springs are the entropic representation of the effects on the end to end vector of the polymer. This model is limited to small deformations due to the gaussian distribution of the end- to -end vectors. In this case, the dumbbell can be stretched with no limits.

This unphysical behaviour can be corrected by dumbbells with FENE (finitely extensible non-linear elastic) spring forces. The evolution of the position vectors of the beads of the bead spring chain can be obtained from Eqn 6.1 as:

$$d\mathbf{r}_i = \left[\mathbf{u}_i^\infty + \frac{\mathbf{F}_i^E}{\zeta} \right] dt + \sqrt{\frac{2kT}{\zeta}} d\mathbf{W}_i, \quad i = 1, 2, \dots, M \quad (6.6)$$

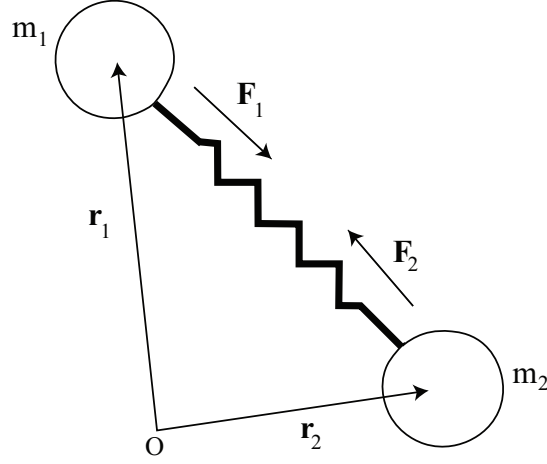


Figure 6.2: The Hookean dumbbell model

where $d\mathbf{W}_i$ is a Wiener process mathematically represented by a Gaussian random number with a mean of zero and variance dt , \mathbf{u}_i^∞ is the solvent velocity at bead i , $d\mathbf{r}_i$ is the velocity of the bead & ζ is the drag coefficient. The shear stress contribution coming from the suspended particles, τ_p is an important factor when modelling the intrinsic rheology response of a bead spring chain. The 3 major effects contributing to the total shear stress tensor are: (1) the intramolecular forces across the connector vector; (2) the external forces acting on the beads and (3) the transport of momentum caused by the displacement of the beads. There are other factors that contribute of the physics of this system but the listed factors are most important factors in the framework of a standard rheological test. The polymeric stress for a Kramers chain (Fig 6.3) is given as:

$$\tau_p = \sum_{i=1}^{N_s} \langle \mathbf{Q}_i \mathbf{F}_i^s \rangle \quad (6.7)$$

6.1.1 Integration Scheme

The FENE bead-spring chain dynamics can be written in terms of connector vectors (Q_i) replacing the bead positions (r_i) [81].

$$d\mathbf{Q}_i = [Pe(\boldsymbol{\kappa} \cdot \mathbf{Q}_i) + \frac{1}{4}(\mathbf{F}_{i-1}^s - 2\mathbf{F}_i^s + \mathbf{F}_{i+1}^s)]\delta t + \sqrt{\frac{1}{2}}(d\mathbf{W}_{i+1} - d\mathbf{W}_i) \quad (6.8)$$

for $i = 1, 2, \dots, N_s$. This equation is in its dimensionless form. The dimensionless spring force F_i^s for a FENE dumbbell is:

$$\mathbf{F}_i^s = \frac{\mathbf{Q}_i}{1 - Q_i^2/b} \quad (6.9)$$

where $b = H_s Q_0^2 / KT$ is the dimensionless extensibility parameter. It is important to note that b is not a free parameter, but roughly the number of monomer units represented by the dumbbell, and therefore b should be a large number ($b = 1000$) [92], $\boldsymbol{\kappa}$ is the transpose of the velocity gradient tensor and Pe is the bead peclet number, which can be interpreted as the ratio of the bead diffusion time to the characteristic flow time. The simplest way to integrate Eqn 6.8 is via a semi-implicit predictor-corrector integration scheme. In this case, the length of the connector vector, Q should not exceed the maximum permissible value of \sqrt{b} because it will lead to unphysical spring forces. The linear (Hookean) spring force puts no limits on the extent to which dumbbell can be stretched, this is termed an “unphysical behaviour” [42]. The semi-implicit predictor corrector scheme proposed by Somasi et al [81] is used to express our bead-spring chain dynamics (Eqn 6.10 to Eqn 6.14). The term “semi-implicit” refers to the fact that the force law, \bar{F}_i^s for any spring in the chain is either written explicitly from the previous timestep or solved implicitly through the cubic equation ensuring that no brownian step is rejected at any time during the simulation. This scheme is known to have an important advantage where the difference between the predictor and corrector provides useful information about the local error in each time step, which can be used for online improvement of simulations, for example by controlling a variable time-step width [73]. Implicit schemes allow the advantage of accessing smaller time steps and high stability but they are time consuming. The

numerical algorithm is described as follows:

Step 1. In the predictor step, $\mathbf{Q}_i(t_n)$ is explicitly updated to $\mathbf{Q}_i^*(t_n)$ as:

$$\mathbf{Q}_i^* = \mathbf{Q}_i^n + [Pe(\kappa \cdot \mathbf{Q}_i^n) + \frac{1}{4}(\mathbf{F}_{i-1}^{s,n} - 2\mathbf{F}_i^{s,n} + \mathbf{F}_{i+1}^{s,n})]\delta t + \sqrt{\frac{1}{2}}(d\mathbf{W}_{i+1}^n - d\mathbf{W}_i^n) \quad (6.10)$$

where $\mathbf{F}_i^{s,n}$ is the spring force for the i th segment at time $t = n\delta t$.

Step 2. In the corrector step, the spring forces for segments i and $i - 1$ are implicitly treated to obtain \mathbf{F}_i

$$\bar{\mathbf{Q}}_i + \frac{1}{2}(\delta t)\bar{\mathbf{F}}_i^s = \mathbf{Q}_i^n + [\frac{1}{2}Pe(\kappa \cdot \mathbf{Q}_i^n + \kappa \cdot \mathbf{Q}_i^*) + \frac{1}{4}(\bar{\mathbf{F}}_{i-1}^s + \mathbf{F}_{i+1}^{s,n})]\delta t + \sqrt{\frac{1}{2}}(d\mathbf{W}_{i+1}^n - d\mathbf{W}_i^n). \quad (6.11)$$

The magnitude of $\bar{\mathbf{Q}}_i$ for each i th spring in the chain can be obtained as a cubic equation from the rearrangement of the Eqn 6.11.

$$|\bar{\mathbf{Q}}_i|^3 - R|\bar{\mathbf{Q}}_i|^2 - b(1 + \frac{1}{2}(\delta t))|\mathbf{Q}_i| + bR = 0 \quad (6.12)$$

R is the magnitude of the right-hand side of Eqn 6.11 and b is the dimensionless extensibility parameter. $|\bar{\mathbf{Q}}_i|$ is never greater than \sqrt{b} because the cubic equation above has one unique root between 0 and \sqrt{b} which is selected. These equations work by calculating the relevant connector vectors and spring forces by sweeping through a seven bead chain with six springs. i.e. when $i = 1$, $\bar{\mathbf{F}}_{i-1}^s$ resolves to zero meaning the right-hand side of Eqn 6.11 can be calculated easily. Hence, $\bar{\mathbf{Q}}_1$ can be obtained via Eqn 6.12 which is the used to calculate $\bar{\mathbf{F}}_1^s$ from Eqn 6.9. In the next bead where $i = 2$, the right side of Eqn 6.11 can be calculated because $\bar{\mathbf{F}}_{i-1}^s$ resolves to $\bar{\mathbf{F}}_1^s$ obtained from the previous bead, $i = 1$, hence $\bar{\mathbf{Q}}_2$ and $\bar{\mathbf{F}}_2^s$ can be calculated from the relevant equations. This process continues until all the relevant forces and connector vectors for the each individual bead of a 7 bead spring chain is obtained. This same method is used in the last corrector step described below.

Step 3. For the last corrector step, the spring forces for segments i and $i - 1$ are implicitly

treated and the spring force for the segment $i + 1$ is derived from step 2.

$$\mathbf{Q}_i^{n+1} + \frac{1}{2}(\delta t)\mathbf{F}_i^{s,n+1} = \mathbf{Q}_i^n + \left[\frac{1}{2}Pe(\kappa \cdot \mathbf{Q}_i^n + \kappa \cdot \bar{\mathbf{Q}}_i) + \frac{1}{4}(\mathbf{F}_{i-1}^{s,n+1} + \mathbf{F}_{i+1}^s)\right]\delta t + \sqrt{\frac{1}{2}}(d\mathbf{W}_{i+1}^n - d\mathbf{W}_i^n) \quad (6.13)$$

The residual is calculated as the difference between the solutions $\bar{\mathbf{Q}}_i$ and $\bar{\mathbf{Q}}_i^{n+1}$

$$\epsilon = \sqrt{\sum_{i=1}^{N_s} (\mathbf{Q}_i^{n+1} - \bar{\mathbf{Q}}_i)^2} \quad (6.14)$$

$\bar{\mathbf{Q}}_i$ is replaced by \mathbf{Q}_i^{n+1} when the residual (ϵ) is greater than the specified tolerance (10^{-6}) and step 3 is repeated until convergence.

6.2 Validation

MATLAB was selected as the software to build the simulation over Python, C++ and Fortran because of its user friendly nature and prepackaged functions that would otherwise have to be built from scratch. High Powered Computing (HPC) is a service provided by SUPERCOMPUTING WALES [2] that allows computationally intensive calculations to be performed over numerous processing cores. The average personal computer (PC) can have 4-6 processing cores but HPC allows a maximum of 35 processing cores, drastically reducing computational cost (the time required to complete the simulations is reduced). It also provides a cloud based storage system where large files can be stored and accessed as required. A detailed description of the MATLAB code required to produce Brownian dynamic simulations for polymer chains is found in Appendix C.

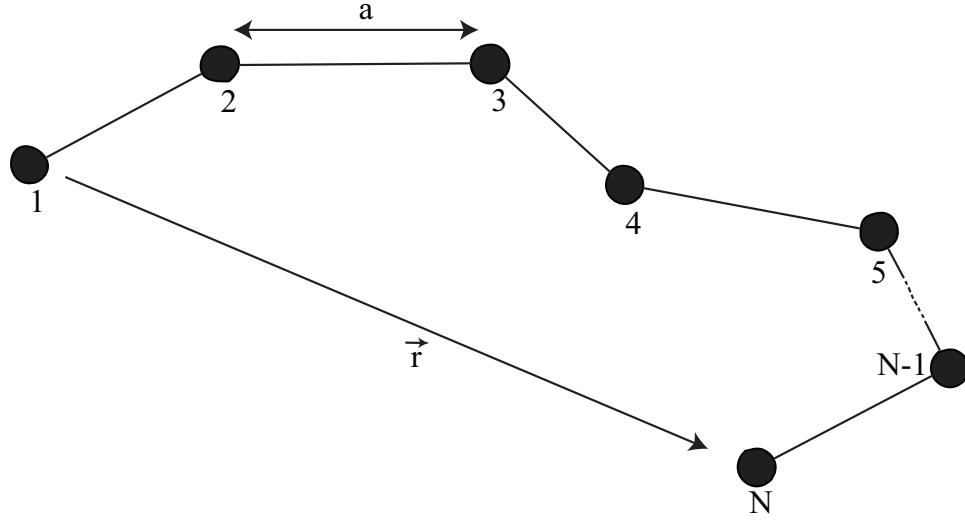


Figure 6.3: The freely jointed bead-rod chain (Kramers chain) model for a polymer chain

6.2.1 Equilibrium properties

The maximum extension of a FENE bead spring chain is [81]:

$$N_s Q_0 = N_s \sqrt{b} \quad (6.15)$$

where N_s is the number of beads in the FENE chain, b is the dimensionless extensibility parameter and Q_0 is the maximum possible spring length.

A Kramers chain is a coarse-grained bead-rod model. The length of a fully stretched Kramers chain (Fig 6.3) has been established [81]:

$$L = (N_k - 1)a \quad (6.16)$$

where N_k is the number of beads for a Kramers chain and a is the length of the connecting rods. The length of a fully stretched FENE bead spring chain has not been established in literature but a vital relationship relationship between b , N_k & number of bead springs (N_s) is given as [42]:

$$N_k = \frac{bN_s}{3} + 1 \quad (6.17)$$

Substituting Eqn 6.17 into Eqn 6.16 and equating the result with Eqn 6.15 leads to a relationship between a of a Kramers chain and b of a FENE chain:

$$a = \frac{3}{\sqrt{b}} \quad (6.18)$$

For a Kramers chain, the end to end equilibrium distance $\langle r_{eq}^2 \rangle$ [11] is given as:

$$\langle r_{eq}^2 \rangle = N_k a^2 \quad (6.19)$$

The appropriate substitutions will allow us to derive the equilibrium end to end distance for a FENE spring chain:

$$\langle r_{eq}^2 \rangle = \frac{3(bN_s + 3)}{b} \quad (6.20)$$

The end to end distance of a Hookean dumbbell is obtained from the accepted values of Q obtained in Eqn 6.13 and is calculated as [11]:

$$\langle EE \rangle = \langle \sum Q_{eq}^2 \rangle \quad (6.21)$$

The time constant, $\lambda_H = \zeta/(4H)$ can be made dimensionless with the relaxation time of a Hookean dumbbell, $\zeta/(4H)$ hence for the BD simulations, $\lambda_H = 1$.

Another important factor in BD simulations when employing implicit integration schemes is the time step. In Chinesta et al [22], the evolution of the squared end to end distance is presented for different time steps (Δt) using a population of 10^4 dumbbells. They observed that a complete divergence of the scheme is observed when the timestep is greater than the main relaxation time while convergence towards the central values can be observed as the time step gets smaller than a tenth of the relaxation time as shown in Fig 6.5. They also conclude that the numerical considerations extracted from the BD simulations with Hookean-dumbbells can be extrapolated to the BD simulations of ≥ 1000 multi-bead-spring chains. Applying these considerations to the FENE bead spring chains, the end to end equilibrium distance (Fig 6.4) shows equilibrium is reached at any time, $t > 50 s$. As the number of chains is increased, there is a noticeable reduction in the noise of the simulation i.e. averaging over a increasing number of chains reduces

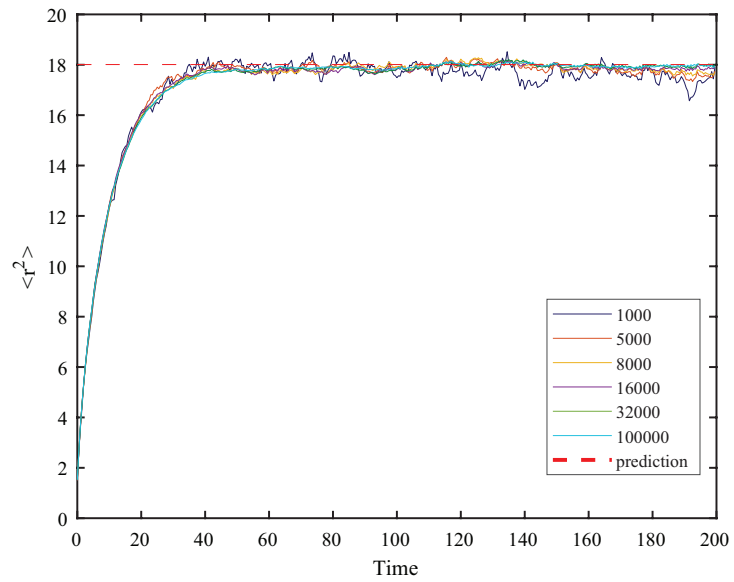


Figure 6.4: Evolution of the reduced square end-to-end distance of a bead spring for a time step (Δt) of $\lambda_H/100$. Different chain populations have been employed & $\lambda_H = 1$. The simulated data is calculated from Eqn 6.21 & the red dashed line is calculated from Eqn 6.20.

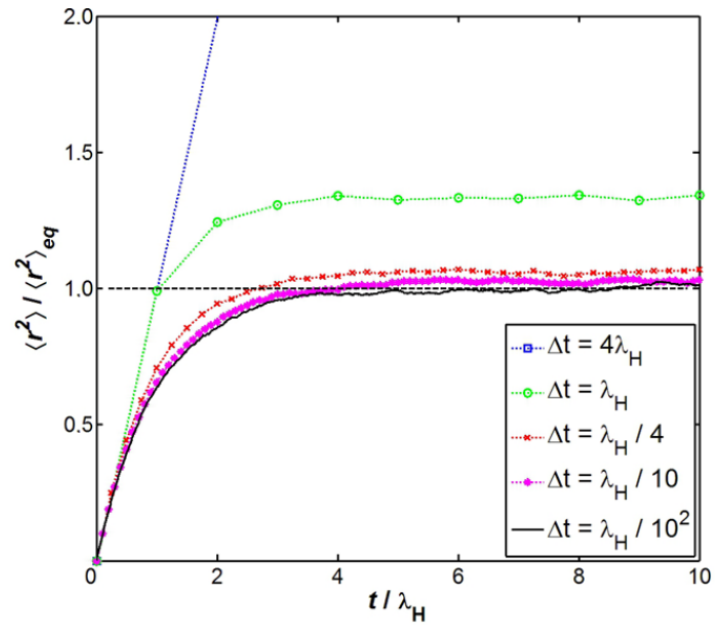


Figure 6.5: Evolution of the reduced square end-to-end distance of a dumbbell after sudden thermal activation for different time steps in the BD simulation. The Square end-to-end distance is made dimensionless using the equilibrium value given by the kinetic theory. A population of 10^4 dumbbells has been employed. Reproduced from Ref [22] with permission from SPRINGER VERLAG.

the standard deviation from the ideal. After the simulation has been allowed to reach equilibrium, the correct end-to-end distance of a FENE bead spring chain is obtained. The simulations show good convergence at a timestep of $\Delta t = \lambda_H/100$.

6.2.2 Steady Shear Simulations

In Fig 6.6, the results of simulations of viscosity, η at different values of ultimate shear rates (Pe) are displayed. The bead peclet number (Pe) is the ratio of the bead diffusion time to the characteristic flow time, $Pe = \dot{\gamma}(\zeta a^2/\kappa T)$. The numerical algorithms ensure that all time constants are non-dimensionalized to 1 hence shear rate ($\dot{\gamma}$) and Peclet number (Pe) are equivalent. Viscosity is a ratio of the stress to the Peclet number, there is less noise at $Pe = 10$ and $Pe = 100$ because the stress is much greater than the noise at those values. At $Pe = 0.1$, the value of the stress is close to the noise level, hence the data is erratic. At high shear rates, the viscosity overshoots where the stresses go thorough a maxima before decreasing to their steady state values. As the shear rate increases, the overshoot occurs sooner. There is excellent agreement between the steady shear results obtained from the present simulations and Tanner’s analytical solutions [93] as shown in Fig 6.6 (bottom row) as well as experimental data for dilute solutions [46]. This establishes confidence that the simulations is able to accurately simulate steady shear conditions. The viscosity is calculated using Eqn 6.22.

$$\eta = \frac{\sigma_{BD}}{\dot{\gamma}} \tag{6.22}$$

where simulation stress, σ_{BD} is derived from Eqn 6.7. Tanner’s work uses analytical equations to generate these viscosity curves hence the data appears as smooth lines. Replicating the steady shear data via Brownian dynamics with an integration scheme at $\Delta t = 0.1$ results in noisy data. Reducing the timestep will reduce statistical noise resulting in smoother curves.

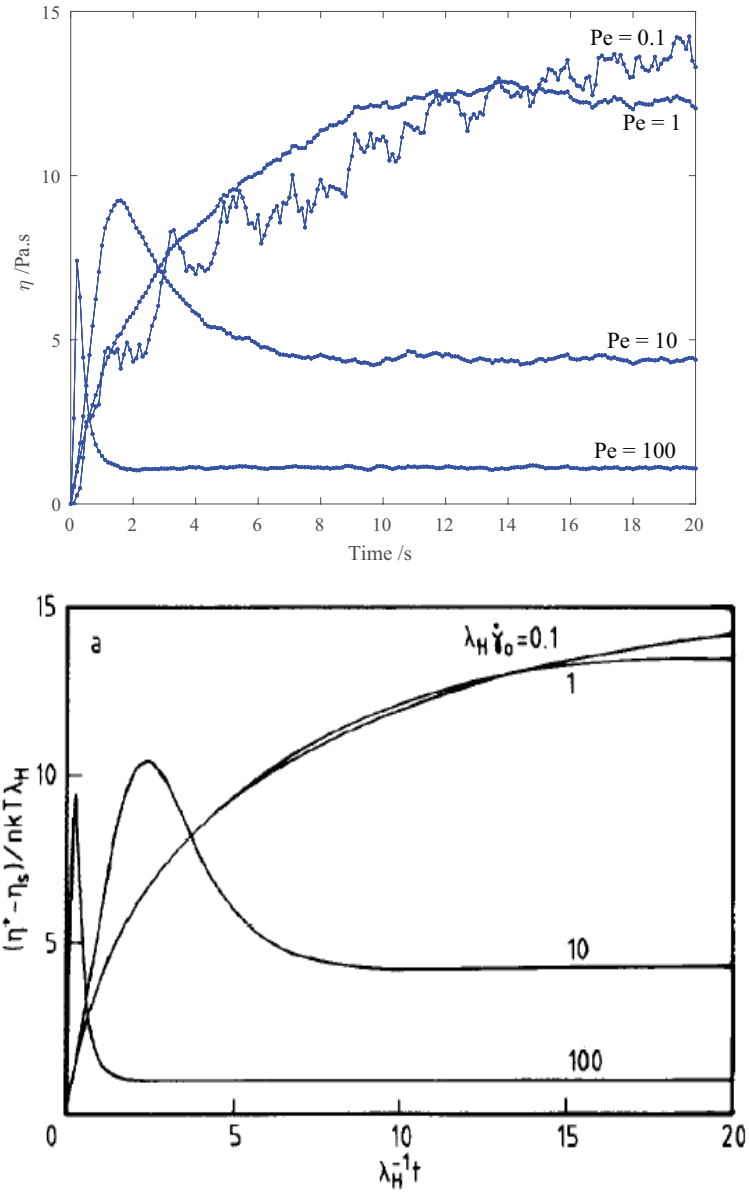


Figure 6.6: The growth of the viscosity at several shear rates for seven bead chains where $N_{chains} = 1000$, $b = 100$ and $\Delta t = 0.1$ calculated using Eqn 6.22 & Eqn 6.7. The top image shows the results of the simulations and the bottom shows the results publish by Tanner & Wiest [93].

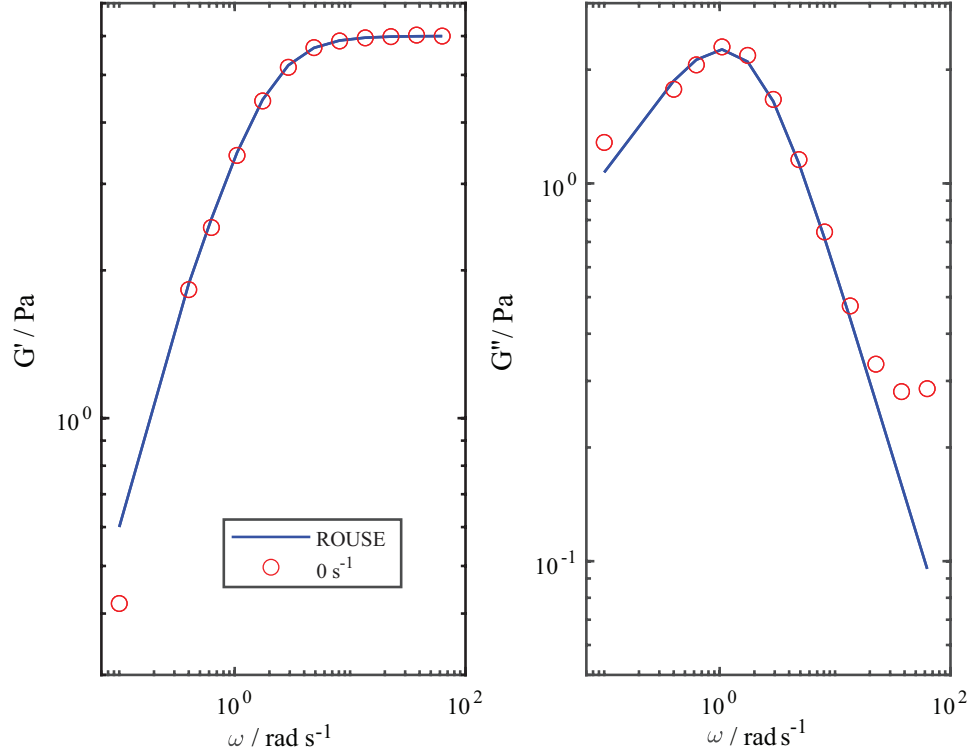


Figure 6.7: The BD prediction for storage and loss modulus at SAOS compared to the Rouse model represented by a solid blue line at various frequencies, ω .

6.2.3 Small Amplitude Oscillatory Shear (SAOS)

The validity of this simulation can also be verified with SAOS simulations. For BD simulations, SAOS conditions are established at $\dot{\gamma}$ or $Pe=0$. These results can be compared with analytical solutions from the Rouse chain in a frequency sweep simulation. In Fig 6.7, there is good agreement between the G' and Rouse model for frequencies, $\omega > 0.1 \text{ rad s}^{-1}$. For the G'' , there is good agreement for a range of frequencies but poor agreement at $\omega < 0.4 \text{ rad s}^{-1}$ and $\omega > 8 \text{ rad s}^{-1}$.

The value of G' from the numerical simulation differs from the analytical results at $\omega = 0.1 \text{ rad s}^{-1}$. This poor accuracy is caused by weak signals generated using a total time of 200 s where the period of the signal is $2\pi/0.1 = 64 \text{ s}$. The signal to noise ratio is poor at these conditions. This discrepancy is not observed at high frequencies for the storage

modulus because it increases with frequency far above any resolution limit of the system. A similar issue is observed at $\omega = 0.1 \text{ rad s}^{-1}$ for the loss modulus (G'') and further discrepancies are observed at high frequencies. This was also observed by Chinesta [22] who attributed the discrepancies to bad resolutions of the integration scheme when the phase angle approaches 0° (loss modulus initially increases with frequency then decreases at higher frequencies tending towards 0 i.e. elastic behaviour). This error can be resolved by employing shorter time steps but it should be noted that model behaviour at such frequencies lack any physical interpretation.

The relaxation times for the Rouse model (Hookean dumbbell) is given as [11]:

$$\lambda_j = \frac{\zeta/2H}{4 \sin^2(j\pi/2N)} \quad (6.23)$$

where $\frac{\zeta}{H} = 1$, $j = N - 1$ is the number of springs and N is the number of beads. The Rouse material functions can be calculated as:

$$G' = \sum_{j=1}^{n-1} \frac{\lambda_j^2 \omega^2}{1 + (\lambda_j \omega)^2} \quad (6.24)$$

$$G'' = \sum_{j=1}^{n-1} \frac{\lambda_j \omega}{1 + (\lambda_j \omega)^2} \quad (6.25)$$

The values of G' and G'' for the simulated data are obtained by fitting the stress and strain values to the equation of an ellipse (Eqn 6.27) via the least squared method. This procedure results in values for the coefficients a and b respectively.

$$a\sigma^2 + b\sigma\gamma + c\gamma^2 = 1 \quad (6.26)$$

$$ax^2 + bxy + cy = 1 \quad (6.27)$$

The storage and loss modulus can be obtained from a tilted ellipse as shown in Fig 6.8. The complete derivations can be found in appendix C.

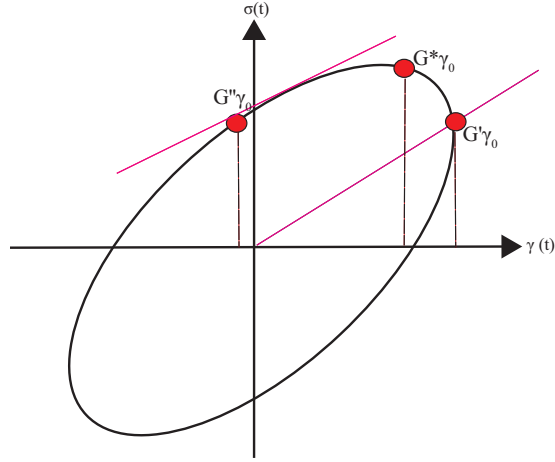


Figure 6.8: The Lissajous curves of a viscoelastic material represented by a tilted ellipse from which the storage and loss modulus may be obtained.

$$G'' = \sqrt{\frac{1}{a\gamma_0^2}} \quad (6.28)$$

$$G' = \frac{-b\gamma_0^2 G''^2}{2} \quad (6.29)$$

The Lissajous curves from the simulations (blue shapes) are plotted with the stress values obtained from Eqn 6.7. The strain, after equilibration is calculated as:

$$\gamma = \gamma_0 \sin(\omega t) \quad (6.30)$$

where γ_0 is the strain amplitude. G' and G'' can be used to construct the Lissajous curves (red lines) using the equation for stress below:

$$\sigma_t = G' \gamma_0 \sin(\omega t) + G'' \gamma_0 \cos(\omega t). \quad (6.31)$$

The Lissajous curves in Fig 6.9 show a comparison between the BD simulations (Blue circles) and the fitted Lissajous curves (red lines) as an assessment of the quality of the fit. It is important to note that the simulated Lissajous curves are constructed by adding the individual waves and dividing over the total number of waves to obtain an average waveform. At $\omega = 0.1 \text{ rad s}^{-1}$, there are massive discrepancies between the two curves hence the data at low frequencies cannot be trusted but good data can be obtained at 0.4 rad s^{-1} and above. The signal is weak at 0.1 rad s^{-1} at a total time of 200 s . In the following pages, different methods are used to increase signal strength.

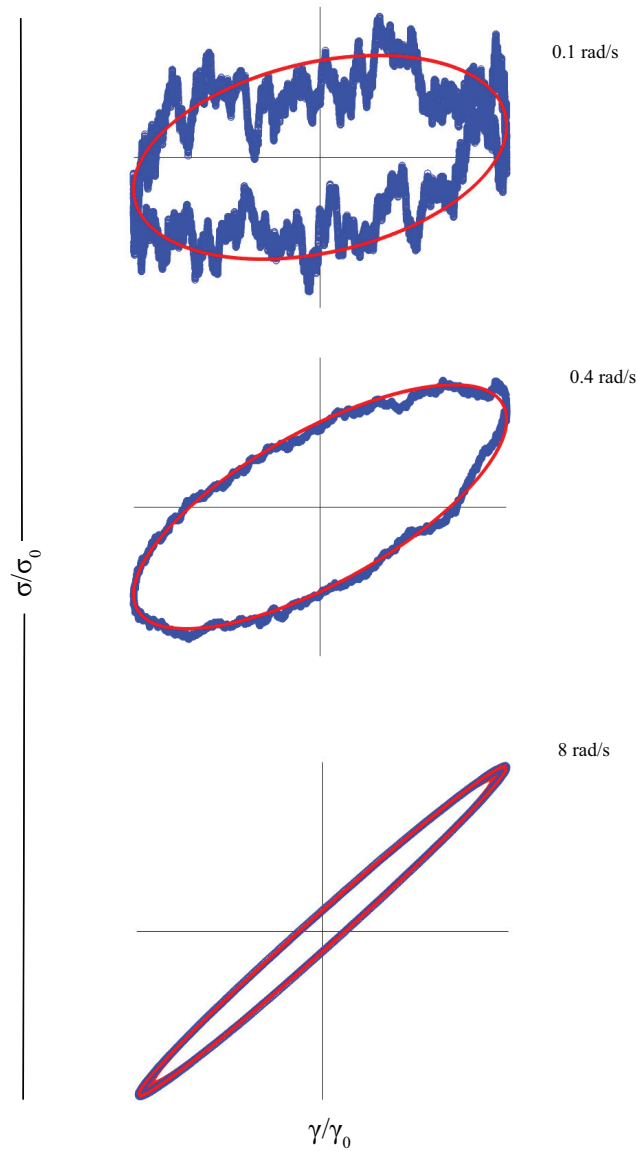


Figure 6.9: Lissajous plots of BD simulations at increasing frequencies of 0.1 rad s^{-1} , 0.4 rad s^{-1} & 8 rad s^{-1} for a BD total time of 200 s and $\gamma_0 = 0.1$. These curves are normalized stress versus normalized strain. The red lines are calculated with Eqn 6.30 & 6.31 while the blue circles represent stress and strain from the BD simulations.

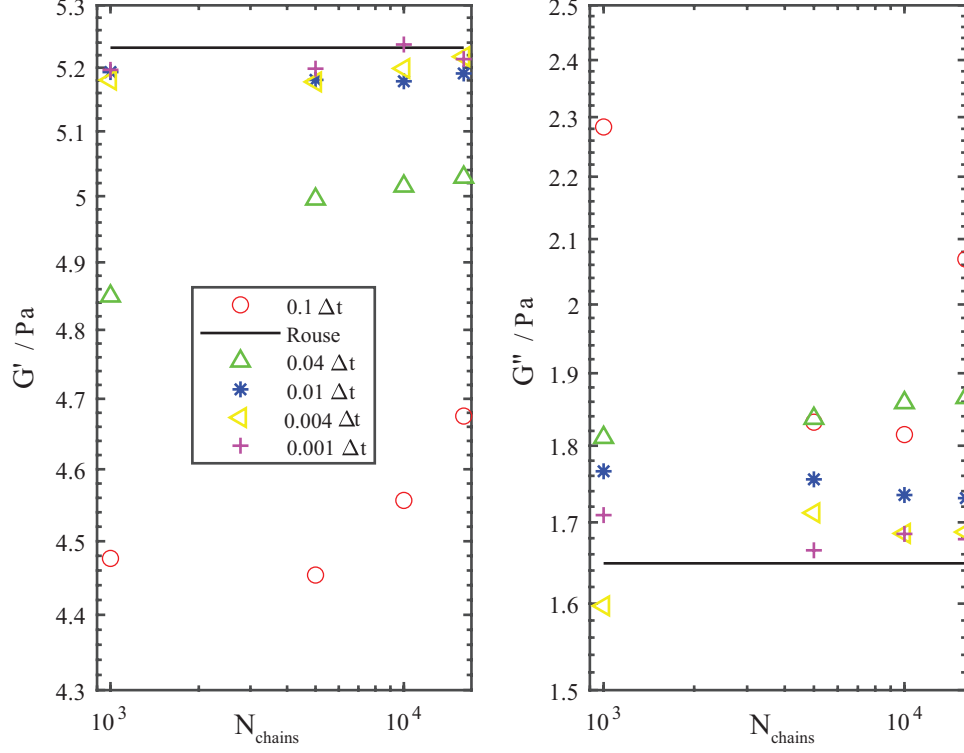


Figure 6.10: The BD predictions for storage modulus (G') and loss modulus (G'') at $\dot{\gamma}$ or $Pe = 0$ for different chain populations (N_{chains}) at different timesteps (Δt) at $\omega = 2.91 \text{ rad s}^{-1}$ compared to the Rouse chain predictions (G' & G'') represented with a solid black line at the same frequency (ω).

6.3 Optimization

The Optimization process involves selecting the best parameters that will lead to accurate results and the Rouse chain predictions serve as a benchmark to measure the performance of a BD simulation. This process involves the management of Number of chains (N_{chains}) and timestep (Δt) whilst ensuring the accuracy of Storage modulus (G') and loss modulus (G''). The simulated moduli are compared with Rouse chain moduli using Eqn 6.24 & Eqn 6.25 at $\omega = 2.91 \text{ rad s}^{-1}$.

In Fig 6.10, the storage modulus, G' , for different chain populations at different timesteps,

Δt is compared with the Rouse chain. The results show that reducing Δt leads to an increase in G' towards the ideal Rouse chain values. At a $\Delta t = 0.1$, increasing the number of chains results in a marginal increase in G' . At the $\Delta t = 0.01$, increasing the number of chains barely affects the storage modulus even as the storage moduli is closer to the ideal. At the $\Delta t = 0.001$, the best results that match the Rouse model at 1000, 5000, 16000 chains are obtained. The loss modulus follows the same trend but in reverse. Decreasing the Δt leads to a reduction in G'' towards the ideal Rouse chain values. The variation of G' and G'' with Δt is displayed in Fig 6.11. There is a sharp increase in G' towards the ideal Rouse prediction as Δt is decreased from 0.1 to 0.001. There is steep decline towards the ideal in the G'' as Δt is reduced. This same trend is observed as the number of chains is increased. The best results are derived from $\Delta t < 0.01$ & $N_{chains} > 1000$. In Fig 6.12, computation time drastically increases as Δt is decreased. For all Δt , increasing the N_{chains} leads to increases in computational time. As Δt is decreased, the range of computational time also increases. The time required to complete a BD simulation for 16000 chains and $\Delta t = 0.001$ is 66 hours while the required time for 5000 chains and $\Delta t = 0.001$ is 21 hours. There is a limitation on SUPERCOMPUTING WALES (HPC) service where all simulations are terminated after 72 hours and there are often large wait times before a simulation can be processed. Although operating for longer times with larger number of chains is desirable, the benefits of running the simulations for 72 hours are insignificant. It might be possible to obtain better results especially at low frequencies if the simulations can run for 3 to 4 weeks but constraints limit our parameters to 5000 chains and $\Delta t = 0.001$ at 21 hours.

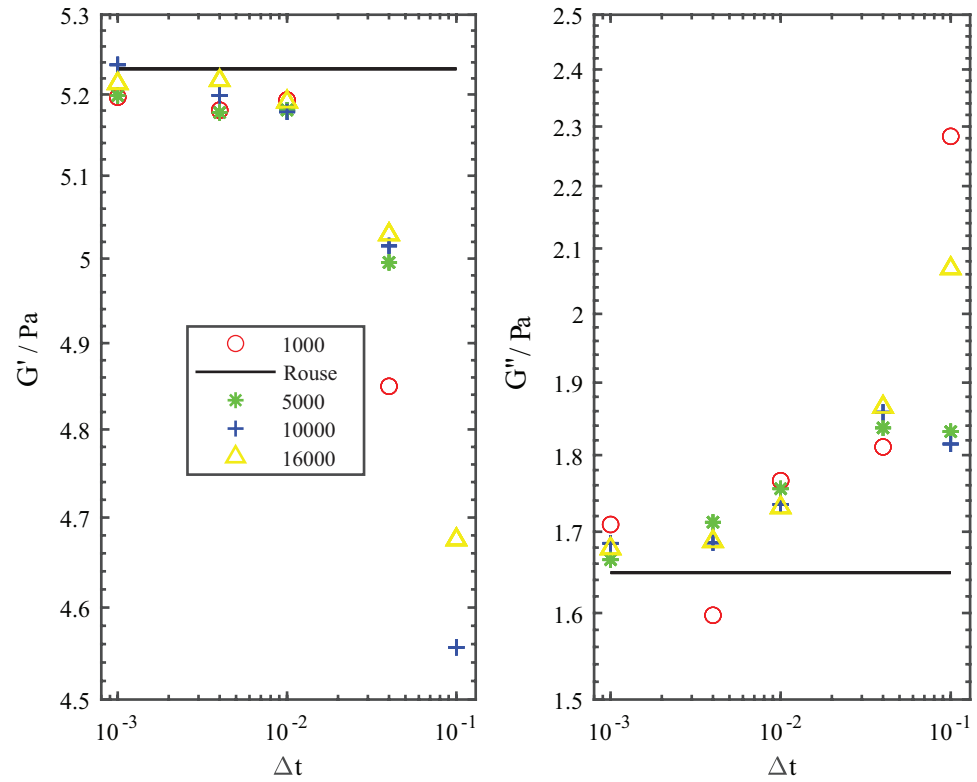


Figure 6.11: The BD predictions for storage modulus (G') and loss modulus (G'') at $\dot{\gamma}$ or $Pe = 0$ vs Δt for different chain populations, N_{chains} at $\omega = 2.91 \text{ rad s}^{-1}$ compared to the Rouse chain predictions (G' & G'') represented with a solid black line at the same frequency, ω .

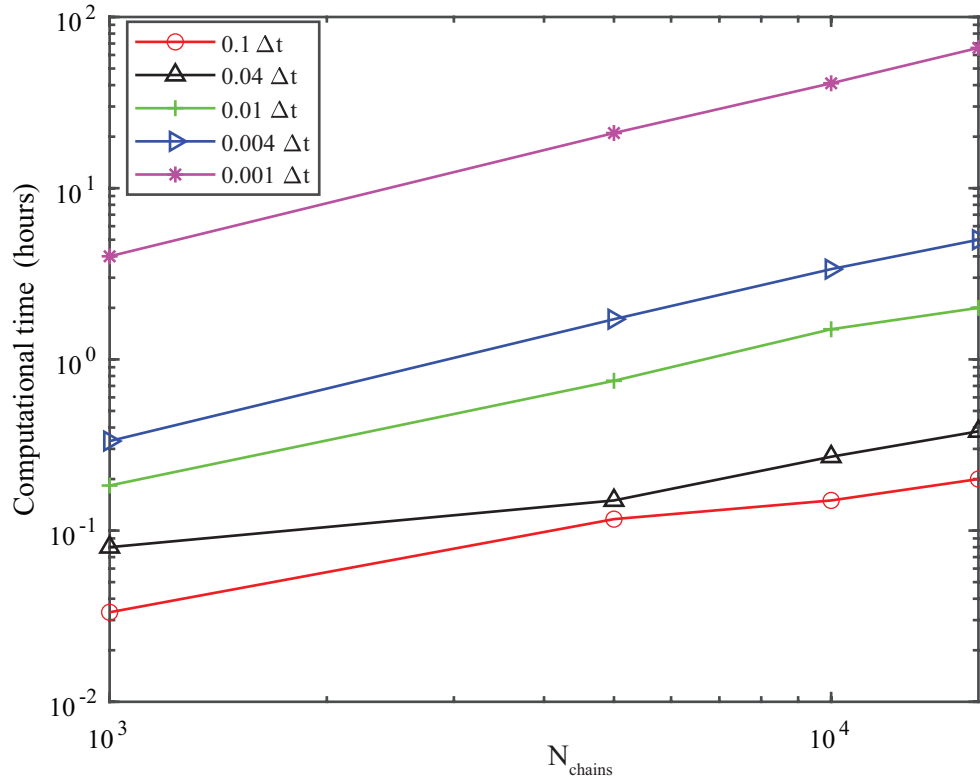


Figure 6.12: The CPU time required to complete BD simulations for different number of Chains, N_{chains} at $\omega = 2.91 \text{ rad s}^{-1}$ for different timesteps (Δt).

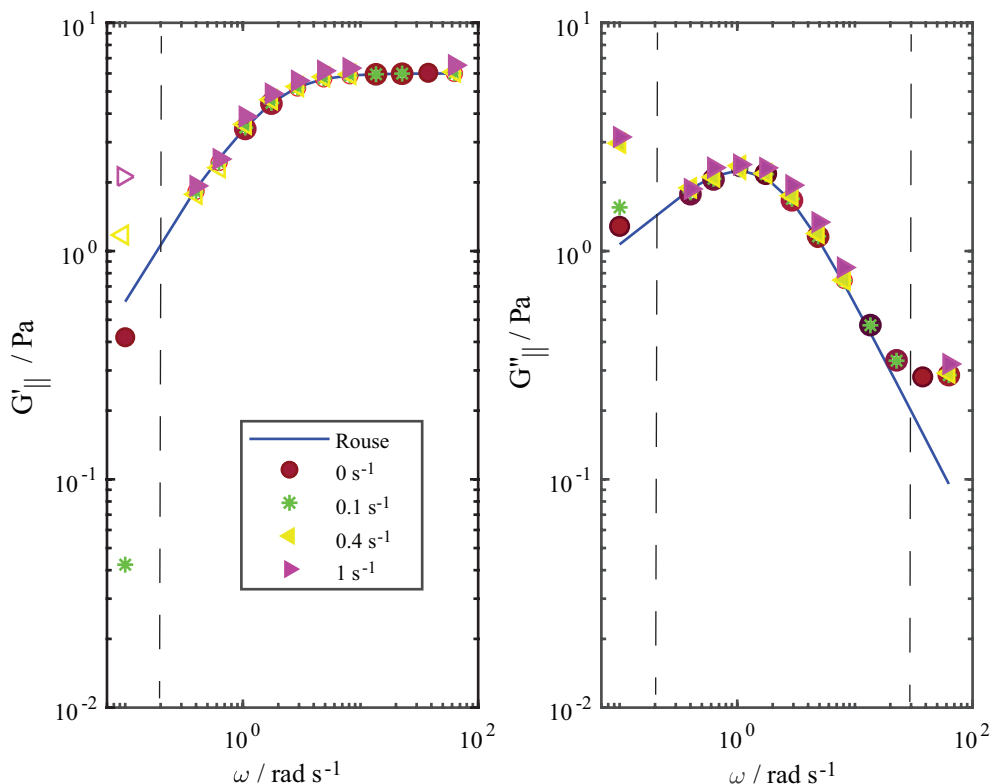


Figure 6.13: Parallel Superposition Rheometry performed by a BD simulation at low shear rates (shapes, open shapes represent absolute values of any negative data) and compared with the Rouse model (solid blue line). The black dashed lines are used to denote the region of acceptable data.

6.4 Parallel Superposition Simulations

The aim of this section is to simulate a PSR experiment (small amplitude oscillations superimposed on steady shear ($\dot{\gamma}$) in the parallel direction) and investigate chain dynamics that result in the appearance of negative values of $G'_{||}$.

In Fig 6.13, there is good agreement between the SAOS, Rouse model and $\dot{\gamma} = 0.1 \text{ s}^{-1}$, 0.4 s^{-1} and 1 s^{-1} for $\omega > 0.1 \text{ rad s}^{-1}$. There is poor resolution at low frequencies due to high statistical noise. This is also observed in experimental data shown in Appendix A where the noise is noticeable at low frequencies in both amplitude and frequency sweeps.

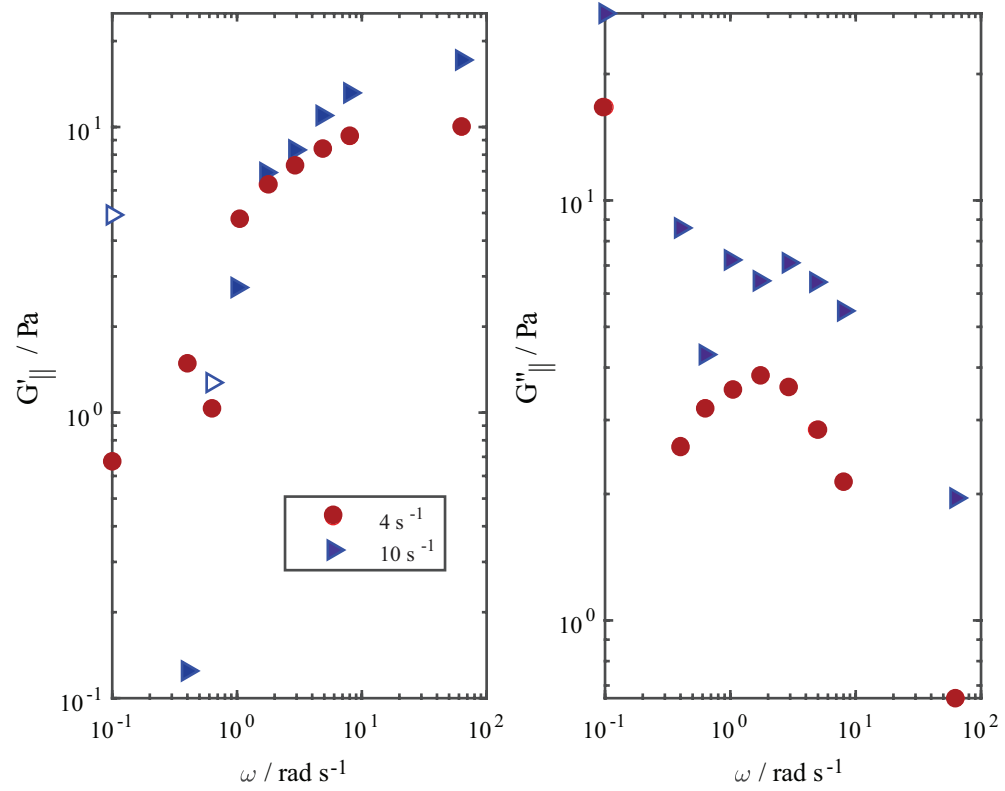


Figure 6.14: Parallel Superposition Rheometry performed by a BD simulation at High shear rates (shapes), open shapes represent absolute values of any negative data.

The poor resolution at high frequency ($\omega > 8 \text{ rad s}^{-1}$) for the loss modulus is because phase angle tends towards 0 as frequency increases.

The appearance of negative values of G'_{\parallel} at sufficiently low frequencies, $\omega = 0.1 \text{ rad s}^{-1}$ at 0.4 s^{-1} and 1 s^{-1} are also observed. In Fig 6.14, there is an appearance of negative values of G'_{\parallel} at 0.1 rad s^{-1} and 0.63 rad s^{-1} at $\dot{\gamma} = 10 \text{ s}^{-1}$. The validity of the data can be checked by constructing Lissajous curves. In Fig 6.15, a high level of noise is observed in the Lissajous curve for each $\dot{\gamma}$ that results in negative values of G'_{\parallel} at a total simulation time of 200 s . The simulated results (blue shapes) do not form ellipses (open spaces are observed) as a result of noise (weak signals). The period of the signal is calculated as $T = 2\pi/0.1 = 63 \text{ s}$ and the total simulation time is 200 s , hence the signal is weak at these conditions because the data is averaged over only 3 periods. If the signal at 0.1 rad s^{-1} is too weak at 200 s , slightly increasing the frequency to 0.63 rad s^{-1} to obtain more waves should help reduce the noise as observed in Fig 6.16. The curves show a marginal reduction in noise as the amplitude is reduced but there are spiked artefacts at the extremes that indicate some non-linear effects. The results are noisy at $\omega = 0.63 \text{ rad s}^{-1}$ and the artefacts at the extremes can be reduced by reducing the amplitude (the spiked artefacts are prominent at $\gamma_0 = 0.1$ and less prominent as the amplitude is reduced). This means a total time of 200 s cannot generate strong signals at the frequencies where negative values of G'_{\parallel} are likely to be found. In Fig 6.17, the signal is strengthened by drastically increasing total time but Δt is increased from 0.001 to 0.01 in order to reduce computational time. Negative values of G'_{\parallel} can be observed along with a drastic reduction in noise by increasing total time (t). At total times of 1000 s , 2000 s & 3000 s , the artefacts observed in Fig 6.16 are removed and the noise in the simulation is reduced although the Lissajous curves still differ.

In Fig 6.18, the experimental Lissajous curves for a WLM subjected to parallel superposition rheometry shows negative values of G'_{\parallel} at sufficiently low frequencies. Extremely low frequencies ($\omega = 0.14 \text{ rad s}^{-1}$) result in noisy curves indicating that negative data cannot be trusted. At $\omega = 1.42 \text{ rad s}^{-1}$ & $\omega = 2.26 \text{ rad s}^{-1}$, the Lissajous curves have reduced noise indicating that the data can be trusted.

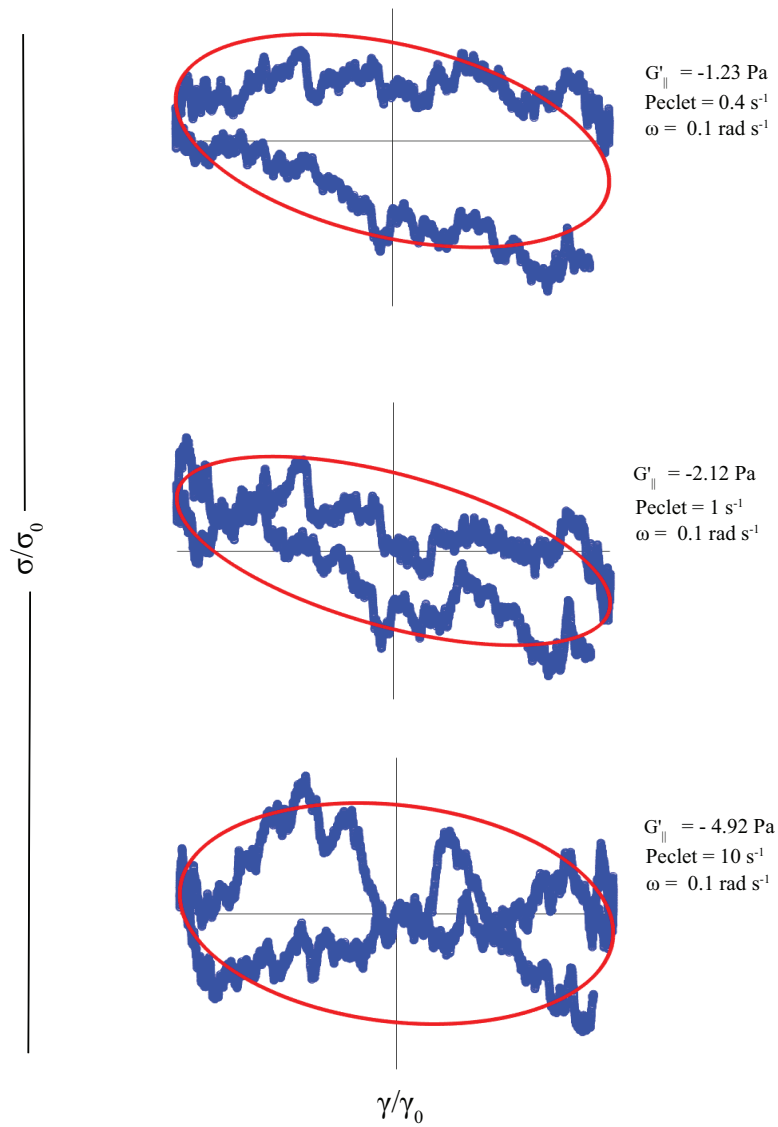


Figure 6.15: The Lissajous curves for BD simulations at the appearance of negative values G'_{\parallel} at $\gamma_0 = 0.1$ & $\Delta t = 0.001$ and 5000 chains and a simulation time of 200 s. These curves are normalized stress versus normalized strain. The red lines are calculated with Eqn 6.30 & 6.31 while the blue circles represent stress and strain from the BD simulations.

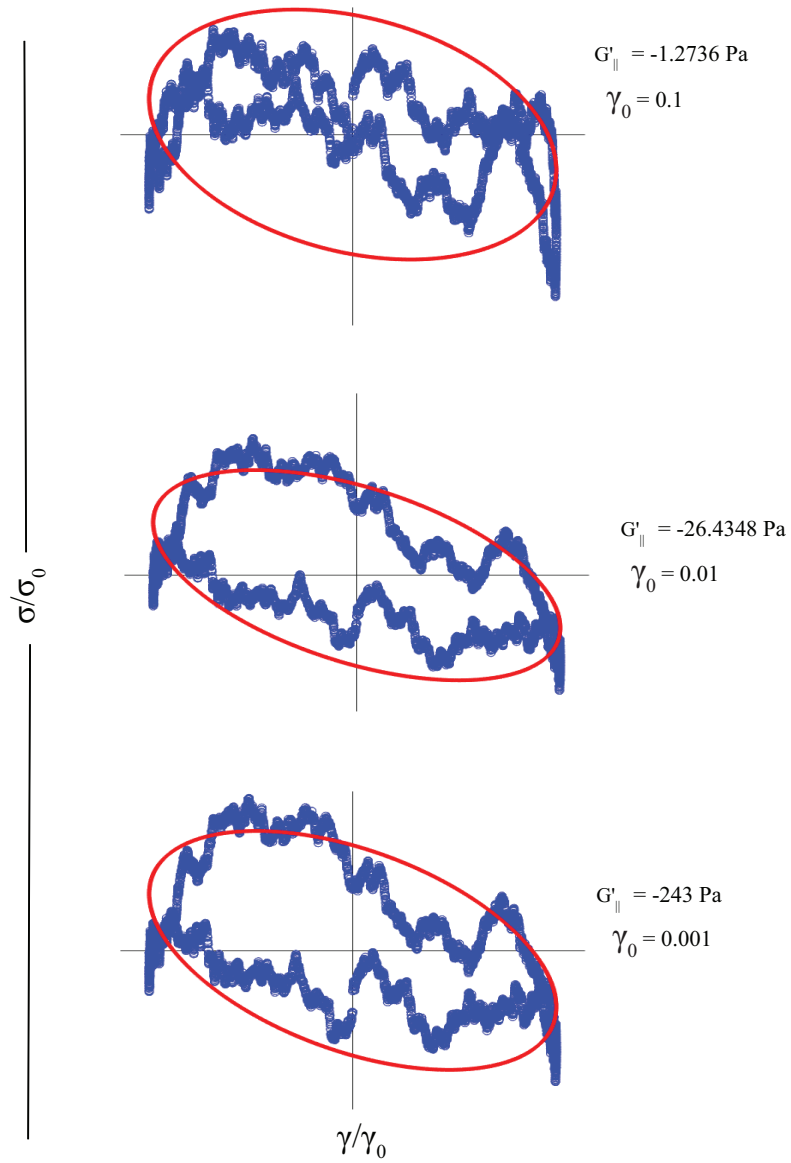


Figure 6.16: The Lissajous curves for 10 s^{-1} at $\omega = 0.63 \text{ rad s}^{-1}$ for 5000 chains , $\Delta t = 0.001$, total time = 200 s and decreasing oscillation amplitude, γ_0 . The red lines are calculated with Eqn 6.30 & 6.31 while the blue circles represent stress and strain from the BD simulations.

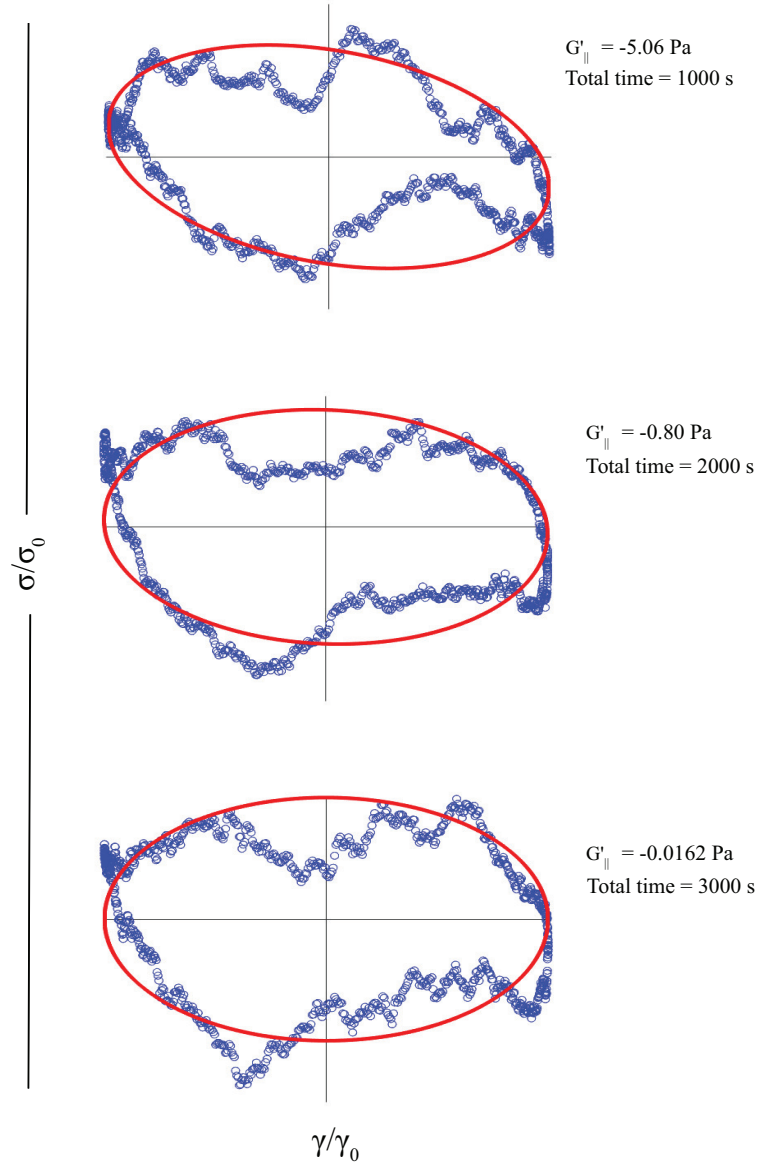


Figure 6.17: The Lissajous curves for 10 s^{-1} at $\omega = 0.63 \text{ rad s}^{-1}$ for 5000 chains, $\Delta t = 0.01$ and increasing total time, t at $\gamma_0 = 0.01$. The red lines are calculated with Eqn 6.30 & 6.31 while the blue circles represent stress and strain from the BD simulations.

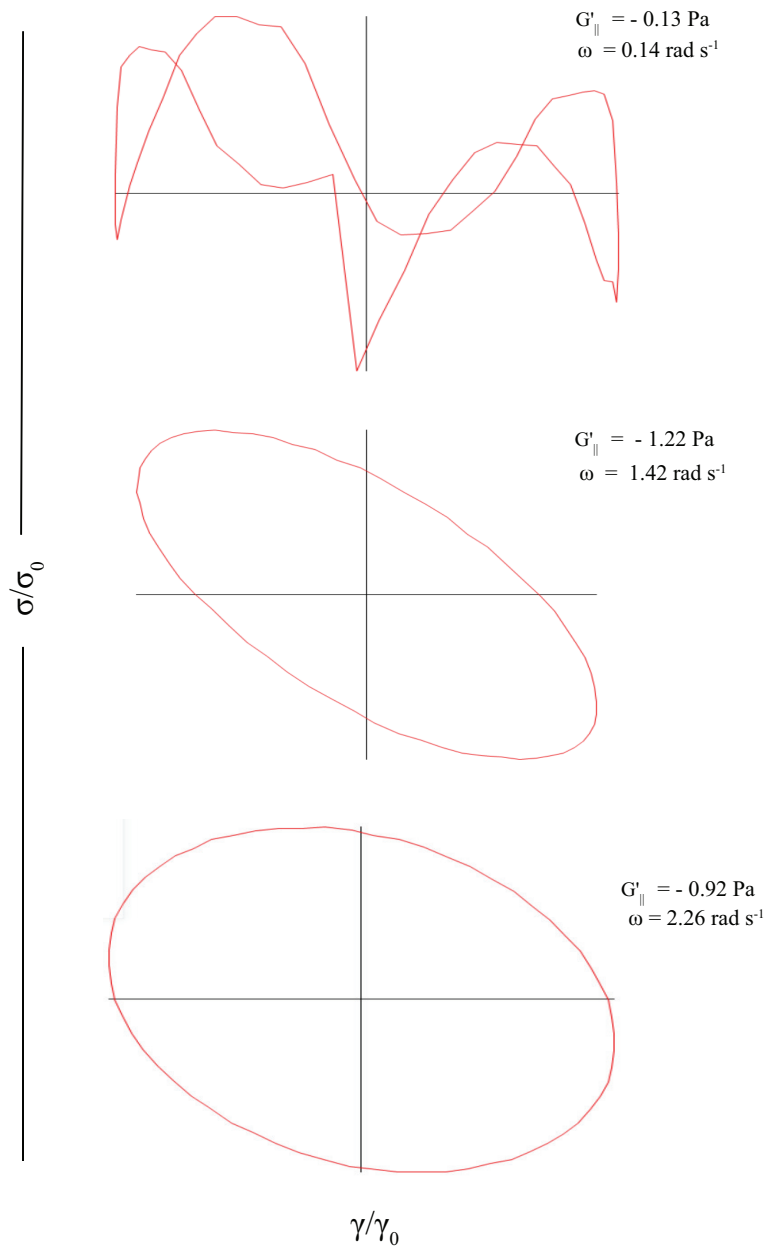


Figure 6.18: Experimental Lissajous curves for a WLM using ARES G2 with double wall concentric cylinder at various frequencies.

6.5 Conclusions

In this chapter, the predictor corrector scheme proposed by Somasi et al [81] is constructed with MATLAB and processed via High Powered Computing to accurately simulate steady shear which was compared with results by Tanner et al [93] and simulate SAOS compared with results by Chinesta et al [22]. This work tackles issue of the appearance of negative values of G'_{\parallel} by superimposing small amplitude oscillations on steady shear in a parallel direction. Although the BD simulations generated negative storage modulus at sufficiently low frequencies, the signals generated at low frequencies proved too weak to reveal any reasonable insights into the chain dynamics. Even under SAOS conditions, the signal at low frequencies is so weak that superimposing a steady shear in the parallel direction is bound to increase the complexities of this procedure. It is shown that increasing total time can reduce the noise to a certain extent, despite this improvement, these curves cannot be trusted. In theory, it would be possible to facilitate accurate PSR simulation via Brownian dynamics, if every parameter is maximized by increasing the Number of chains, further reducing Δt , increasing the total time, t and deriving more sophisticated algorithms but this would require a large amount of computational cost (computational time and hundreds of CPU cores). These are recommendations for further work. These limitations mean that no clear conclusion on the nature of negative storage modulus observed in experimental and simulated Lissajous curves can be made from the present studies.

Chapter 7

Conclusion & Recommendations

The research presented in this thesis contains 3 independent studies tackling issues in constitutive modelling, experimental rheology and computational rheology. In chapter 4, the dynamics of Worm Like Micelles (WLMs) are investigated with superposition rheometry experiments and constitutive models. Kim et al [54] developed analytical PSR and OSR equations of the Giesekus model which were used to model a shear banding (SB) and shear thinning (ST) WLM where good agreement with experimental data is observed at all conditions except for the SB sample at 10 s^{-1} . Analytical PSR and OSR equations for the Co-rotational Maxwell Model (CRM) developed by Curtis & Davies [25] were used to model shear banding and shear thinning WLMs in this chapter. Two modes of analysis were used. In the weakly non-linear case, the assumption was made that the micro-structure of the materials is constant regardless of the shear rate employed. Under these conditions, the CRM shows poor agreement with the experimental data at high shear rates ($> 0.4 \text{ s}^{-1}$) whilst showing good agreements at low shear rates. In the strongly non-linear case, the assumption was made that the micro-structure of the materials changes with shear rate (each shear rate was treated as a separate material). Under this condition, the CRM shows poor agreement with experimental data at high shear rates for both types of WLM. Since the CRM is known for its excessive shear thinning and its lack of a non-linear parameter, the Gordon-Schowalter model (GS) was introduced because of its slip parameter which moderates excessive shear thinning and represents non-linear

behaviours of polymer solutions. In the weakly non-linear case, the GS model shows poor agreement with experimental data at high shear rates for both shear thinning and shear banding cases whilst showing good agreement at low shear rates. In the strongly non-linear case, the GS model performs well at $\dot{\gamma} = 4 \text{ s}^{-1}$ and fails at $\dot{\gamma} = 10 \text{ s}^{-1}$ for the shear thinning WLM. For the shear banding WLM, the model shows poor agreement at both shear rates. The present results show that the 3 models can effectively capture WLM dynamics up to $\dot{\gamma} = 1 \text{ s}^{-1}$. Above this shear rate, the GIE model shows relatively good performance except in regions of shear banding and the GS model under analysis B showed promising results for shear thinning and shear banding WLMs. The literature has indicated that other models such as the reptation-reaction (RR) model developed by Cates [16] may be better at modelling the dynamics of WLMs. This procedure can also be improved via the introduction of damping functions that modify the parameters of the model as a function of shear rate. This is beyond the scope of this analysis and are recommendations for further work.

One of the major issues affecting experimental rheology is the presence of inertia in Combined Motor Transducer (CMT) rheometers. There is sufficient literature confirming the adverse effects of inertia on experimental data (inertia effects can appear as real data) especially at high frequencies. In chapter 5, the effects of rheometer inertia (including instrument and geometry contributions) on the establishment of the steady state periodic response to a stress controlled oscillatory perturbation were investigated. Hassager [41] approached this problem via the theory of linear viscoelasticity but neglected the inertia effects. Inertia effects are introduced as an improvement to Hassager’s model in this chapter. The analysis confirms that inertia has no effect on the offset portion of the signal. At low frequencies, the effects of inertia on the periodic and transient terms are negligible but as the frequency increases inertia effects causes a damped oscillatory behaviour on the transient behavior which decays within specific period. At high frequencies, the transient response decays after longer periods displaying damped oscillatory behaviour. This confirms that sufficient conditioning time must be employed to allow the transient to decay prior to data acquisition. The timescale for the establishment of the steady state periodic response is also affected by the presence of rheometer inertia. The

analysis is supplemented with experiments using a cone and plate geometry where inertia effects are used to model the start of oscillatory shear for a WLM where the model captures inertia effects at $\omega = 10 \text{ rad s}^{-1}$ & 100 rad s^{-1} . The discrete relaxation spectra obtained by fitting the experimental SAOS data was used to predict the transient behaviour of the WLM with great accuracy using the new inertia model. Investigations on the effects of instrument inertia when using complex waveforms like optimally windowed chirps are beyond the scope of this analysis and are recommendations for further works.

In chapter 6, Brownian dynamics is used to investigate the nature of negative storage moduli observed in chapter 3. The accuracy of numerical algorithms developed by Somasi [81] can be increased by reducing the timesteps (Δt) at the cost of longer processing hours. The steady shear behaviour of polymer chains was simulated successfully using Brownian dynamics with great agreement to Tanner's analytical solutions [93]. The SAOS behaviour also showed good agreement with similar simulations performed by Chinesta [22]. The results are compared with analytical equations of Rouse chain where the storage modulus shows good agreement except at low frequencies ($\omega = 0.1 \text{ rad s}^{-1}$). At low frequencies, the signal is weak and can be strengthened by running the simulation for longer times. Unfortunately, the supercomputing service limits simulation runtime to 3 days. It is probable that running the simulations for 3-4 weeks will result in accurate storage modulus values in those regions. The Lissajous curves constructed from simulation data show high noise values at $\omega = 0.1 \text{ rad s}^{-1}$. The same issue affects the loss modulus at low frequencies. The loss modulus is also affected at higher frequencies ($> 8 \text{ rad s}^{-1}$) because the algorithm cannot resolve itself as loss modulus decays rapidly to 0 with increasing frequency. The present work also superimposes a steady shear on small amplitude oscillations in the parallel direction to simulate PSR experiments. Herein, the signal was found to be weak using a total time of 200 s. The simulated Lissajous curves show large discrepancies from the analytical curves at low frequencies. Increasing the total time to generate stronger signals was found to reduce the noise in the curves, however they differ from the expected results. In conclusion, probing the dynamics of the appearance of negative G''_{\parallel} at low frequencies requires adequate signal to noise ratio which was inaccessible during the course of this study. Recommendations for further work include

developing more accurate algorithms and gaining access to hundreds of processing units which will significantly reduce simulation time hence generating stronger signals at low frequencies.

Appendix A

Chapter 4: Appendix

The determination of the pseudo-LVR for 4.1wt% CPyCl Solution

The experimental limitations can be identified by drawing boundary lines with the coordinate axes used to report material functions [31]. The viscoelastic moduli as a function of strain amplitude, for which the low-torque limit sets the minimum measurable viscoelastic moduli is:

$$G_{min} = \frac{F_t T_{min}}{\gamma_0} \quad (\text{A.1})$$

The stress constant (F_t) is obtained from ARES-G2 instrument specifications as 7463.55 $Pa/N.m$. The minimum torque (T_{min}) is often specified by instrument manufacturers but can be higher in materials like dilute polymers in aqueous solutions. In this case, the minimum torque was selected by careful analysis of the experimental amplitude and frequency sweeps. The strain amplitude (γ_0) is 4%. In Fig A.1 and Fig A.2, the amplitude sweeps are subjected to steady shear flows in the parallel direction. As expected, the storage modulus increases with increasing frequency. It is observed that measurements become increasingly erratic as the shear rate is increased especially at low frequencies. This is because increasing shear rate suppresses the oscillatory wave decreasing the signal to noise ratio (high noise). These experimental boundaries (red dashed line) defined by Eqn A.1 help identify the region of acceptable data.

In Fig A.3 and Fig A.4, the frequency sweeps at different strains under PSR flows are described. Using a strain amplitude (γ_0) of 4%, the experimental boundaries defined by Eqn A.1 are constructed. For 0, 0.1, 0.4 s^{-1} (Fig A.3), the strains are independent of frequency and shear rate but at low frequencies (around 0.1 $rad\ s^{-1}$), some noise is observed. For 1, 4, 10 s^{-1} (A.4), the strains are highly dependent on frequencies below 1 $rad\ s^{-1}$ (high noise). There is erratic behaviour due to the steady shear suppressing the oscillatory wave. It is clear that at low frequencies ($\omega < 0.4\ rad\ s^{-1}$) and high shear rates ($\dot{\gamma} > 1\ s^{-1}$), the oscillatory signal is significantly weaker than the steady shear, hence, the minimum torque (T_{min}) required to obtain valid data increases as shear rate ($\dot{\gamma}$) increases as observed in Fig, A.5.

In Fig A.6 and Fig A.7, the orthogonal amplitude sweeps for 0.1, 1, 10 and 40 $rad\ s^{-1}$ are subject to varying levels of steady shear. The highest frequency was limited to 40 $rad\ s^{-1}$ due to instrument limitations. As expected, the storage modulus increases as frequency is increased. At 0.1 $rad\ s^{-1}$, the erratic nature of the data is present at all shear rates. The region of acceptable data is denoted by the red dashed line calculated from Eqn A.1 where the stress constant (F_{min}) is obtain from instrument specifications as 92.1256 $Pa/N.m$ and $\gamma_0 = 4\%$. The weak signal at low frequencies means the data should be treated as artefacts not be trusted. In Fig A.8 and Fig A.9, the orthogonal frequency sweeps for different strains are subjected to varying levels of shear rate ($\dot{\gamma}$). The instrument limitations require that the maximum stain that can be applied orthogonally is $\gamma_0 = 5\%$. At $\omega > 0.1\ rad\ s^{-1}$, the storage and loss modulus are independent of applied strain until $\omega > 40\ rad\ s^{-1}$ where data becomes erratic and strain becomes frequency dependent. The low torque limit boundary (red dashed line) is identified via Eqn A.1. Below this region, the oscillatory signal is weaker than the steady shear. It is important to note that the noisiness of the OSR pseudo linear region is considerably less than that of its PSR counterpart because it has been established that Orthogonal Superposition Rheometry is analogous to Small Amplitude Oscillatory Shear because the steady shear and SAOS are applied in different directions i.e. there is no coupling of forces. In Fig A.10, the minimum torque (T_{min}) increases as shear rate ($\dot{\gamma}$) increases. The criteria for a region of acceptable data is simply when measured torque is greater than the minimum

torque, $T > T_{min}$. The conclusions from investigating the pseudo-LVR of a shear thinning 4.1 wt% *CPyCl* solution also applies to a shear banding 5.9 wt% *CPyCl* solution.

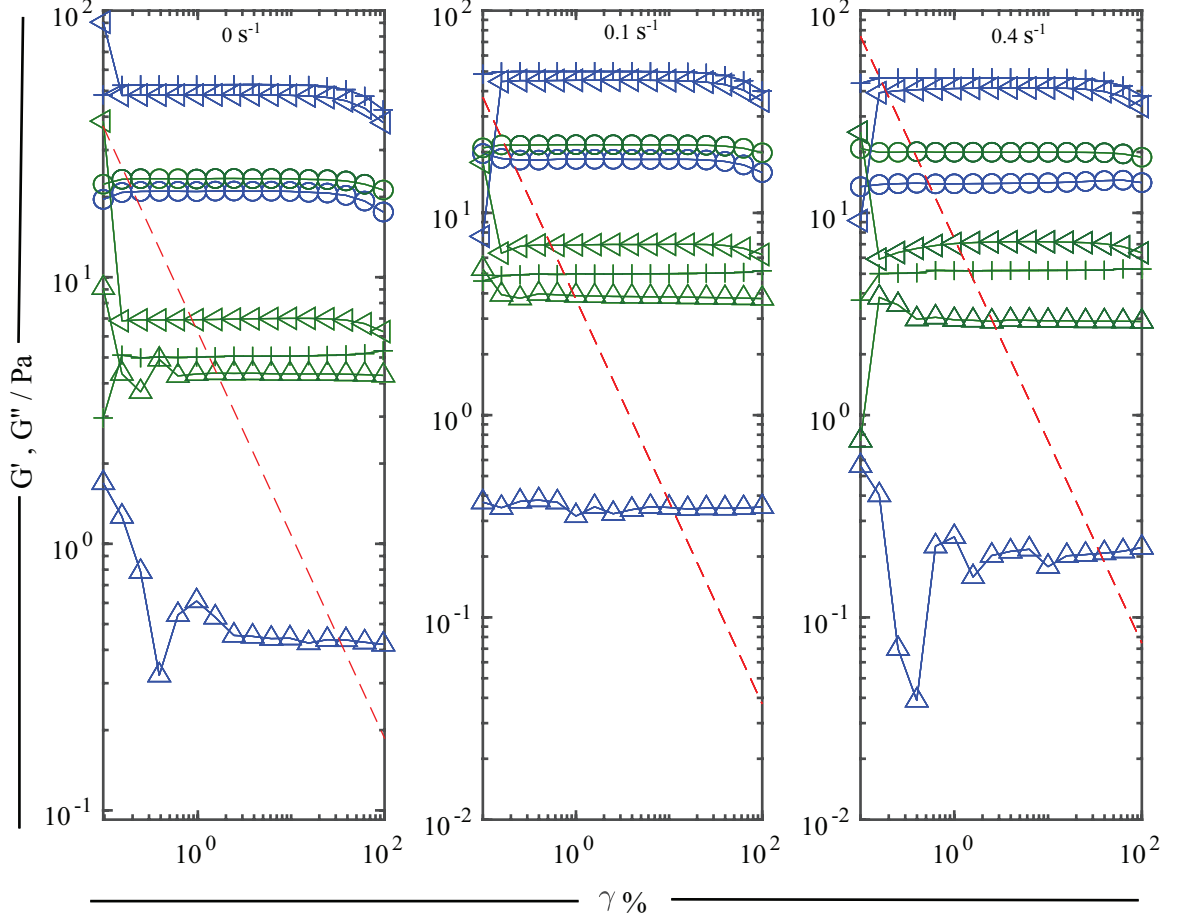


Figure A.1: The determination of the PSR pseudo-linear viscoelastic range for 4.1wt% *CPyCl* at 0.1(Δ), 1(\circ), 10(\triangleleft), 100($+$) $rad\ s^{-1}$ at 0, 0.1, 0.4 s^{-1} respectively. The blue shapes are storage moduli (G'_{\parallel}) and the green shapes are the loss moduli (G''_{\parallel}). The low-torque limit effects (red dashed) line is calculated from Eqn A.1.

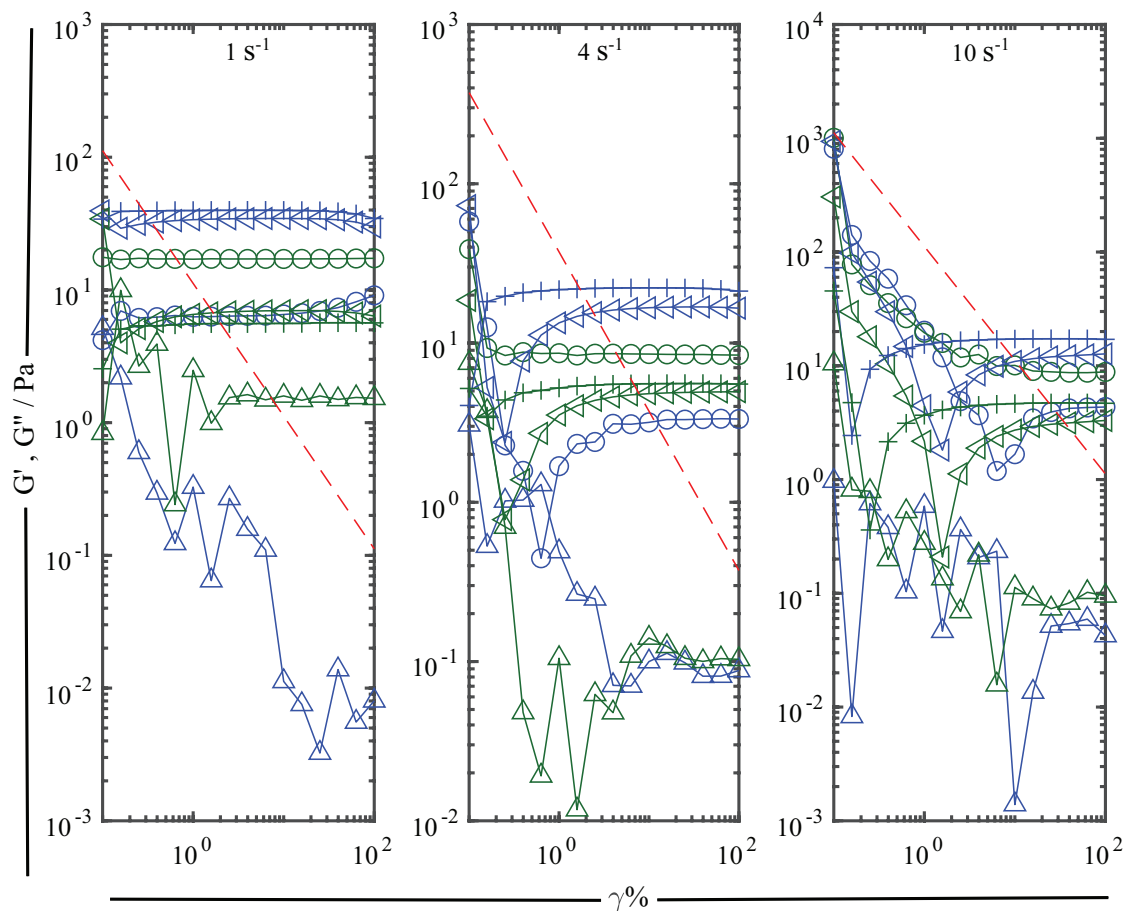


Figure A.2: The determination of the PSR pseudo-linear viscoelastic range for 4.1wt% *CPyCl* at 0.1(Δ), 1(\circ), 10(\triangleleft), 100($+$) rad s^{-1} at 1, 4, 10 s^{-1} respectively. The blue shapes are storage moduli (G'_{\parallel}) and the green shapes are the loss moduli (G''_{\parallel}). The low-torque limit effects (red dashed) line is calculated from Eqn A.1.

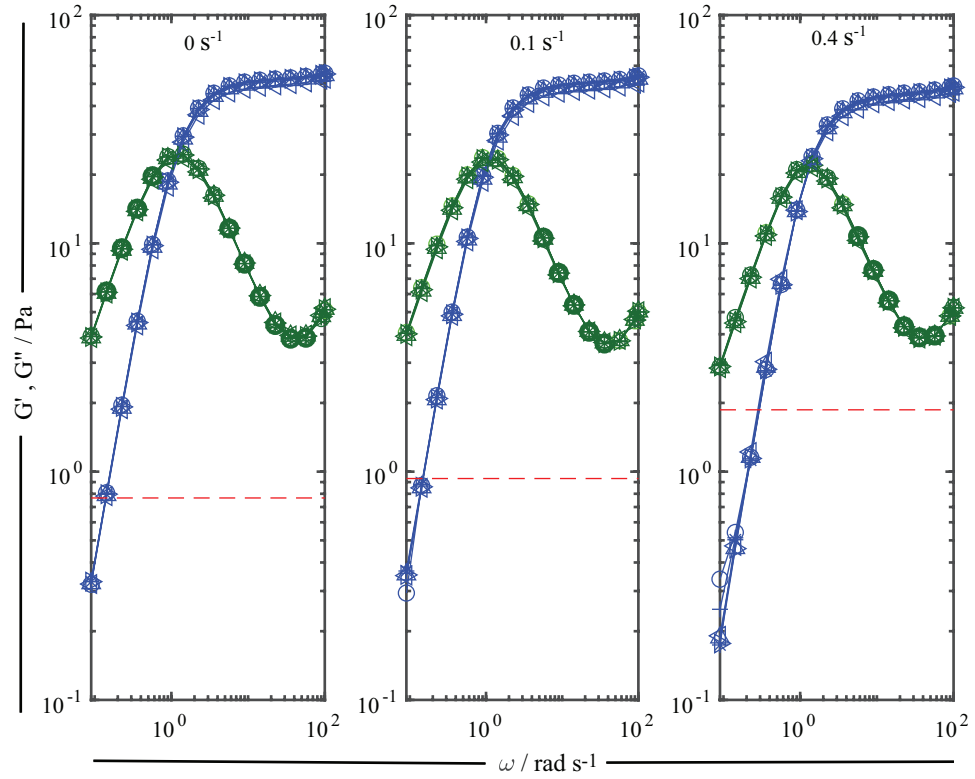


Figure A.3: The frequency sweeps of 4.1wt% *CPyCl* at 0, 0.1, 0.4 s^{-1} respectively using strains of 1, 2, 4, 10, 20, 40%. The blue shapes are storage moduli (G'_{\parallel}) and the green shapes are the loss moduli (G''_{\parallel}). The low-torque limit effects (red dashed) line is calculated from Eqn A.1.

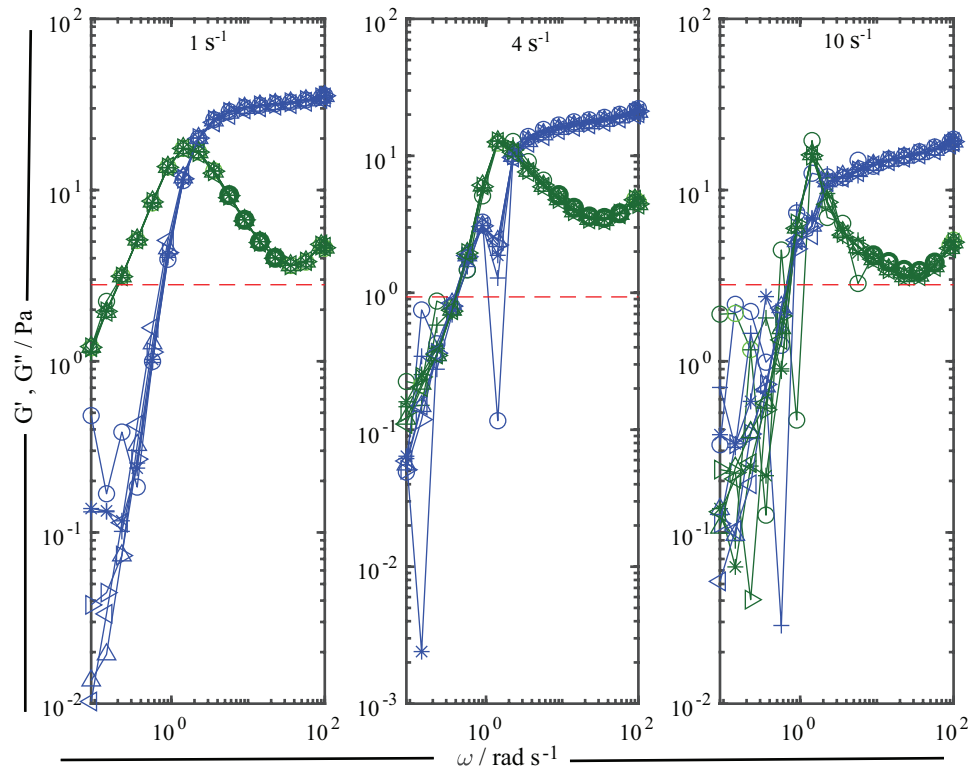


Figure A.4: The frequency sweeps of 4.1wt% *CPyCl* at 1, 4, 10 s^{-1} respectively using strains of 1, 2, 4, 10, 20, 40%. The blue shapes are storage moduli (G'_{\parallel}) and the green shapes are the loss moduli (G''_{\parallel}). The low-torque limit effects (red dashed) line is calculated from Eqn A.1.

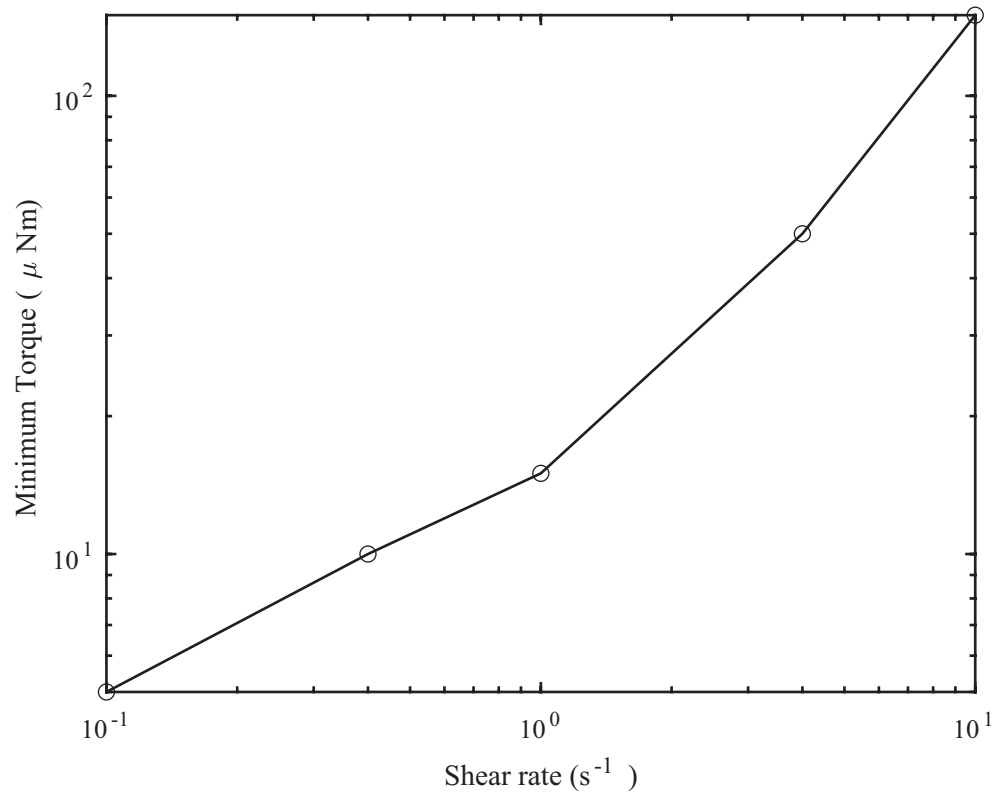


Figure A.5: The variation of the minimum torque (T_{min}) with shearrate ($\dot{\gamma}$) for PSR.

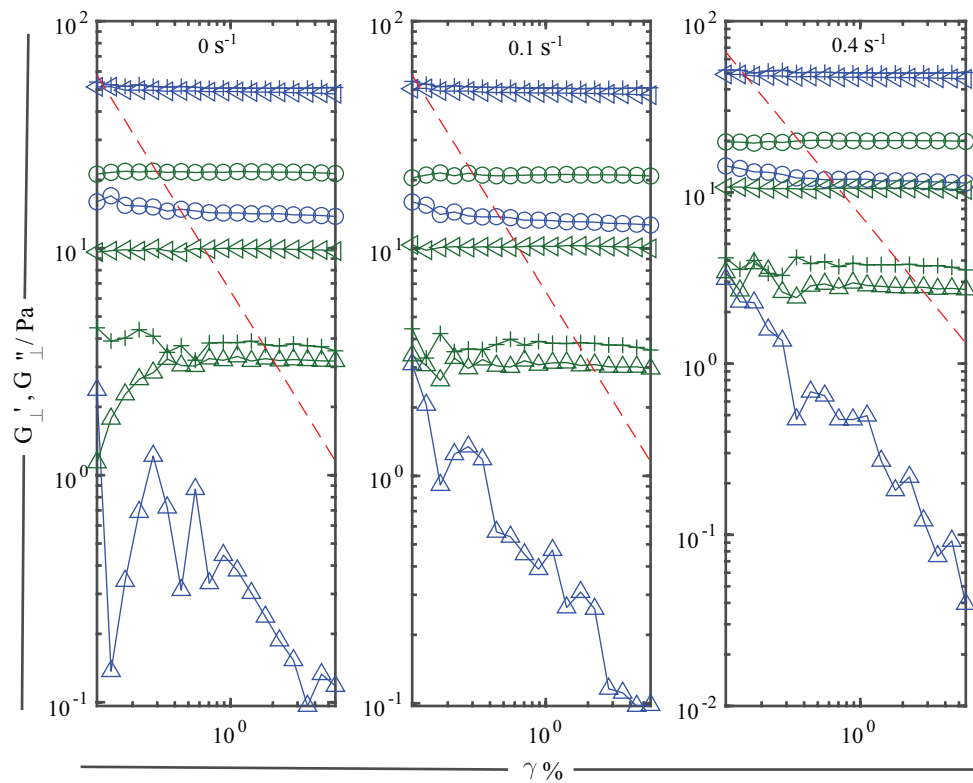


Figure A.6: The determination of the OSR pseudo-linear viscoelastic range for 4.1wt% *CPyCl* at 0.1(Δ), 1(\circ), 10(\diamond), 40($+$) rad s^{-1} at 0, 0.1, 0.4 s^{-1} respectively. The blue shapes are storage moduli (G'_{\perp}) and the green shapes are the loss moduli (G''_{\perp}). The low-torque limit effects (red dashed) line is calculated from Eqn A.1.

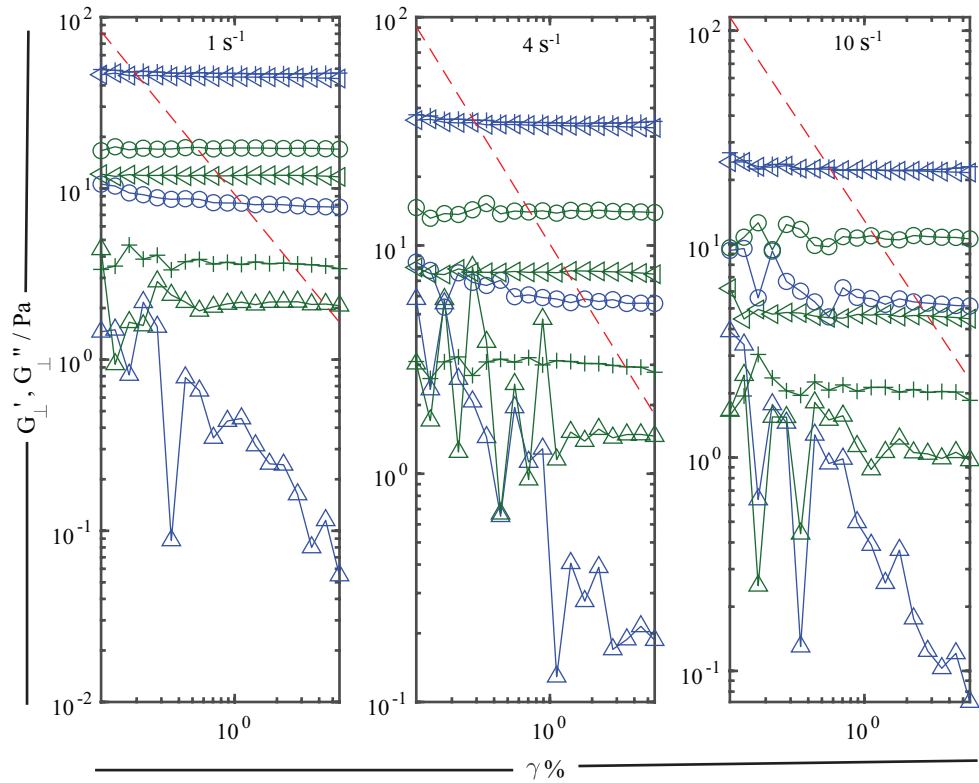


Figure A.7: The determination of the OSR pseudo-linear viscoelastic range for 4.1wt% *CPyCl* at 0.1(Δ), 1(\circ), 10(\triangleleft), 40($+$) rad s^{-1} at 1, 4, 10 s^{-1} respectively. The blue shapes are storage moduli (G'_{\perp}) and the Green shapes are the loss moduli (G''_{\perp}). The low-torque limit effects (red dashed) line is calculated from Eqn A.1.

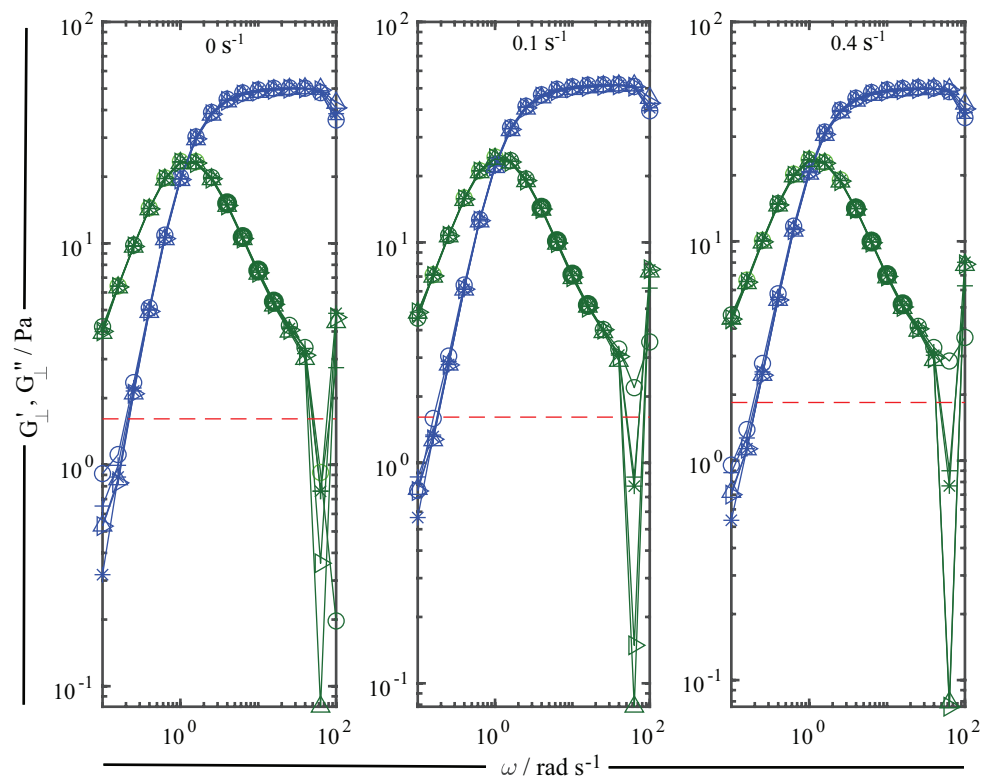


Figure A.8: The orthogonal superposition frequency sweeps of 4.1wt% *CPyCl* at 0, 0.1, 0.4 s^{-1} respectively using strains of 1,2,3,4,5 %. The blue shapes are storage moduli (G'_{\perp}) and the green shapes are the loss moduli (G''_{\perp}). The low-torque limit effects (red dashed) line is calculated from Eqn A.1.

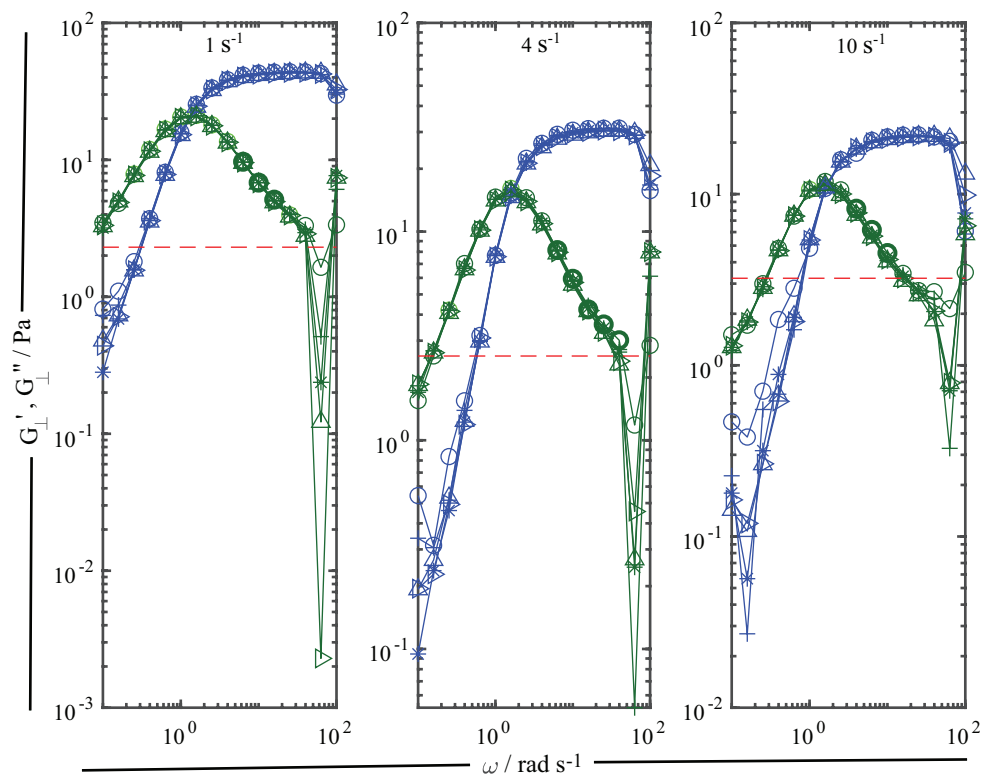


Figure A.9: The orthogonal superposition frequency sweeps of 4.1wt% *CPyCl* at 1, 4, 10 s⁻¹ respectively using strains of 1,2,3,4,5 %. The blue shapes are storage moduli (G'_{\perp}) and the green shapes are the loss moduli (G''_{\perp}). The low-torque limit effects (red dashed) line is calculated from Eqn A.1.

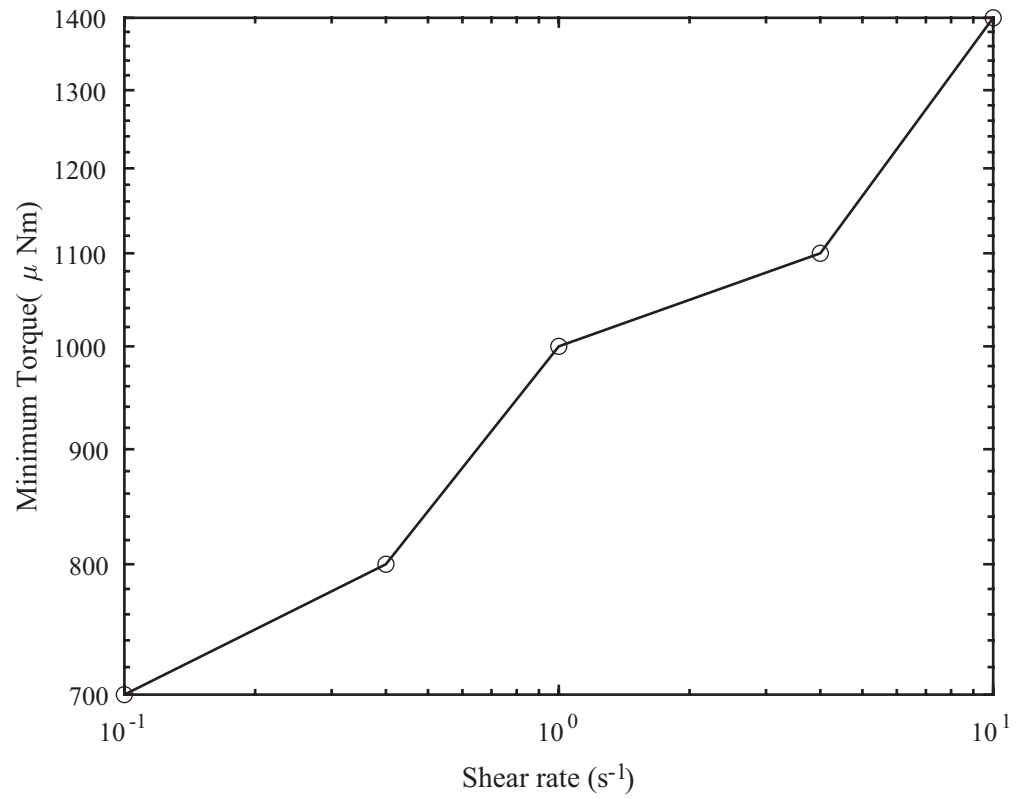


Figure A.10: The variation of the minimum torque (T_{min}) with shearrate ($\dot{\gamma}$) for OSR.

The Giesekeus Model for PSR & OSR

```
function [R L2] = Giesekeus(G, lambda, alpha, Gsaos, rate, eta_s, w)
```

```
De = lambda.*rate
```

```
L2 = (1/(8*alpha*(1-alpha)*De^2))*(sqrt(1 + 16*alpha*(1-alpha)*De^2)-1)
```

```
LAM = sqrt(L2) ;
```

```
N2 = G.*(1-LAM)./(1+(1-2*alpha)*LAM) ;
```

```
N1 = 2*N2*(G-alpha.*N2)/(alpha*(G-N2)) ;
```

```
sigma = De*(G-N2)^2/(G+(1-2*alpha)*N2) ;
```

```
n1 = N1./G ; n2 = N2./G ;
```

```
a = 1 + alpha*n1-alpha*n2 ;
```

```
b = alpha.*(sigma/G)*(De - alpha*(sigma/G)) ;
```

```
A = 1 - n2 ;
```

```
z = (1 - alpha.*n2)
```

```
asg = alpha.*(sigma/G).^2 ;
```

```
B = A*(2*a^2-b)-asg*(2+alpha*n1-2*alpha*n2) ;
```

```
C = A*(a^4 -(a^2)*b)-asg*(a^3+z*a^2) ;
```

```
D = z^2+2*(a^2-b) ;
```

```
E = 2*z*(z*a^2+a*b)+(a^2-b)^2 ;
```

```
F = ( z*a^2 + a*b).^2 ;
```

```
H = A*z + asg ;
```

```
I = A*(2*z*a^2+a*b)-asg*(z*a-a^2+b) ;
```

```
J = A*(z*a^4 + a^3*b)-asg*(z*a^3+a^2*b) ;
```

$$X = \text{lambda}.*w ;$$

$$\begin{aligned} Gp_o &= G.*(A.*X.^6 + B.*X.^4 + C.*X.^2)./(X.^6 + D.*X.^4 + E.*X.^2 + F) ; \\ Gpp_o &= G.*(H.*X.^5 + I.*X.^3 + J.*X)./(X.^6 + D.*X.^4 + E.*X.^2 + F) \\ &+ \text{eta}_s.*w ; \end{aligned}$$

$$\begin{aligned} c &= 1 + 2*\alpha*(n1-n2) ; \\ d &= (\alpha.*\text{sigma}/G) - D_e \\ e &= 1 - 2*\alpha*n2 ; \\ f &= 1 + \alpha*(n1-2*n2) ; \\ h &= 1 - n2 ; \end{aligned}$$

$$K = A ;$$

$$L = c*c*h + h*e*e - 2*(c+f)*\text{asg} + 4*d*h*\alpha*\text{sigma}/G ;$$

$$\begin{aligned} M &= c*c*e*e*h + 4*d*e*\alpha*\alpha*((\text{sigma}/G).^3) \\ &- 4*c*d*\alpha*\alpha*((\text{sigma}/G).^3) \\ &- 2*c*e*e*\alpha*((\text{sigma}/G).^2) - 2*e*e*f*\alpha*((\text{sigma}/G).^2) \\ &+ 2*d*e*e*h*\alpha*(\text{sigma}/G) + 2*c*c*d*h*\alpha*(\text{sigma}/G); \end{aligned}$$

$$N = c*c + e*e + f*f + 4*d*\alpha*\text{sigma}/G ;$$

$$O = c*c*f*f + c*c*e*e + e*e*f*f + 4*(c*c - e*f)*d*\alpha*\text{sigma}/G ;$$

$$P = c*c*e*e*f*f + 4*(c*c - e*e)*d*d*\alpha*\text{asg} - 4*c*c*d*e*f*\alpha*\text{sigma}/G ;$$

$$Q = f*h + 2*\alpha*((\text{sigma}/G).^2) ;$$

$$R = c*c*f*h + e*e*f*h + 2*(e*e - c*f)*\text{asg}$$

```
+ 2*(c-e)*d*h*alpha*sigma/G ;
```

```
S = c*c*e*e*f*h - 4*d*e*e*alpha*alpha*((sigma/G).^3)  
+ 4*c*d*e*alpha*alpha*((sigma/G).^3)  
- 2*c*e*e*f*alpha*((sigma/G).^2) + 2*c*d*e*e*h*alpha*(sigma/G)  
-2*c*c*d*e*h*alpha*(sigma/G);
```

```
Gp_11 = G.*(K.*X.^6 + L.*X.^4 + M.*X.^2)./(X.^6 + N.*X.^4 + O.*X.^2 + P) ;  
Gpp_11 = G.*(Q.*X.^5 + R.*X.^3 + S.*X)./(X.^6 + N.*X.^4 + O.*X.^2 + P)  
+ eta_s.*w ;
```

```
R = [w' Gp_o' Gpp_o' Gp_11' Gpp_11']
```

Appendix B

Chapter 5: Appendix

The Determination of Peak Stresses (σ_0) from the LVR of 4.1wt% *CPyCl* Solution

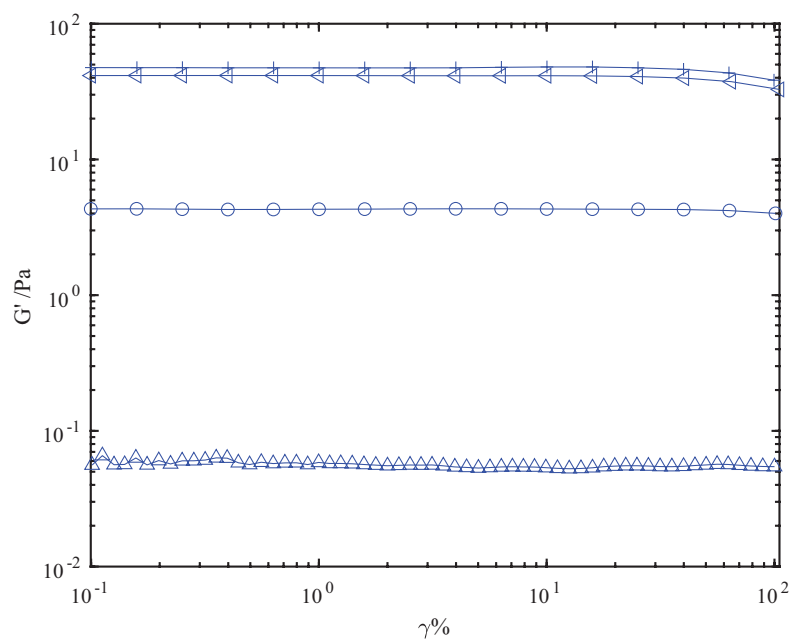


Figure B.1: The determination of the LVR for 4.1wt% *CPyCl* at 0.1(Δ), 1(\circ), 10(\triangleleft), 100(+) $rad\ s^{-1}$.

In Fig B.1, the linear viscoelastic region of a 4.1%wt *CPyCl* solution is determined via amplitude sweeps using a Combined Motor Transducer (CMT), Dual head Rheometer (DHR-30) from TA instruments. As expected, the storage modulus increases as shear rate is increased. The LVR is the region where the storage modulus is independent of applied strain. The corresponding peak stresses, σ_0 at these LVR strains are used to generate experimental transient data from the DHR-30 and calculate numerical transient data using the methods described in section 5.2. These selected values are shown in the table below:

ω ($rad\ s^{-1}$)	σ_0 (Pa)
0.1	0.11
1	0.51
10	1.65
100	1.84

Appendix C

Chapter 6: Appendix

Derivation of the moduli from a tilted ellipse

The sinusoidal strain can be defined as:

$$\gamma = \gamma_0 \sin(\omega\tau) \quad (\text{C.1})$$

The stress can be defined as:

$$\sigma = \gamma_0 G' \sin(\omega t) + \gamma_0 G'' \cos(\omega t) \quad (\text{C.2})$$

From Eqn C.1, it follows that:

$$\sin(\omega t) = \frac{\gamma}{\gamma_0} \quad (\text{C.3})$$

The relevant trigonometric identity is :

$$\cos(\omega t) = \sqrt{1 - \sin^2(\omega t)} \quad (\text{C.4})$$

By substituting Eqn C.3 and Eqn C.4 into Eqn C.2, the following expression can be obtained:

$$\sigma = \gamma_0 G' \frac{\gamma}{\gamma_0} + \gamma_0 G'' \sqrt{1 - \left(\frac{\gamma}{\gamma_0}\right)^2} \quad (\text{C.5})$$

$$\sigma - G'\gamma = \gamma_0 G'' \sqrt{1 - \left(\frac{\gamma}{\gamma_0}\right)^2} \quad (\text{C.6})$$

$$\frac{\sigma}{\gamma_0 G''} - \frac{G'\gamma}{\gamma_0 G''} = \sqrt{1 - \left(\frac{\gamma}{\gamma_0}\right)^2} \quad (\text{C.7})$$

$$\left(\frac{\sigma}{\gamma_0 G''} - \frac{G'\gamma}{\gamma_0 G''}\right)^2 = 1 - \left(\frac{\gamma}{\gamma_0}\right)^2 \quad (\text{C.8})$$

$$\frac{\sigma^2}{\gamma_0^2 G''^2} - \frac{2\sigma\gamma G'}{\gamma_0^2 G''^2} + \frac{G'^2 \gamma^2}{\gamma_0^2 G''^2} = 1 - \left(\frac{\gamma}{\gamma_0}\right)^2 \quad (\text{C.9})$$

Multiplying Eqn C.9 by $\gamma_0^2 G''^2$, the following expression is obtained:

$$\sigma^2 - 2\sigma\gamma G' + G'^2 \gamma^2 + \gamma^2 G''^2 = \gamma_0^2 G''^2 \quad (\text{C.10})$$

$$\sigma^2 - 2\sigma\gamma G' + (G'^2 + G''^2)\gamma^2 = \gamma_0^2 G''^2 \quad (\text{C.11})$$

Dividing Eqn C.11 by $\gamma_0^2 G''^2$, the following expression can be obtained:

$$\frac{\sigma^2}{\gamma_0^2 G''^2} - \frac{2G'\sigma\gamma}{\gamma_0^2 G''^2} + \frac{G'^2 + G''^2}{\gamma_0^2 G''^2} \gamma^2 = 1 \quad (\text{C.12})$$

The equation of the ellipse is given as:

$$a\sigma^2 + b\sigma\gamma + c\gamma^2 = 1 \quad (\text{C.13})$$

where:

$$a = \frac{1}{\gamma_0^2 G''^2} \quad (\text{C.14})$$

$$b = \frac{-2G'}{\gamma_0^2 G''^2} \quad (\text{C.15})$$

$$c = \frac{G'^2 + G''^2}{\gamma_0^2 G''^2} \quad (\text{C.16})$$

such that:

$$G'' = \sqrt{\frac{1}{a\gamma_0^2}} \quad (\text{C.17})$$

$$G' = \frac{-b\gamma_0^2 G''^2}{2} \quad (\text{C.18})$$

Description of MATLAB code for creating Brownian Dynamic Simulations

`% Variables`

`Wi = 10; % the Weissenberg number is the product of the longest relaxation time and the shear rate (Peclet).`

`N = 7 ; % Number of beads.`

`Ns = N-1; % Number of Springs.`

`b = 1000; % extensibility parameter.`

`lambdaH = 1 ; % Non-dimensionalized relaxation time of a Hookean Dumbbell.`

`tot_time = 5000 ; % The total time of the BD simulation.`

`eq_time = 100 ; % The equilibration time allowed before flow is imposed.`

`flow_type = 'shr'; % 'ext = extensional flow' or 'shr = shear flow'`

`L = 0.5 ;`

`dt = 0.01 ; % Initial Timestep.`

`D = 3 ;`

```

freqrange = logspace(-1,1,10); % The frequency range in Hertz.
osc_freq = 2*pi*freqrange(1); % The frequency in Radians.
osc_amp = 0.1; % Oscillation Amplitude.
psr = 1; % This turns on parallel superposition.

Peclet = 10 ; % The dimensionless Shear rate (Peclet) is
the ratio of the Weissenberg number
to the dimensionless relaxation time.

roothalf = sqrt(0.5) ;

Nsteps = tot_time/dt ; % Number of Steps.
Neq = eq_time/dt ; % Number of Equilibration Steps.

t = dt: dt:tot_time ; % The time vector starts from
the chosen timestep to the totaltime in intervals of the timestep.

strain = zeros(size(t)) ; strain(Neq:end) = Peclet.*(t(Neq:end)-t(Neq)) ;
% The strain is defined as a product of Peclet
and time after equilibration.

R2eq = 3*(b*Ns+3)/b;
% The Equilibrium end to end distance
for a Bead Spring Chain. (see section 5.1.7)

S12 = zeros(Nsteps, Nchains) ;
% A matrix that stores the 1-2 component of the stress tensor.

EE = S12 ; %A matrix that stores the End-to-End distance of a polymer chain.

```

```

parpool(35) % This allows access to 35 CPU cores of SUPERCOMPUTINGWALES.

parfor c = 1 : Nchains
% A parallel For-Loop that cycles through each individual chain.
% Generate initial chain configuration.
[x , Q] = BD_Init_Config(N,L,D,0) ;
X0 = x - mean(x);
% This allows the center of the chain to be at the origin
BD_Plot(X0,1, plotlim);
F = FENE(Q, b) ; % A function that uses the connector vector, Q
and extensibility parameter, b to generate
the dimensionless vector of spring force on a FENE dumbbell.
see Eqn 5.43

% Generate random Brownian force.
Q2 = zeros(size(Q)) ;
F2 = Q2 ;
Fbar = Q2 ;
Qbar = Q2 ;

for ii = 1 : Nsteps % A ForLoop that cycles through the number of steps.

if ii > Neq ; flow = 1; else flow = 0; end
% The variable flow switches on the flow after equilibration.

ratetensor = flow.*(Peclet+osc_amp*osc_freq*cos(osc_freq*((ii-Neq)*dt)))
*(psr.*[0 1 0; 0 0 0; 0 0 0] + osr.*[0 0 1; 0 0 0; 0 0 0]);
% This defines the instantaneous rate tensor which for PSR
involves the steady component and oscillatory components.
If flow is equal to zero, the rate tensor is zero.

```

```

W = normrnd(0,sqrt(dt),N,D) ; .
% generates an array of normal random numbers,
N and D indicates the size of each dimension and
standard deviation of squareroot of dt and
a mean value of zero.

W = diff(W); % The differentiation of W.

% The integration scheme (see section 5.1.6)

Qs = zeros(size(Q)) ;
for jj = 1 : N-1 % cycle through the number of springs
    if jj == 1
        Qs(jj,:) = Q(jj,:) + dt.*( (flow*ratetensor*Q(jj,:))' )'
        + 0.25*( -2*F(jj,:) + F(jj+1,:) ) ) + roothalf*W(jj,:) ;
    elseif jj == N-1
        Qs(jj,:) = Q(jj,:) + dt.*( (flow*ratetensor*Q(jj,:))' )'
        + 0.25*( F(jj-1,:) -2*F(jj,:) ) ) + roothalf*W(jj,:) ;
    else
        Qs(jj,:) = Q(jj,:) + dt.*( (flow*ratetensor*Q(jj,:))' )'
        + 0.25*( F(jj-1,:) -2*F(jj,:) + F(jj+1,:) ) )
        + roothalf*W(jj,:);
    end
end

% Corrector 1
R = zeros(size(Q)) ;
for jj = 1 : N-1
    if jj == 1
        R(jj,:) = Q(jj,:) + dt*(0.5*( (flow*ratetensor*Q(jj,:))' )'
        + (flow*ratetensor*Qs(jj,:))' )' )
    end
end

```

```

+ 0.25*F(jj+1,:)) + roothalf*W(jj,:) ;
Qbar(jj,:) = Qbar_from_R(R(jj,:),b, dt) ;
Fbar(jj,:) = FENE(Qbar(jj,:), b) ;

elseif jj == N-1
R(jj,:) = Q(jj,:) + dt*(0.5*( (flow*ratetensor*Q(jj,:))' )'
+ (flow*ratetensor*Qs(jj,:))' )' ) + 0.25*Fbar(jj-1,:))
+ roothalf*W(jj,:) ;
Qbar(jj,:) = Qbar_from_R(R(jj,:),b, dt) ;
Fbar(jj,:) = FENE(Qbar(jj,:), b) ;

else
R(jj,:) = Q(jj,:) + dt*(0.5*( (flow*ratetensor*Q(jj,:))' )'
+ (flow*ratetensor*Qs(jj,:))' )' ) + 0.25*( Fbar(jj-1,:)
+ F(jj+1,:) ) ) + roothalf*W(jj,:) ;
Qbar(jj,:) = Qbar_from_R(R(jj,:),b, dt) ;
Fbar(jj,:) = FENE(Qbar(jj,:), b) ;
end
end

% Corrector 2
accept = 0 ;
%Q2(jj,:) = [NaN NaN NaN];
while accept == 0
R = zeros(size(Q)) ;
for jj = 1 : N-1
if jj == 1
R(jj,:) = Q(jj,:) + dt*(0.5*( (flow*ratetensor*Q(jj,:))' )'
+ (flow*ratetensor*Qbar(jj,:))' )' )
+ 0.25*Fbar(jj+1,:)) + roothalf*W(jj,:) ;

```

```

    Q2(jj,:) = Qbar_from_R(R(jj,:),b, dt) ;
    F2(jj,:) = FENE(Q2(jj,:), b) ;

elseif jj == N-1
    R(jj,:) = Q(jj,:) + dt*(0.5*( (flow*ratetensor*Q(jj,:))' )'
    + (flow*ratetensor*Qbar(jj,:))' )'
    + 0.25*F2(jj-1,:)) + roothalf*W(jj,:) ;

    Q2(jj,:) = Qbar_from_R(R(jj,:),b, dt) ;
    F2(jj,:) = FENE(Q2(jj,:), b) ;

else
    R(jj,:) = Q(jj,:) + dt*(0.5*( (flow*ratetensor*Q(jj,:))' )'
    + (flow*ratetensor*Qbar(jj,:))' )' + 0.25*( F2(jj-1,:)
    + Fbar(jj+1,:) ) ) + roothalf*W(jj,:) ;

    Q2(jj,:) = Qbar_from_R(R(jj,:),b, dt) ;
    F2(jj,:) = FENE(Q2(jj,:), b) ;

end

end

dQ = Q2 - Qbar ;
err = sqrt(sum(dot(dQ,dQ,2))) ;
% This is the residual between Q2 and Qbar.
if err < 1E-6
% If the residual is less than a specified tolerance,
Q2 and F2 are accepted as the correct
Connector vector and Spring force.
    Q = Q2 ;

```

```

        F = F2 ;
        accept = 1;
    else
        Qbar = Q2 ;
        Fbar = F2 ;
        % If the residual is greater than the specified tolerance,
        % Q2 and F2 replace Qbar and Fbar and corrector 2 is
        % repeated until convergence.
    end
end
end

X = [zeros(1,D); cumsum(Q)];
X = X - mean(X);
if doplot == 1
    BD_Plot(X,1, plotlim);
    t(ii)
    pause(0.001)
end
stress = zeros(3,3) ;
for jj = 1 : N-1
    stress = stress + Q(jj,:)'*F(jj,:); % This is the polymeric stress
    derived from the accepted Q and F variables.
end

if flow_type == 'shr'
    S12(ii,c) = stress(1,2) ; % This is the shear stress.
    S31(ii,c) = stress(3,1) ;
    EE(ii,c) = norm(sum(Q))^2 ;
else
    S(ii,c) = stress(1,1) - stress(2,2);
end

```

```

        EE(ii,c) = norm(sum(Q))^2 ;
        % This is the end-to-end vector of the polymer chain.
    end

figure(50)
plot(t,mean(EE,2),'-k') % Plot the simulated End-to-End vector against time.
hold on
plot([min(t) max(t)],[R2eq R2eq],'--r', 'linewidth',2) % Plot the equilibrium
End-to-End distance for a Bead-Spring Chain for a Hookean dumbbell.
xlabel('Time')
ylabel('<r^2>')
legend('Simulation','Prediction')

tyme = dt:dt:tot_time ; %the time vector.
tyme = (tyme-eq_time)./lambdaH; %A dimensionless time vector.
vis = mean(S12,2)./(Peclet) ;
%The unsteady state viscosity as stress divided by shear rate.

figure(2000)
plot(tyme', vis, '-b')
axis([0 20 0 12]) % A plot of Viscosity against time.

stress = mean(S12,2) ;

for w2 = osc_freq %Oscillation Frequency in radians.

lambda = 2./(4* sin((1:(n-1))*pi/(2*n)).^2)
%The relaxation time for Rouse chain. see section 5.1.6

```



```

lambda_w = lambda.*w2

Gpm = sum( (lambda.^2 * w2.^2) ./ (1 + lambda_w.^2))
%The Storage modulus for a Rouse Chain.
Gppm = sum( lambda_w ./ (1 + lambda_w.^2))
% The loss modulus for a Rouse Chain.
end

ndx7 = t >=120 ;
tt = t(ndx7) ;
% The relevant times are greater than or equal to 120 seconds.
This is after steady state has been reached.

yy = strain(ndx7)' - Peclet*(tyme(ndx7)-dt*Neq)' ;
% Removal of the steady shear strain from the
% total strain to obtain the oscillatory strain.

xx = stress(ndx7) ; % The stress values for the relevant time.

tm1 = min(tt)
tm2 = tm1 + 2*pi/osc_freq %+ 0.05*dt
n_sig = 0
xx0 = 0
yy0 = 0
ee0 =0
ndx0 = tt > tm1 & tt <= tm2 ;

```

```

MEAN_S31_5000_0001 = mean(S31,2);
MEAN_S12_5000_0001 = mean(S12,2);
MEAN_EE_5000_0001 = mean(EE,2);
ee = MEAN_EE_5000_0001;

% Averaging waves to improve the signal to noise ratio.
while tm2 <= max(tt)

    if n_sig == 1

        xx0 = xx(ndx0);  yy0 = yy(ndx0);
        ee0 = ee(ndx0);
    else
        xx0 = xx0 + xx(ndx0);  yy0 =yy0 + yy(ndx0); ee0 = ee0 + ee(ndx0);
    end

    n_sig = n_sig + 1
    ndx1 = ndx0 ;
    tm2 = tm2 + 2*pi/osc_freq ;
    ndx0(max(find(ndx0))+1:max(find(ndx0))+sum(ndx0)) = 1 ;
    ndx0(ndx1) = 0 ;

end

xx = (xx0 - mean(xx0)) / n_sig ; yy = yy0 / n_sig ; ee = ee0 / n_sig ;

A = [xx.^2, xx.*yy, yy.^2]\ones(size(xx)) ;
% This extracts the major and minor axis of the Lissajous curves;

osc_amp = max(yy) ;

```

```

Gpp2 = sqrt( 1 / ( A(1).*(osc_amp^2) ) ) ;
Gp2 = -A(2).* ((Gpp2*osc_amp)^2) / 2 ;
(Gp2*Gp2 + Gpp2*Gpp2)/( (Gpp2*osc_amp)^2) ;
% This calculates the moduli from minor and major axis.

ss_exp = Gp2.*osc_amp*sin(osc_freq*(tt)) + Gpp2.*osc_amp*cos(osc_freq*(tt)) ;
%This calculates the fitted stress wave.

figure(20002)
plot(yy, xx, 'ob') ;
% Plot the simulated oscillatory strain versus stress.
hold on
plot(osc_amp*sin(osc_freq*tt), ss_exp, '-r', 'linewidth',3) ;
% Plot the fitted oscillatory strain versus stress.

```

Function to generate Initial chain configurations

```

function [x , Q] = BD_Init_Config(N,L,D,LVar)

% generate random unit vectors

R = rand(N,D) - 0.5;

% rand is a function that generates random numbers
between 0 and 1. 0.5 is subtracted from the result
to obtain vectors whose components can have
positive and negative directions.
% This generates the initial configuration of the polymer
(a random list of co-ordinates for each of the beads).
% D is the Number of dimensions for the random vectors.

```

```

% N is the Number of beads.

R = bsxfun(@rdivide,R,sqrt(sum(R.^2,2)));
% This function divides all the values
of R by the length of the vector to
obtain unit vectors.

if LVar~= 0
    LV = ones(N,1) + LVar*2*(rand(N,1)-0.5);
else
    LV = L*ones(N,1);
end
% This generates a list of lengths
for the vectors.

R = bsxfun(@times, R, LV);
% This function multiplies the
list of lengths(LV) and
Random directions(R)
to obtain position vectors.

x = [zeros(1,D); cumsum(R)];
% This is a list of position
vectors.

Q = R(1:end-1,:) ;
% The Connector vector, Q
is obtained from R.

```

Appendix D

Publications

The following paper has been submitted accepted for publications subject to minor revisions.

Full paper redacted (pages 174 - 184). Details of paper provided below.

The effect of instrument inertia on the initiation of oscillatory flow in stress controlled rheometry

Adeniyi Ogunkeye, Rebecca E. Hudson, and Daniel J. Curtis
*Complex Fluids Research Group, Department of Chemical Engineering, Faculty of Science and Engineering,
Swansea University Bay Campus, Fabian Way, Swansea SA1 8EN, UK*

(Dated: 16 March 2023)

In a recent paper [Hassager, J. Rheol. **64** (2020) 545-550], Hassager performed an analysis of the start up of stress-controlled oscillatory flow based on the general theory of linear viscoelasticity. The analysis provided a theoretical basis for exploring the establishment of a steady strain offset that is inherent to stress controlled oscillatory rheometric protocols. However, the analysis neglected the impact of instrument inertia on the establishment of the steady periodic response. The inclusion of the inertia term in the framework is important since it (i) gives rise to inertio-elastic ringing and (ii) introduces an additional phase shift in the periodic part of the response. Herein, we modify the expressions to include an appropriate inertial contribution and demonstrate that the presence of the additional terms can have a substantial impact on the time scale required to attain the steady state periodic response. The analysis is then applied to an aqueous solution of worm like micelles.

Library Research Support Team (05/09/2023)

Appendix E

Nomenclature

Symbol	Definitions	Units
σ	Shear stress	Pa
G	Elastic modulus	Pa
γ	Shear strain	-
$\dot{\gamma}$	Shear strainrate	s^{-1}
F	Force	N
μ	Newtonian viscosity	Pa.s
η	non-Newtonian viscosity	Pa.s
G'	Storage modulus	Pa
G''	Loss modulus	Pa
G^*	Complex modulus	Pa
t	Time	s
ω	Angular frequency	$rad\ s^{-1}$

M	Torque	N.m
r	Radius	m
t_{rep}	Reptation time	s
t_{br}, λ_{br}	Breaking and recombination time	s
t_R	Relaxation time	s
G'_{\perp}	Orthogonal storage modulus	Pa
G''_{\perp}	Orthogonal loss modulus	Pa
G'_{\parallel}	Parallel storage modulus	Pa
G''_{\parallel}	Parallel loss modulus	Pa
α	Dimensionless mobility parameter	-
δ_m	Raw phase	-
I	Inertia	$\mu Nm s^{-1}$
τ_p	Polymeric stress	Pa
Pe	Bead pecelet number	-
b	Dimensionless extensibility parameter	-
T	Temperature	$^{\circ}C$

Bibliography

- [1]
- [2] Supercomputing wales portal.
- [3] Vol. 49, rheometric series operators manual. 2007. 2007.
- [4] K Almdal, J Dyre, S Hvidt, and Ole Kramer. Towards a phenomenological definition of the term ‘gel’. *Polymer gels and networks*, 1(1):5–17, 1993.
- [5] Pierre Ballesta, M Paul Lettinga, and Sébastien Manneville. Superposition rheology of shear-banding wormlike micelles. *Journal of rheology*, 51(5):1047–1072, 2007.
- [6] Christophe Baravian, Ghania Benbelkacem, and François Caton. Unsteady rheometry: can we characterize weak gels with a controlled stress rheometer? *Rheologica Acta*, 46:577–581, 2007.
- [7] Howard A. Barnes. *A Handbook of Elementary Rheology*. University of Wales:Institute of Non-Newtonian Fluid Mechanics, 2000.
- [8] Howard A. Barnes, J. F. Hutton, and Kenneth Walters. An introduction to rheology. 1989.
- [9] Jean-François Berret. Transient rheology of wormlike micelles. *Langmuir*, 13:2227–2234, 1997.
- [10] Jean-François Berret, D. C. D. Roux, and Grégoire Porte. Isotropic-to-nematic transition in wormlike micelles under shear. *Journal De Physique Ii*, 4:1261–1279, 1994.

- [11] R. Byron Bird, Charles F. . Curtiss, Robert C. Armstrong, and Ole Hassager. Dynamics of polymeric liquids: Kinetic theory. 1987.
- [12] Gert Böhme and M. Stenger. On the influence of fluid inertia in oscillatory rheometry. *Journal of Rheology*, 34:415–424, 1990.
- [13] HC Booij. Influence of superimposed steady shear flow on the dynamic properties of non-newtonian fluids. *Rheologica Acta*, 7(3):202–209, 1968.
- [14] K. H. Jürgen Buschow. Encyclopedia of materials : science and technology. 2001.
- [15] ME Cates. Reptation of living polymers: dynamics of entangled polymers in the presence of reversible chain-scission reactions. *Macromolecules*, 20(9):2289–2296, 1987.
- [16] Michael E. Cates and Sauveur Jean Candau. Review article: Statics and dynamics of worm-like surfactant micelles. *Journal of Physics: Condensed Matter*, 1990.
- [17] Peng Cheng, Michael C Burroughs, L Gary Leal, and Matthew E Helgeson. Distinguishing shear banding from shear thinning in flows with a shear stress gradient. *Rheologica Acta*, 56(12):1007–1032, 2017.
- [18] Zonglin Chu, Cécile A Dreiss, and Yujun Feng. Smart wormlike micelles. *Chemical Society Reviews*, 42(17):7174–7203, 2013.
- [19] Nathan C. Crawford, Lauren B Popp, Katherine E. Johns, Lindsey M Caire, Brittany N. Peterson, and Matthew W. Liberatore. Shear thickening of corn starch suspensions: does concentration matter? *Journal of colloid and interface science*, 396:83–9, 2013.
- [20] Marcel J. Crochet and Kenneth Walters. Computational rheology: a new science. *Endeavour*, 17:64–77, 1993.
- [21] Rod Cross. Elastic and viscous properties of silly putty. *American Journal of Physics*, 80(10):870–875, 2012.

- [22] Camilo Cruz, Francisco Chinesta, and Gilles Regnier. Review on the brownian dynamics simulation of bead-rod-spring models encountered in computational rheology. *Archives of Computational Methods in Engineering*, 19(2):227–259, 2012.
- [23] D. J. Curtis and A. R. Davies. Volterra kernels, oldroyd models, and interconversion in superposition rheometry. *Journal of Non-Newtonian Fluid Mechanics*, 2021.
- [24] DJ Curtis and AR Davies. On response spectra and kramers-kronig relations in superposition rheometry. *Physics of Fluids*, 31(12):127105, 2019.
- [25] DJ Curtis and AR Davies. On shear-rate dependent relaxation spectra in superposition rheometry: A basis for quantitative comparison/interconversion of orthogonal and parallel superposition moduli. *Journal of Non-Newtonian Fluid Mechanics*, 274:104198, 2019.
- [26] Pierre Gilles de Gennes. Reptation of a polymer chain in the presence of fixed obstacles. *Journal of Chemical Physics*, 55:572–579, 1971.
- [27] Pierre Gilles de Gennes. Scaling concepts in polymer physics. 1979.
- [28] Jan KG Dhont and Norman J Wagner. Superposition rheology. *Physical Review E*, 63(2):021406, 2001.
- [29] Masao Doi and Sam F. Edwards. The theory of polymer dynamics. 1986.
- [30] Cécile A. Dreiss and Yujun Feng. Wormlike micelles: Advances in systems, characterisation and applications. *The Royal Society of Chemistry*, pages 31–62, 2017.
- [31] Randy H. Ewoldt, Michael T. Johnston, and Lucas Caretta. Experimental challenges of shear rheology: How to avoid bad data. 2015.
- [32] Randy H. Ewoldt and Gareth H. McKinley. 4 creep ringing in rheometry or how to deal with oft-discarded data in step stress tests ! 2007.
- [33] John D Ferry. *Viscoelastic properties of polymers*. John Wiley & Sons, 1980.

- [34] AJ Franck. Understanding instrument inertia corrections in oscillation. *TA Instrument*, 2005.
- [35] Michela Geri, Bavand Keshavarz, Thibaut Divoux, Christian Clasen, Daniel J Curtis, and Gareth H McKinley. Time-resolved mechanical spectroscopy of soft materials via optimally windowed chirps. *Physical Review X*, 8(4):041042, 2018.
- [36] Hanswalter Giesekus. A simple constitutive equation for polymer fluids based on the concept of deformation-dependent tensorial mobility. *Journal of Non-Newtonian Fluid Mechanics*, 11(1-2):69–109, 1982.
- [37] JD Goddard. Material instability in complex fluids. *Annual Review of Fluid Mechanics*, 35(1):113–133, 2003.
- [38] RJ Gordon and WR Schowalter. Anisotropic fluid theory: a different approach to the dumbbell theory of dilute polymer solutions. *Transactions of the Society of Rheology*, 16(1):79–97, 1972.
- [39] William W. Graessley. Polymeric liquids and networks : dynamics and rheology. 2008.
- [40] R Granek and ME Cates. Stress relaxation in living polymers: Results from a poisson renewal model. *The Journal of chemical physics*, 96(6):4758–4767, 1992.
- [41] Ole Hassager. Stress-controlled oscillatory flow initiated at time zero: A linear viscoelastic analysis. *Journal of Rheology*, 64:545–550, 2020.
- [42] Markus Herrchen and Hans Christian Öttinger. A detailed comparison of various fene dumbbell models. *Journal of non-newtonian fluid mechanics*, 68(1):17–42, 1997.
- [43] Krister Holmberg, Dinesh Ochhavlal Shah, and Milan J Schwuger. *Handbook of applied surface and colloid chemistry*, volume 1. Wiley-Blackwell, 2002.
- [44] Y Thomas Hu and A Lips. Kinetics and mechanism of shear banding in an entangled micellar solution. *Journal of Rheology*, 49(5):1001–1027, 2005.

- [45] Y Thomas Hu, C Palla, and A Lips. Comparison between shear banding and shear thinning in entangled micellar solutions. *Journal of Rheology*, 52(2):379–400, 2008.
- [46] JD Huppler. 1. f. macdonald, e. ashare, tw spriggs, rb bird, la holmes. *Trans. Soc. Rheo*, 11:181, 1967.
- [47] Kyu Hyun, Manfred Wilhelm, Christopher O. Klein, Kwang Soo Cho, Jung Gun Nam, Kyung Hyun Ahn, Seung Jong Lee, Randy H. Ewoldt, and Gareth H. McKinley. A review of nonlinear oscillatory shear tests: Analysis and application of large amplitude oscillatory shear (laos). *Progress in Polymer Science*, 36:1697–1753, 2011.
- [48] Jacob N Israelachvili. *Intermolecular and surface forces*. Academic press, 2011.
- [49] W. Mervyn Jones. Viscoelastic properties of polymers : by j.d. ferry, john wiley and son, 1980, 3rd edition. *Journal of Non-newtonian Fluid Mechanics*, 8:369, 1981.
- [50] A Kate Gurnon and Norman J Wagner. Large amplitude oscillatory shear (laos) measurements to obtain constitutive equation model parameters: Giesekus model of banding and nonbanding wormlike micelles. *Journal of Rheology*, 56(2):333–351, 2012.
- [51] Frank Kern, François Lequeux, Raoul Zana, and Sauveur Jean Candau. Dynamic properties of salt-free viscoelastic micellar solutions. *Langmuir*, 10:1714–1723, 1994.
- [52] SA Khan and RG Larson. Comparison of simple constitutive equations for polymer melts in shear and biaxial and uniaxial extensions. *Journal of Rheology*, 31(3):207–234, 1987.
- [53] Sunilkumar Khandavalli, Jan Hendricks, Christian Clasen, and Jonathan P. Rothstein. A comparison of linear and branched wormlike micelles using large amplitude oscillatory shear and orthogonal superposition rheology. *Journal of Rheology*, 60:1331–1346, 2016.
- [54] Sunhyung Kim, Jan Mewis, Christian Clasen, and Jan Vermant. Superposition rheometry of a wormlike micellar fluid. *Rheologica Acta*, 52(8):727–740, 2013.

- [55] Sunhyung Kim, Jan Mewis, Christian Clasen, and Jan Vermant. Superposition rheometry of a wormlike micellar fluid, responding to errors found in the paper. *Rheologica Acta*, 52(8):727–740, 2013.
- [56] Sarah A. Klemuk and Ingo R. Titze. Determining motor inertia of a stress-controlled rheometer. *Journal of rheology*, 53 4:765, 2009.
- [57] Ronald G. Larson. The structure and rheology of complex fluids. 1998.
- [58] Kyle R Lennon, Gareth H McKinley, and James W Swan. Medium amplitude parallel superposition (maps) rheology of a wormlike micellar solution. *Rheologica Acta*, 60:729–739, 2021.
- [59] Christopher W. Macosko. Rheology: Principles, measurements, and applications. 1994.
- [60] GC Maitland. Oil and gas production. *Current opinion in colloid & interface science*, 5(5-6):301–311, 2000.
- [61] Alexander Ya Malkin. Non-linearity in rheology—an essay of classification. *Rheologica acta*, 34(1):27–39, 1995.
- [62] Hershel Markovitz. Boltzmann and the beginnings of linear viscoelasticity. *Transactions of the Society of Rheology*, 21(3):381–398, 1977.
- [63] U Menge, P Lang, and GH Findenegg. From oil-swollen wormlike micelles to microemulsion droplets: a static light scattering study of the l1 phase of the system water+ c12e5+ decane. *The Journal of Physical Chemistry B*, 103(28):5768–5774, 1999.
- [64] Vishal Metri and WJ Briels. Brownian dynamics investigation of the boltzmann superposition principle for orthogonal superposition rheology. *The Journal of chemical physics*, 150(1):014903, 2019.
- [65] Jan Mewis and Gary Biebaut. Shear thickening in steady and superposition flows effect of particle interaction forces. *Journal of Rheology*, 45(3):799–813, 2001.

- [66] Jan Mewis and Gustaaf Schoukens. Mechanical spectroscopy of colloidal dispersions. *Faraday Discussions of the Chemical Society*, 65:58–64, 1978.
- [67] T.G Mezger. Applied rheology 2nd ed., anton paar gmbh. 2015.
- [68] Paula Moldenaers and Joannes Mewis. On the nature of viscoelasticity in polymeric liquid crystals. *Journal of rheology*, 37(2):367–380, 1993.
- [69] Faith A Morrison et al. *Understanding rheology*, volume 1. Oxford university press New York, 2001.
- [70] Isaac Newton and NW Chittenden. *Newton’s Principia: the mathematical principles of natural philosophy*. Geo. P. Putnam, 1850.
- [71] Ad Hoc Committee on Official Nomenclature and Symbols. Official symbols and nomenclature of the society of rheology. *Journal of Rheology*, 57(4):1047–1055, 2013.
- [72] Kunihiro Osaki, Mikio Tamura, Michio Kurata, and Tadao Kotaka. Complex modulus of concentrated polymer solutions in steady shear1. *The Journal of Physical Chemistry*, 69(12):4183–4191, 1965.
- [73] H. Ch. Öttinger. Stochastic processes in polymeric fluids: Tools and examples for developing simulation algorithms. 1995.
- [74] Robert Owens and Timothy Phillips. Computational rheology. 05 2002.
- [75] Nabil Ramlawi, Narayanan Ashwin Kumar Bharadwaj, and Randy H. Ewoldt. The weakly nonlinear response and nonaffine interpretation of the johnson–segalman/gordon–schowalter model. *arXiv: Soft Condensed Matter*, 2020.
- [76] Heinz Rehage and Heinz Hoffmann. Viscoelastic surfactant solutions: model systems for rheological research. *Molecular Physics*, 74:933–973, 1991.
- [77] John L. Schrag. Deviation of velocity gradient profiles from the “gap loading” and “surface loading” limits in dynamic simple shear experiments. 1977.

- [78] Toshiyuki Shikata, Hirotaka Hirata, and Tadao Kotaka. Micelle formation of detergent molecules in aqueous media: viscoelastic properties of aqueous cetyltrimethylammonium bromide solutions. *Langmuir*, 3:1081–1086, 1987.
- [79] Paul Thomas Slatter. The rheological characterisation of sludges. *Water Science and Technology*, 36:9–18, 1997.
- [80] JFA Soltero, JE Puig, and O Manero. Rheology of the cetyltrimethylammonium tosylate- water system. 2. linear viscoelastic regime. *Langmuir*, 12(11):2654–2662, 1996.
- [81] Madan Somasi, Bamin Khomami, Nathanael J Woo, Joe S Hur, and Eric SG Shaqfeh. Brownian dynamics simulations of bead-rod and bead-spring chains: numerical algorithms and coarse-graining issues. *Journal of non-newtonian fluid mechanics*, 108(1-3):227–255, 2002.
- [82] Murray R. Spiegel. Schaum’s outline of theory and problems of laplace transforms. 1965.
- [83] James Freeman Steffe. Rheological methods in food process engineering. 1992.
- [84] Jun-Hee Sung, Sung-Taek Lim, Chul-Am Kim, Chung Heejeong, and Hyoung-Jin Park. Mechanical degradation kinetics of poly (ethylene oxide) in a turbulent flow. *Korea-Australia Rheology Journal*, 16(2):57–62, 2004.
- [85] RI Tanner. Comparative studies of some simple viscoelastic theories. *Transactions of the Society of Rheology*, 12(1):155–182, 1968.
- [86] Ran Tao and Aaron M Forster. End effect correction for orthogonal small strain oscillatory shear in a rotational shear rheometer. *Rheologica Acta*, 59(2):95–108, 2020.
- [87] Nicholas W Tschoegl. *The phenomenological theory of linear viscoelastic behavior: an introduction*. Springer Science & Business Media, 2012.

- [88] MS Turner and ME Cates. Linear viscoelasticity of living polymers: A quantitative probe of chemical relaxation times. *Langmuir*, 7(8):1590–1594, 1991.
- [89] Jan Vermant, L Walker, Paula Moldenaers, and Joannes Mewis. Orthogonal versus parallel superposition measurements. *Journal of non-newtonian fluid mechanics*, 79(2-3):173–189, 1998.
- [90] Lynn M Walker, Jan Vermant, Paula Moldenaers, and Jan Mewis. Orthogonal and parallel superposition measurements on lyotropic liquid crystalline polymers. *Rheologica acta*, 39(1):26–37, 2000.
- [91] Kelly Zack Walters. Lessons from history. *Korea-australia Rheology Journal*, 11:265–268, 1999.
- [92] Harold R Warner Jr. Kinetic theory and rheology of dilute suspensions of finitely extendible dumbbells. *Industrial & Engineering Chemistry Fundamentals*, 11(3):379–387, 1972.
- [93] JM Wiest and RI Tanner. Rheology of bead-nonlinear spring chain macromolecules. *Journal of Rheology*, 33(2):281–316, 1989.
- [94] Arthur J. Winfield. Rheological techniques, 2nd edition : R. w. whorlow, ellis horwood, 1992. pages xvii + 460. £60.00. isbn 13-775370-5. *Talanta*, 41:1611–1612, 1994.
- [95] Misazo Yamamoto. Rate-dependent relaxation spectra and their determination. *Transactions of the Society of Rheology*, 15(2):331–344, 1971.
- [96] Norman Y. Yao, Ryan J. Larsen, and David A. Weitz. Probing nonlinear rheology with inertio-elastic oscillations. *Journal of Rheology*, 52:1013–1025, 2008.
- [97] Jacques L Zakin, Bin Lu, and Hans-Werner Bowersdorff. Surfactant drag reduction. *Reviews in Chemical Engineering*, 14(4-5):253–320, 1998.

- [98] Jos Zeegers, Dirk van den Ende, Cor Blom, Egbert G Altena, Gerrit J Beukema, and Jorrit Mellema. A sensitive dynamic viscometer for measuring the complex shear modulus in a steady shear flow using the method of orthogonal superposition. *Rheologica acta*, 34:606–621, 1995.